THE
JOHNS HOPKINS
UNIVERSITY

DEPARTMENT

OF

PHYSICS & ASTRONOMY

A Measurement of the B Quark
and Neutral B Meson
Production Cross Sections
in Proton-Antiproton Collisions at a Center
of Mass Energy of 1.8 TeV

by

Steve Vejcik, III

Baltimore, Maryland 21218

A Measurement of the b Quark and Neutral B Meson

Production Cross Sections in Proton-Antiproton

Collisions at a Center of Mass Energy of 1.8 TeV

by

Steve Vejcik III

A dissertation submitted to

The Johns Hopkins University

in conformity with the requirements for the

degree of Doctor of Philosophy

Baltimore, Maryland

August, 1992

Abstract

The measurement of the b quark and B^0 meson production cross sections in $\bar{p}p$ collisions at $\sqrt{s} = 1.8$ TeV for $|y| < 1.0$ and $P_T(B^0) > 9.0$ GeV/c, $P_T(b) > 11.5$ GeV/c is reported. The B^0 sample was tagged with the decay chain $B^0 \rightarrow J/\psi\ K^{0*}$, $J/\psi \rightarrow \mu^+\mu^-$, $K^{0*} \rightarrow K^{\pm}\pi^{\mp}$ from a sample of $\bar{p}p$ collisions with an integrated luminosity of 4.3 pb^{-1} .

The results are compared to the values predicted from $\mathcal{O}(\alpha_S{}^3)$ perturbative Quantum Chromodynamics and indicate a production rate for b quarks which is in excess of that predicted. Implications of the result are that the next-to-leading order calculations are not yet capable of precisely predicting heavy quark production rates. The same calculations are presently utilized to estimate the production cross section of top quarks.

While these calculations may be more reliable for top quarks, the discrepancy between the calculated and measured b quark production cross section could indicate that present upper limits on the top quark mass are conservative. This thesis was prepared under the guidance of Professor Bruce Barnett.

Acknowledgements

Many people have helped me to get to this point. I'm going to try to name and thank as many of them as I can, and I apologise in advance to those that I forget.

For starters, everyone I've been associated with in the Johns Hopkins HEP group has been really great. John Skarha and Rick Snider are two examples of what I think good scientists should be and really taught me quite a bit. Over the last several months in particular, John was put through the painful and tedious job of sitting down with me and ensuring that this thesis was done right, and for that he gets my unending gratitude. John Matthews deserves mention, especially for showing me the value of 'back of the envelope' calculations. It was fun having Alain Spies and Jeff Tseng around the past year or two-I hope they realise how good they're going to have it with the next run's data. Of course the biggest constant in my graduate career has been having Chris Boswell around. Thanks for being a good friend over the years. Finally, I'd like to thank my advisor, Bruce Barnett, for bringing me to this point in pretty good shape. I don't see how it would've been possible to have had a better advisor.

I'm also greatful to have been a part of the CDF collaboration. Even though the collaboration is now large enough to incorporate itself as a small town, people are still pretty friendly and answers to questions can usually be had by just walking down the hall and asking. There are some people I need to specifically thank. Dan Amidei was the first person I met at CDF and I owe him quite a bit of thanks for the friendliness he showed and for having a great attitude about everything. There were a lot of other people on CDF and especially in the SVX group I need to thank. Some of the ones that come to mind are Paul Tipton, Carl Haber, Mike Hrycyk, Bert Gonzales, Paul Derwent, Fabrizio Rafaelli, Harry Carter, William Wester, and Franco Bedeschi. Outside of the SVX group, special thanks

go out to Frits Dejongh who gets a large amount of credit for having the patience to have shown me how to do an analysis and to take the time to try and do it right.

Next on the list has to come the 'Vermin':Colin, Dan, Mark, Chris, and Amy. Thanks for being good friends - I hope we all stay in touch. Speaking of the Vermin, I also need to thank Judy at the User's Center for being a really great bartender and a cool person overall. I also want to thank Brian Harral, Bob Mattingly, Camille Ginsburg, and Doug and Jenny Benjamin for good times the last couple years.

There are also a lot of people outside of CDF/FNAL who I'm happy to thank. Back at Hopkins, Robert Welsh has been a good friend since undergraduate days-thanks man. I also have to acknowledge the friendship of, Dave Leonavicius and Brandt Heatherington. It helped to have both of you around when I needed a break.

Finally, and most importantly, I have to thank my family for being there for me when I really needed them. I owe most of where I am and what I've accomplished to both of my parents and I'd like to dediciate this to both of them.

Contents

2

List of Figures

List of Tables

Chapter 1

Introduction

This introduction is intended to give an overview of what is contained in the pages beyond. The author has also devoted some space in this chapter to his opinions about science and physics.

It can certainly be argued that science in general, and physics in particular have been very successful at creating a picture of the universe which is both accessible to the human mind and incredibly beautiful. It does not seem too far fetched to speculate that no aspect of the physical universe is beyond our capability of understanding. The success of physics has reinforced that what we see and perceive is, after all, a *physical* universe. That is, when a human being perceives something about this world, it is inconceivable that he or she could ask why and how it happens and *not* expect to find the answers.

It gives no less pleasure to find out that in addition to being something we can make sense of, the Universe is also a rich and beautiful place. One of the more offensive stereotypes of physicists is the picture of them as people who are concerned with gears and circuits and such, but who lack some aesthetic sense of beauty, spirituality, and the like. Time and

again, when physicists have tried to make sense of what they have seen, it has turned out that the answer was not only 'correct', but elegant and beautiful.

A case in point has been the development of Quantum Mechanics as the way in which to describe phenomena at small length scales. At its fundamental level, it can be thought of as our best present answer to the question of how and what can we know about the universe. It allows for a universe in which reality does not have to be the great machine envisaged by the world of Newtonian Mechanics and forces what once were metaphysical questions about the role of the observer into the scientific domain. That aspect is still not satisfactorily answered, and it may be that Quantum Mechanics itself will evolve into something more encompassing than its present state.

Now, of course, the majority of time spent by scientists rarely involves anything so sublime. Most of the time is spent paying attention to the knobs and dials needed to crack Nature's doors. On the other hand, this is also part of the reason it's so much fun. It is a truly amazing experience to think about things like quarks, electrons, and such, build something with your own hands to observe them, and then go out and really see them. I suspect that it is only in experimental science that the *reality* of these things we talk about can be appreciated.

It is a very sad paradox of our culture today, even in better educated circles, that in times where we can claim to have a pretty good understanding of our world, there are people who choose to turn away from this knowledge - simply because we can understand it. It is hoped that we can make what we've learned from particle physics accessible to others and that we can continue to push and learn from things around us.

1.1 Outline of Thesis

The analysis presented in this thesis is a study of b quark production. Specifically, a measurement was made of how often b quarks were produced when a proton and its antiparticle, the antiproton, annihilated with each other in a collision. The b quark is the heaviest known quark and is presently believed to be fundamental. This means that currently there is no evidence that b quarks are formed from bound states of other particles. Fundamental particles are important in particle physics because it is believed that they form the pieces from which all matter can be accounted for. The fact that b quarks are both fundamental and relatively massive makes it easier to understand certain basic interactions in which b quarks participate.

The measurement consisted of several steps. The first step was to record what happened during each of the many $\bar{p}p$ collisions. This was done with a particle detector located near the point at which the protons and antiprotons collided. The particle detector is a device which records properties of each collision such as what particle went where and how much energy was left by particles in different regions of space.

The second step was to look at each event, trying to isolate collisions which produced b quarks . This involved studying simulations of what b quarks did when produced and looking at the recorded data for events which appeared to do the same thing. In this particular analysis the events which were sought were those in which the b quark formed a B^0 meson and subsequently decayed into a J/ψ and a K^{0*} meson. These two mesons were found by looking for the particles into which they decayed and which could be observed directly by the particle detector. The J/ψ decayed into two muons and the K^{0*} decayed into a charged K meson and a charged π meson.

The third step of the measurement was to estimate how effective the detector was at

finding these types of events. The effectiveness of the detector was known as its efficiency and included such effects as the geometric coverage provided by the detector.

Knowing the efficiency and how often *b* quarks were observed, the frequency with which they were produced was estimated. As a final step, the production rate was normalized to the number of colliding protons and antiprotons per unit time. This normalization factor was called the luminosity, and the ratio between it and the production rate is the cross section.

The thesis is organized as follows. In Chapter Two, the theoretical background relevant to the analysis is reviewed. Chapter Three describes the apparatus which made up the CDF detector and the particle accelerators which the produced the interactions that were studied. Chapter Four details the analysis itself. Chapter Four is somewhat more lengthy than the other chapters and in it will be found separate sections treating the behavior of the trigger system, results from simulated data, the analysis of the data, and finally the calculation of the cross section. Chapter Five concludes by comparing the measurement with the results of other analyses and with the theoretical predictions.

Chapter 2

Theory

2.1 The Standard Model

The Standard Model [1] is the current theory of the fundamental constituents of matter and their interactions. It postulates the existence at low energies (scales much less than 80 GeV) of three interactions. These are the weak, electromagnetic, and strong interactions. The weak and electromagnetic interactions are different aspects of the same interaction called the electroweak interaction. Many texts are available for a detailed description of the Standard Model [2]. This Section will review its basic features.

2.1.1 Electroweak Interactions

The Lagrangian describing the electroweak interaction is postulated to have the local gauge symmetry of $SU(2)_L \otimes U(1)$. These groups correspond to generalized rotations. The $U(1)$ group is equivalent to a phase rotation, while the $SU(2)_L$ group is equivalent to rotations in three dimensions [3]. The electroweak interaction is not parity invariant. The subscript L

	Mass (GeV/c^2)	Width (GeV)
$W^\pm$	80.22 ± 0.26	2.12 ± 0.11
Z^0	91.173 ± 0.020	2.487 ± 0.010
γ	$< 3 \times 10^{-36}$	stable

Table 2.1: The gauge bosons of electroweak interactions in the Standard Model.

reflects the fact that the interaction treats particles differently depending on their helicity. At low energies, the behavior of the electroweak interaction appears to act as two different interactions. This is a consequence of *symmetry breaking*. The postulate of scalar fields in the theory obscures the gauge symmetry resulting in what appear to be two distinct interactions–the weak force and electromagnetism.

The quantized fields of the Standard Model are associated with vector bosons. There are four bosons associated with the unbroken $SU(2)_L \otimes U(1)$ symmetry of the electroweak interaction. Through symmetry breaking the field quanta associated with the $SU(2)_L$ and $U(1)$ gauge groups are mixed together to form the physically observed particles. A subset of these gauge bosons also acquire large masses. These bosons, the $W^\pm$ and Z^0, have masses of about 80-90 GeV/c^2. The massive bosons result in the short distance interaction associated with the weak force whose effective coupling at low energies is small relative to that of the electromagnetic interaction. The observation in 1983 of the $W^\pm$ and Z^0 by the UA1 collaboration [4] was a major triumph for the Standard Model of electroweak interactions. Table 2.1 summarizes the gauge bosons of the electroweak interaction.

The Standard Model also specifies the fundamental constituents of matter which interact by exchange of the gauge bosons. These particles can be grouped according to the different ways they can interact. Quarks are the particles which have strong as well as electroweak

charge. Leptons have only an electroweak charge. Both types of particles are fermions, having spin equal to 1/2.

The left-handed components of these fermions form doublet representations of $SU(2)_L \otimes U(1)$, while the right-handed components form singlet representations. The interacting doublets and singlets are shown in Figure 2.1. Note that the neutrino only appears in the doublets, and that no right-handed neutrinos are present in the theory.

There are three sets, or generations, of leptons and quarks. In the leptonic sector, these generations are associated with an additional quantum number. For instance, the generation including the electron and ν_e carries the 'electron-lepton' quantum number. Conservation of this quantum number prevents transitions such as $\mu \rightarrow e\bar{\nu}_\mu$. The quarks also carry an additional quantum number but, instead of being associated with generations, these quantum numbers appear to be unique to each individual quark. Thus, the bottom quark carries the 'bottomness' quantum number. These quantum numbers, or flavors, are conserved by the strong interaction but not by the electroweak interaction.

The violation of flavor conservation in electroweak interactions happens in a very specific manner. The quark generations which participate in the charged current interactions are not the same as the mass eigenstates depicted in Figure 2.1 , but are 'rotated'. The states appearing in an interaction are linear combinations of the mass eigenstates. The matrix which accomplishes this rotation is the Cabbibo-Kobayashi-Maskawa (CKM) matrix [5]. In a completely general way, the rotation can be described purely by its effect on the $I_Z = -1/2$ members of each weak isodoublet.

The CKM matrix has ten parameters which are not predicted by the Standard Model. These parameters are not all independent. As with normal rotations, there are three parameters which describe the rotation. Additionally, there is one overall phase which is not arbitrary, so that only four of the ten parameters are independent. These are presently

—Determination of CKM elements [6]—

V_{ud}	Nuclear β decay, Muon decay
V_{us}	Analysis of K_{e3} and Hyperon decays
V_{ub}	No direct measurement. Value is 90% confidence limit using $|V_{ub}/V_{cb}| = 0.09 \pm 0.04$
V_{cd}	ν and $\bar{\nu}$ production of charm off valence d quarks
V_{cs}	D_{l3} decay combined with lifetimes τ_D
V_{cb}	Semileptonic B decays
V_{td}	B_d mixing, limits on m_t, and theoretical assumptions
V_{ts}	B_s mixing, limits on m_t, and theoretical assumptions
V_{tb}	Unitarity

Table 2.2: Methods used to measure elements of CKM matrix.

assumed to be fundamental parameters which must be measured by experiment. Figure 2.2 and Table 2.2 summarize the present knowledge of the elements of the CKM matrix.

2.1.2 QCD

While the electroweak sector of the Standard Model has been extensively studied and shown to agree very well with experiment, the strong interaction has not been tested as thoroughly. A feature of the theory is that the strong interaction becomes weaker with increasing collision energy. Because of this, predictions are thought to be reliable at energy scales greater than a few GeV. One goal of the analysis presented in this thesis is to test our understanding of the strong interaction at such energies.

$$\begin{pmatrix} u_L \\ d_L \end{pmatrix} \quad \begin{pmatrix} c_L \\ s_L \end{pmatrix} \quad \begin{pmatrix} t_L \\ b_L \end{pmatrix} \qquad \begin{pmatrix} e_L \\ \nu_{eL} \end{pmatrix} \quad \begin{pmatrix} \mu_L \\ \nu_{\mu L} \end{pmatrix} \quad \begin{pmatrix} \tau_L \\ \nu_{\tau L} \end{pmatrix}$$

$$u_R \quad d_R \quad c_R \quad s_R \quad t_R \quad b_R$$

$$e_R \quad \mu_R \quad \tau_R$$

Figure 2.1: The constituent particles of the Standard Model. The subscripts 'L' and 'R' refer to the chirality of the particles.

$$\begin{pmatrix} V_{ud} & V_{us} & V_{ub} \\ V_{cd} & V_{cs} & V_{cb} \\ V_{td} & V_{ts} & V_{tb} \end{pmatrix} = \begin{pmatrix} 0.9747 - 0.9759 & 0.218 - 0.224 & 0.002 - 0.007 \\ 0.218 - 0.224 & 0.9735 - 0.9751 & 0.032 - 0.054 \\ 0.003 - 0.018 & 0.030 - 0.054 & 0.9985 - 0.9995 \end{pmatrix}$$

Figure 2.2: The Cabbibo-Kobayashi-Maskawa matrix [7]. The numbers are 90% confidence limits assuming unitarity and the existence of three quark-lepton generations.

The Standard Model hypothesizes that strong interactions can be described by *Quantum Chromodynamics* (QCD) [8]. These interactions are assumed to be symmetric under the local gauge transformations described by the group $SU(3)_{color}$, where the term 'color' is the generic name for the interacting fields of QCD. This symmetry leads to the prediction of a coupling constant, α_S , whose strength decreases with the momentum transfer or energy scale, Q^2 , which characterizes the interaction being studied. The theory includes a parameter, Λ_{QCD}, which corresponds to the Q^2 at which α_S becomes large, and eight gauge bosons called gluons. Both gluons and quarks carry the QCD charge, referred to as color, of which there are three types, usually called Red, Blue, and Green.

Evidence for the existence of color was provided for by measurements of the inclusive cross section for e^+e^- annihilation. The cross section for hadroproduction in e^+e^- annihilation is traditionally measured in units of the calculated lowest order (Born) cross section for $e^+e^- \rightarrow \mu^+\mu^-$. In the absence of color, the ratio $R_{ee} \equiv \frac{\sigma(e^+e^- \rightarrow Hadrons)}{\sigma_{Born}(e^+e^- \rightarrow \mu^+\mu^-)}$ is proportional to the sum of the electric charge squared of the different quarks which can be produced at a given energy. The presence of color, however, increases the number of available quark states by a factor of three. As can be seen in Figure 2.3, the color hypothesis is favored at presently observable energies.

Observable hadronic matter is postulated to be formed from color neutral combinations of quarks and antiquarks. These are either baryons (qqq states) or mesons (q̄q states) Free quarks have never been observed experimentally, a feature thought to arise from the energy dependence of α_S . As discussed in the next section, the strong coupling strength increases as the energy scale in a reaction is decreased. This means that if, in an effort to separate them, the binding energy of a quark-antiquark pair is decreased, the effective coupling strength will increase and therefore the energy density of the color field between the quarks will increase. Eventually, the energy density will be high enough to produce
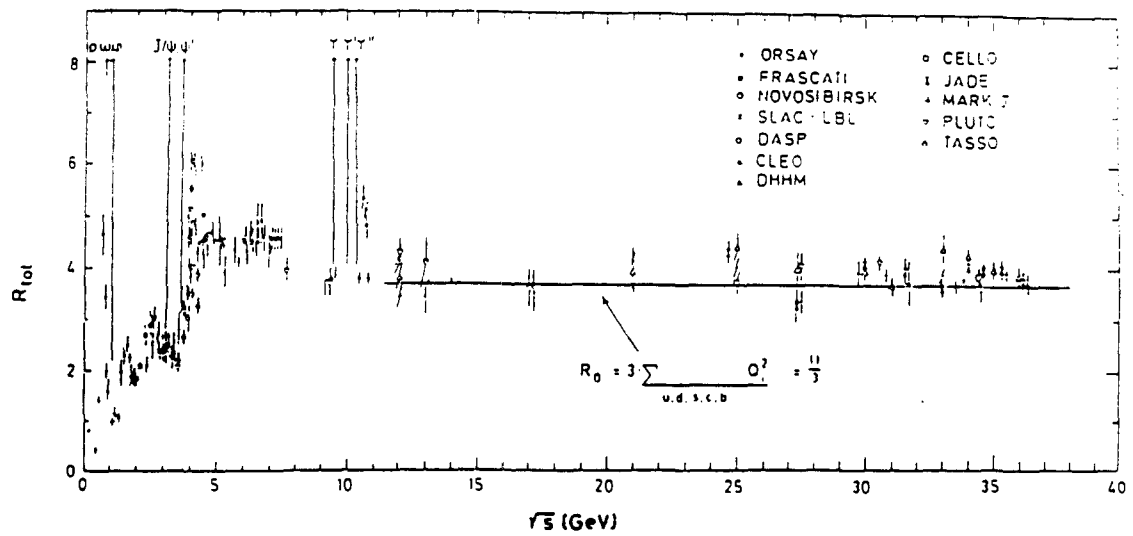
Figure 2.3: Measured and predicted values of R_{ee} within the Standard Model with three colors, from Reference [9]. The excess over the expected values below the Upsilon resonance is thought to be due to various resonances and QCD radiative corrections [10].

a new quark-antiquark pair. Thus, instead of splitting the initial hadron into quarks, an additional hadron is produced and the system remains color neutral. At high energies, this process results in the production of *jets* of colorless particles produced in roughly the same direction as the initial q$\bar{\text{q}}$ pair. Evidence for such jet production was first observed in e^+e^- collisions in 1975 [11]. Figure 2.4 shows a typical two jet event at CDF, demonstrating the jet-like structure of quark fragmentation.

Because the gluons in QCD also carry color charge, they too will produce jets. Evidence for the existence of gluons was provided by the observation of events with three jets by the TASSO and Mark-J collaborations in e^+e^- collisions at the PETRA storage ring [12].

The QCD Running Coupling Constant

A feature of the spontaneously broken gauge theories such as the Standard Model is that they are renormalizable[13]. This means that perturbation methods are guaranteed to produce finite results in terms of physically observed parameters. However, the inclusion of only one loop Feynman diagrams, such as the one shown in Figure 2.5 , leads to divergences in the calculated scattering amplitudes when the momentum of a virtual particle in the loop goes to infinity. Such divergences are known as ultraviolet divergences.

The difficulties presented by these divergences are handled by a redefinition of the coupling constant included in the calculations. There is no theoretical prediction for the value of the coupling constants associated with the Feynman diagrams. The renormalization procedure is to define the coupling constant so that it includes the divergent parts of the loop diagrams as well as the original 'bare' coupling. Note that there can be many schemes to define precisely where to separate the divergent from the nondivergent parts , but that the physical observables should be independent of the scheme chosen.

The sensitivity of the coupling to the infinities depends on the energy scale, or Q^2 , of
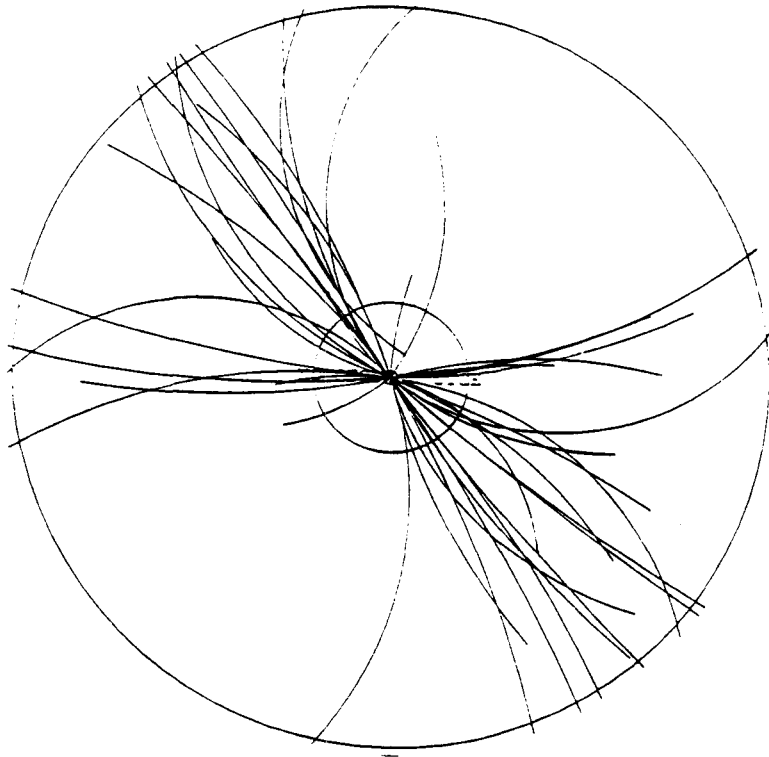
Figure 2.4: An example of a dijet event observed at CDF.

where R is any dimensionless observable. A consequence of the renormalization group equation was that if R was expressed as an nth order perturbative series in α_S, then changing the value of μ would change the value of R by an amount of order α_S^{n+1}. This also implied that a rough idea of the size of higher order corrections in a perturbative series could thus be estimated by varying the value of μ.

2.2 The QCD Improved Parton Model

The idea that hadronic structure is described by pointlike spin-1/2 constituents is known as the parton model. The parton model was first introduced by Feynman [14] in 1972. Evidence that hadrons consisted of these partons came from the experimental study of hadronic structure functions using Deep Inelastic Scattering (DIS) of leptons off of nucleons. Elastic scattering of electrons off of protons depended on a parameter in the proton structure functions which characterized the size of the proton. The value of the structure functions depended explicitly on the value of Q^2 .

In contrast, no scale was present in the scattering of electrons off of the partons within a proton. The structure functions depended only on the dimensionless combination $Q^2/2m_N\nu$ where m_N is the nucleon mass and ν is the energy transfer from the lepton. This means that, in contrast to ep scattering for instance, the structure functions do not depend on the absolute value of Q^2 . This behaviour, predicted by Bjorken [15], was observed in DIS in 1971 [16], and interpreted by Feynman as elastic scattering off of the partons within the nucleons.

The distributions of parton momenta within a hadron are characterized by the parton distribution functions which are directly related to the structure functions. The terms 'structure function' and 'parton distribution function' are often used interchangeably. These

functions describe the distribution of z, the fraction of the hadron momentum carried by the partons.

While the original parton model predicted perfect scaling, the introduction of QCD as the interaction which binds the partons together leads to structure functions which exhibit a slight dependence on the momentum transfer, Q^2, in scattering experiments. The dependence arises from reasons similar to those which lead to the running QCD coupling constant.

The parton distribution functions are sensitive to how the partons interact with one another and with the different virtual particles which accompany them. The virtual particles become increasingly important with smaller values of z. The interactions among these particles can occur at soft energy scales, $Q^2 < \Lambda_{QCD}^2$, where the distributions cannot be calculated perturbatively. They can, however, be probed by studying Deep Inelastic Scattering of leptons on nuclei.

In the parton model, the cross section for the scattering of a virtual photon (from an incident lepton in DIS, for instance) off of a quark in a proton was calculated by factorizing the cross section into two pieces. One piece was described by the parton distribution function, which gives the probability that a target parton within the proton had some momentum fraction x. The second piece was the hard scattering amplitude for the process $\gamma^* q \rightarrow q$, calculable using perturbative techniques.

The next-to-leading order calculation of the hard scattering cross section included QCD modifications. At $\mathcal{O}(\alpha_S)$, theoretical predictions for the hard scatter resulted in infinities from diagrams such as those shown in Figure 2.6. The singularities correspond to emission of real gluons which were parallel to a quark line (collinear singularities). In the QCD parton model, these singularities were absorbed into the measured distribution functions. Just as with the running coupling constant, this introduced a parameter, μ, which divided

the scattering process into its perturbative and non-perturbative parts as a function of the momentum regime being probed. Additionally, this factorization procedure predicted that the parton distribution functions, or equivalently the structure functions, would exhibit scaling violation by showing a dependence on Q^2.

The Q^2 dependence of the structure functions was described by the Altarelli-Parisi equation:

$$\frac{dF(x, Q^2)}{dlogQ^2} = \frac{\alpha_s}{2\pi} \int \frac{dy}{y} F(y, Q^2) P_{qq}(\frac{x}{y}), \tag{2.5}$$

where, F is the parton distribution function and $P_{qq}(z)$ is a 'splitting' function, which describes the probability of a quark emitting a gluon and retaining a fraction z of its original momentum. The quantity ν is the energy loss of the scattered lepton. The solutions to the Altarelli-Parisi equations are analogous to the equations for the running coupling constant (Equations 2.1 or 2.3).

Physically, the Q^2 dependence of the structure functions arises because the partons being resolved in DIS could emit and absorb virtual gluons, and therefore began to differ in their properties from the pointlike particles of the original parton model.

The presence of collinear or other infrared singularities in some physical quantity also modified the renormalization group equation (equation 2.4) which any observable must satisfy. As is discussed in Section 2.3.3, this could be utilized to obtain higher order contributions to processes involving hadrons.

While the Q^2 dependence of the distribution functions was contained in the Altarelli-Parisi equation, their absolute value had to be fixed at some particular Q^2 by experiment. As mentioned above, such measurements were the typically the result of Deep Inelastic Scattering experiments. The x dependence of the structure functions was measured at different Q^2 . The data were used to provide a parameterization of the x-dependence of the
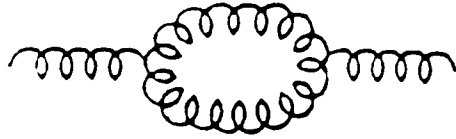
Figure 2.5: An example of a one loop diagram in QCD. The presence of such loops necessitates the renormalisation of the QCD coupling constant, α_s, and its dependence on the Q^2 of strong interactions.
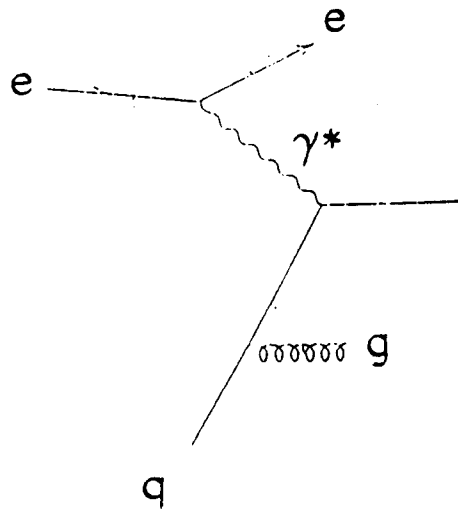
Figure 2.6: Feynman diagram for Deep Inelastic Scattering. The emission of soft virtual gluons as shown in the figure leads to collinear singularities which were removed by mass factorization.

structure functions. Once this was established, the Q^2 dependence could be obtained using the Altarelli-Parisi equation. Instead of integrating the Altarelli-Parisi equation for each needed momentum scale, calculations generally relied on analytic approximations. Several parametrizations can be found in the literature. The distribution functions of Eichten *et. al.*[17] , Duke and Owens[18], DFLM[19], and Morfin and Tung[20] are of particular interest.

2.2.1 Inelastic Scattering of Hadrons

The parton model gave the physical picture and tools needed to calculate cross sections for processes involving the interactions of hadrons through their quark and gluon content. The scheme for calculating observed cross sections is embodied in Figure 2.7, and analytically contained within the formula

$$Ed^3\sigma/d^3k = \sum_{i,j} \int dx_A dx_B \left[\frac{Ed^3\hat{\sigma}_{ij}(x_A P_A, x_B P_B, k, m, \mu)}{d^3k} \right] F_i^A F_j^B. \qquad (2.6)$$

The structure function F_i^A describes the probability that hadron A contains parton type i which carries a fraction x of the hadron momentum P_A. The quantity $\hat{\sigma}_{ij}$ is the short distance cross section. It describes the cross section relevant to each particular parton-parton scattering (*e.g.* $q\bar{q} \rightarrow q\bar{q}$). In the next section, Equation 2.6 will be specialized to the case of b quark production.

2.3 Production of b Quarks

The study of b quarks is important to the study of QCD because of their large mass relative to Λ_{QCD} . At values of $Q^2 \sim M_b^2$, α_S becomes relatively small, typically ~ 0.2 . With a sufficiently small α_S , it should be possible to use perturbative techniques to accurately calculate cross sections.
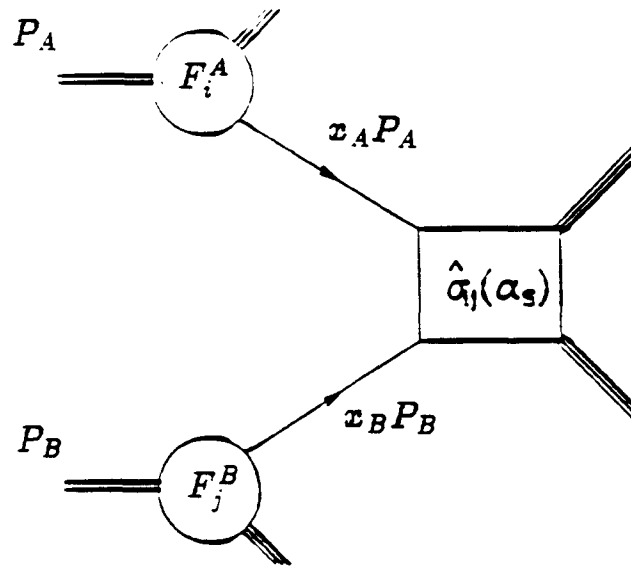
Figure 2.7: Graphical representation hadron-hadron scattering in the Parton Model.

A number of calculations of the b quark production cross section are available in the literature. These calculations will be examined in detail in the following sections. The calculations also have relevance for the production cross sections of the yet undiscovered t quark, and those predictions will also be reviewed.

2.3.1 Predictions for the b Quark Production Cross Section

The calculation of the b quark production cross section begins with the QCD improved parton model and the assumption of the validity of factorization. As discussed above, the latter assumption allows the separation of the short distance parton-parton scattering from the soft interactions which give structure to the hadrons. The incoming hadrons act as sources of partons which interact in a hard scatter with differential cross section $d\hat{\sigma}$. The distribution functions describing the incoming hadrons must satisfy Altarelli-Parisi equations and the total cross section must satisfy a renormalization group equation similar to Equation 2.4.

Specializing to the case of b production corresponds to choosing the relevant renormalization scale (μ) and calculating the appropriate short distance cross sections. Several different choices of μ have been proposed in the literature. The most common one is $\mu^2 = P_T{}^2 + m_b{}^2$. Other choices such as $\mu^2 = 4m_b{}^2$ are possible

The lowest order $\mathcal{O}(\alpha_S{}^2)$ diagrams for heavy quark production have been known for some time [21, 22]. In the case of charm production, the lowest order calculations of the cross sections underestimated the measured rates [23]. The disagreement between the measured charm production cross section and the predicted lowest order cross section helped to motivate the need for next order calculations. The calculation of the $\mathcal{O}(\alpha_S{}^3)$ diagrams for b production was completed by Nason *et. al.* (NDE)[24],[25]. Their results will be discussed in section 2.3.3. The formalism used by NDE to calculate the cross section at both

the leading and next-to-leading order will be discussed here. More details can be found in references[24] and [25].

The total short distance cross section can be calculated as a perturbative series in the running coupling constant:

$$\hat{\sigma} = \frac{\alpha_S^2}{m^2} \mathcal{F}_{ij}(\rho, \frac{\mu^2}{m^2}) \tag{2.7}$$

where

$$\mathcal{F}_{ij}(\rho, \frac{\mu^2}{m^2}) = \mathcal{F}_{ij}^{(0)}(\rho) + \alpha_S [\mathcal{F}_{ij}^{(1)} + \bar{\mathcal{F}}_{ij}^{(1)} log(\frac{\mu^2}{Q^2})] \tag{2.8}$$

and

$$\rho = \frac{4m^2}{\hat{s}}. \tag{2.9}$$

In equation 2.7, $\mathcal{F}_{ij}^{(0)}$ represents the contribution from the lowest order processes and $\mathcal{F}_{ij}^{(1)}$ and $\bar{\mathcal{F}}_{ij}^{(1)}$ represent the contribution from the next-to-leading order diagrams. The quantity $\hat{s}$ is the parton center of mass energy. As will be seen in Section 4.2, the b quark production at CDF was sensitive only to b quarks with P_T's > 10 GeV/c and which were centrally produced ($|y| < 1$) due to geometric acceptance. Measurements are usually compared with the total b quark cross section for b P_T larger than some P_T^{min} and within some rapidity region. The theoretical calculation $\sigma(p\bar{p} \rightarrow bX, P_T^b > P_T^{min})$ involve the integration of the differential cross section over the regions of interest. The differential form of the cross section has the same form as Equation 2.7:

$$\frac{d\hat{\sigma}}{dy d^2 k_T} = \alpha_S^2 H_{ij}^{(0)} + \alpha_S^3 H_{ij}^{(1)}, \tag{2.10}$$

where the functions $H_{ij}^{(1)}$ are the α_S^3 corrections and include terms proportional to $log\frac{\mu^2}{m^2}$ due to the mass singularities. The individual terms depend on the kinematic variables of the scattering process through the parton four-momenta. The analytic forms of the functions

in the differential cross section are lengthy and will not be quoted here, but can be found in Reference[25]. However, because the physical interpretation of the different terms in the $\mathcal{O}(\alpha_S{}^3)$ calculation of the differential cross section are the same as those for the total cross section, they will be discussed below in the context of the total cross section. In the next two sections, the lowest order contributions to the differential cross section are examined, followed by a review of the calculation of the higher order diagrams for the total cross section. The effect of the higher order terms on the differential cross section will be shown without going into the details of the calculations.

2.3.2 Production of b Quarks at $\mathcal{O}(\alpha_S{}^2)$

Important kinematic features of b quark production can be understood by studying the lowest order processes. In particular, the single b differential cross section exhibits the dependence of b production on the variables P_T , rapidity (y), and z. The behavior of these variables can be understood by an examination of the differential cross section for the production of $b\bar{b}$ pairs.

Generalizing equation 2.6 to the case of b pair production, the differential cross section for $b\bar{b}$ production was given by [27]

$$\frac{d\sigma}{dy_3 dy_4 dP_T} = \frac{\alpha^2}{4m_T{}^2(1 + cosh(\Delta y)^2)} \sum_{ij} x_1 f_i(x_1) x_2 f_j(x_2) \overline{\sum_\lambda} |M_{ij}|^2. \tag{2.11}$$

In Equation 2.11 , m_T is the transverse mass, defined as $m_T{}^2 = P_T{}^2 + m^2$, Δy is the rapidity difference between the b and $\bar{b}$ quarks, and the indices i,j run over the different types of partons which can participate in the scattering (gg or $q\bar{q}$). The first summation runs over the different incoming partons and the second summation represents the averaging and summing over incoming and outgoing helicities respectively. The labels of the different variables are as shown in Figure 2.7.

The lowest order diagrams are shown in Figure 2.8.

Following reference[22], the lowest order matrix elements are:

$$\overline{\sum}|M_{q\bar{q}}|^2 = \frac{4}{9}\frac{1}{1+cosh(\Delta y)}\left(cosh(\Delta y) + \frac{m_b{}^2}{m_T{}^2}\right), \tag{2.12}$$

$$\overline{\sum}|M_{gg}|^2 = \frac{1}{24}\frac{8cosh(\Delta y)-1}{1+cosh(\Delta y)}\left(cosh(\Delta y) + 2\frac{m_b{}^2}{m_T{}^2} - 2\frac{m_b{}^4}{m_T{}^4}\right). \tag{2.13}$$

The differential cross section exhibits two features. First, the cross section is suppressed at large values of Δy. This is because the overall dependence on Δy goes like either $cosh^{-1}(\Delta y)$ or $cosh^{-2}(\Delta y)$. This also implies that each quark will be produced at low values of $|y|$. This can be understood from the following argument. The structure functions included in Equation 2.11 are falling functions of x, and the incident parton momenta can be written in terms of the outgoing b quark rapidities:

$$x_1 = \frac{m_T}{\sqrt{S}}\left(e^{y_3} + e^{y_4}\right) \tag{2.14}$$

$$x_2 = \frac{m_T}{\sqrt{S}}\left(e^{-y_3} + e^{-y_4}\right) \tag{2.15}$$

The cross section will be dominated by the regions where the x_i are smallest, because the structure functions are peaked at small x. Since the rapidities of each quark are not too different ($\Delta y \sim 1$), the product $x_1 x_2$ will be dominated by the region of $|y| \sim 0$. In other words, b quarks should be centrally produced.

The exact rapidity distribution depends on the particular choices of structure functions. Figure 2.9 shows the rapidity distribution at center of mass energies corresponding to the Tevatron and Sp$\bar{p}$S colliders using the structure functions of Duke and Owens [28]. Centrally

produced corresponds to values of $|y| \sim 1$. As Figure 2.9 shows, the predicted rapidity distribution was fairly constant out to rapidities of 2 to 3. On the other hand, the geometric acceptance for CDF was limited to an even smaller rapidity range ($|y| < 1$), so that a significant fraction of b quarks were predicted to be produced in regions of large rapidity relative to experimental sensitivity.

A second feature of the lowest order calculations of b production is that the cross section was predicted to fall with increasing transverse mass. This means that the production of b quarks is expected to be suppressed as the P_T of the b quark increased above the b mass. For values of P_T near the b mass, the calculated cross section is not expected to vary as significantly with P_T . Figure 2.10 shows the predicted total cross section at $\mathcal{O}(\alpha_S{}^2)$ for b quarks with $P_T > P_T{}^{min}$, again using the Duke-Owens structure functions [28]. As expected from the above arguments, the calculated cross section is dominated by the low P_T region.

2.3.3 $\mathcal{O}(\alpha_S{}^3)$ Contributions

The calculation of the next-to-leading order terms for b production was motivated by several concerns. As stated earlier, the lowest order calculations for charm production differed from the measured rates. Additionally, the presence of diagrams which are topologically different from the lowest order terms could make a significant contribution to the cross section and could alter the rapidity and P_T dependence of the cross section. In what follows, the $\alpha_S{}^3$ calculations of NDE will be reviewed. Other predictions for the cross section which use the NDE calculations but vary the input parameters and structure functions will also be reviewed.

Figure 2.11 shows examples of the $\mathcal{O}(\alpha_S{}^3)$ diagrams studied by NDE. These diagrams are of two types. The diagrams of Figure 2.11a are pure $\mathcal{O}(\alpha_S{}^3)$ corrections. The diagrams of Figure 2.11b are $\mathcal{O}(\alpha_S{}^4)$ but give an effective $\mathcal{O}(\alpha_S{}^3)$ correction due to interference with
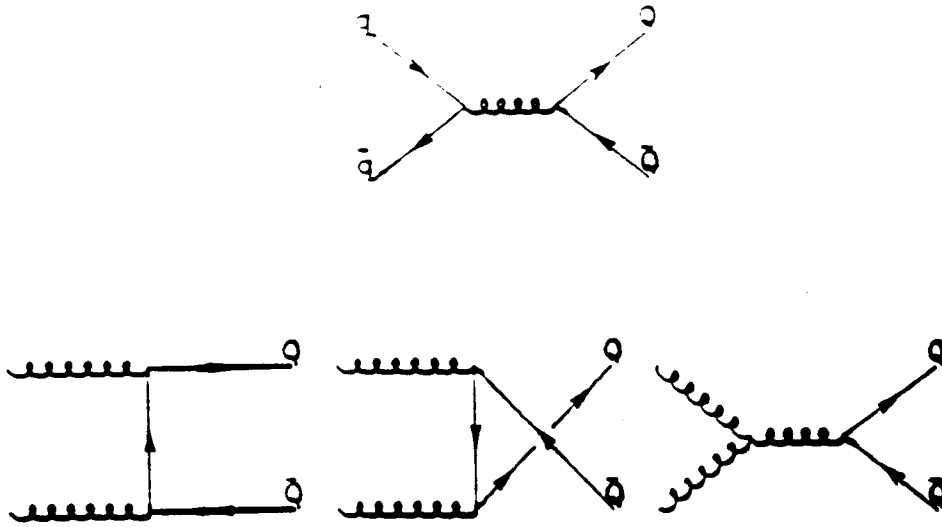
Figure 2.8: **Lowest order Feynman diagrams contributing to heavy quark production.**
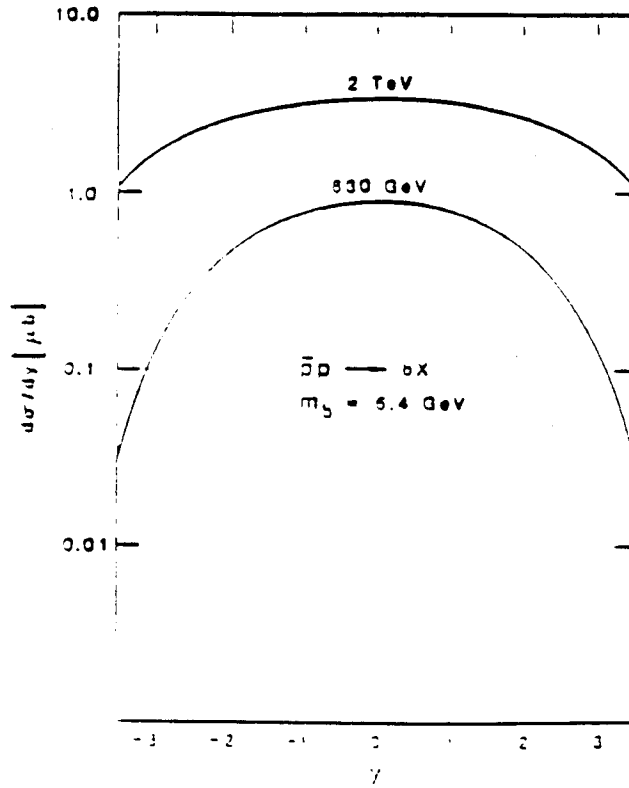
Figure 2.9: Lowest order calculation of $\frac{d\sigma}{dy}$ in b quark production at collider energies.
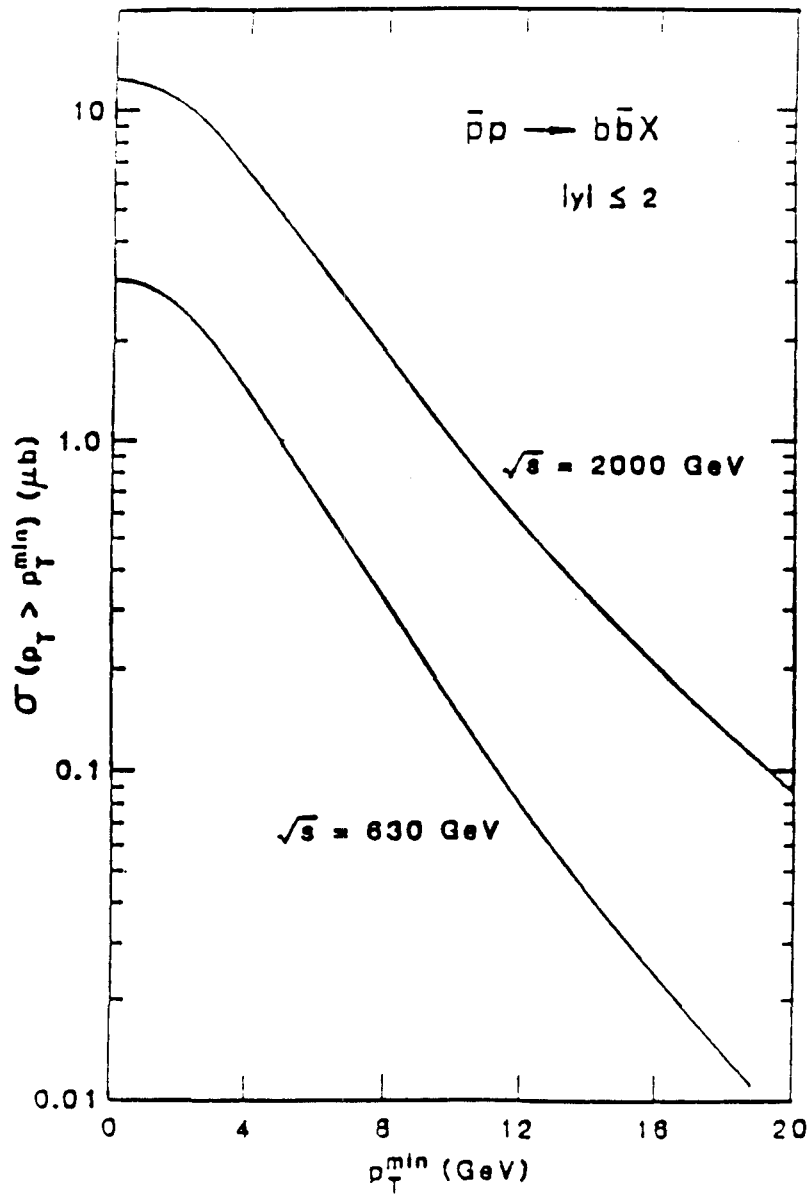
Figure 2.10: Lowest order predictions for the b quark production cross section at collider energies.

the lowest order diagrams. Both types of diagrams contribute to the cross section via the functions $\mathcal{F}_{ij}^{(1)}$ and $\bar{\mathcal{F}}_{ij}^{(1)}$

The quantities $\mathcal{F}_{ij}{}^1$ and $\bar{\mathcal{F}}_{ij}^{(1)}$ depend on the renormalization parameter μ, arising from singularities discussed in section 2.2. The total cross section is required to satisfy a generalized renormalization group equation with the result that $\bar{\mathcal{F}}_{ij}^{(1)}$ is determined by the lowest order term $\mathcal{F}_{ij}{}^{(0)}$:

$$\bar{\mathcal{F}}_{ij}^{(1)} = \frac{1}{8\pi}\left[4\pi b\mathcal{F}_{ij}{}^{(0)}(\rho) - \int\limits_{\rho}^{1} dz_1 \mathcal{F}_{kj}{}^{(0)}(\frac{\rho}{z_1})P_{ki}(z_1) - \int\limits_{\rho}^{1} dz_2 \mathcal{F}_{ik}{}^{(0)}(\frac{\rho}{z_2})P_{kj}(z_2)\right] \quad (2.16)$$

where $b = \frac{33-2n_f}{12\pi}$. The complete $\mathcal{O}(\alpha_S{}^3)$ calculation then fixes the contribution of $\mathcal{F}_{ij}{}^{(1)}$ to the cross section.

In addition to the parton level amplitudes, a choice of structure functions is also required to obtain the b production cross section. The original estimates of NDE were based on two structure functions, EHLQ (set 1) and DFLM. The EHLQ functions included only lowest order effects while DFLM included next-to-leading order effects as well. Figure 2.12 shows the predicted b production cross section for b's with $P_T > P_T{}^{min}$ as a function of $P_T{}^{min}$, using the DFLM structure functions at Tevatron energies, and in the rapidity regions to which CDF was sensitive [25]. The dashed lines in Figure 2.12 represent the theoretical estimate of the uncertainty in the calculation. These uncertainties are discussed in the next section.

The NDE analysis also showed that while the higher order contributions made a significant contribution to the absolute value of the cross section, the shapes of the P_T and y distributions were relatively unchanged. Figure 2.13 shows a comparison made by NDE of the contributions made to the P_T and y distributions from the $\alpha_S{}^2$ and $\alpha_S{}^2 + \alpha_S{}^3$ calculations.
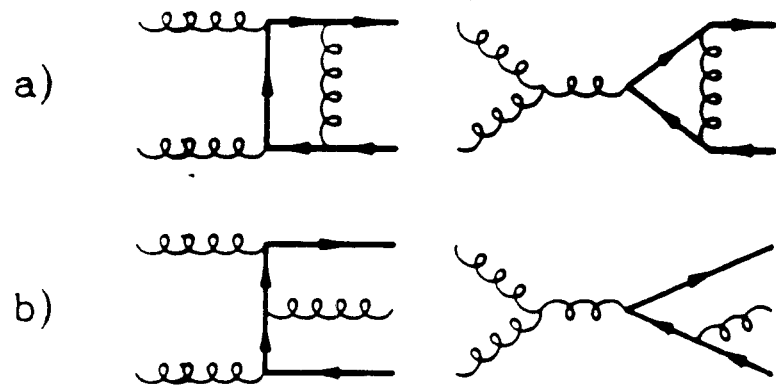
Figure 2.11: Feynman diagrams contributing to next-to-leading order b production cross section. Diagrams in (a) are pure $\mathcal{O}(\alpha_S^3)$ while those in (b) contribute at $\mathcal{O}(\alpha_S^3)$ through interference with the $\mathcal{O}(\alpha_S^2)$ diagrams.
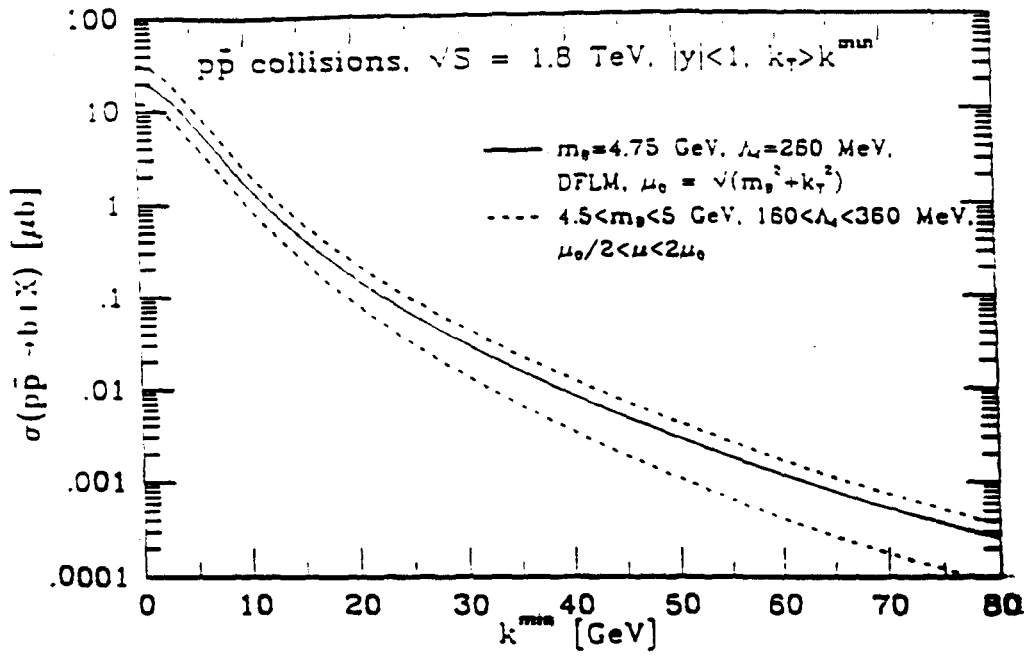
Figure 2.12: $\mathcal{O}(\alpha_S^3)$ predictions for the b quark production cross section. The dashed lines indicate the sensitivity of the predictions to variations in the input parameters.
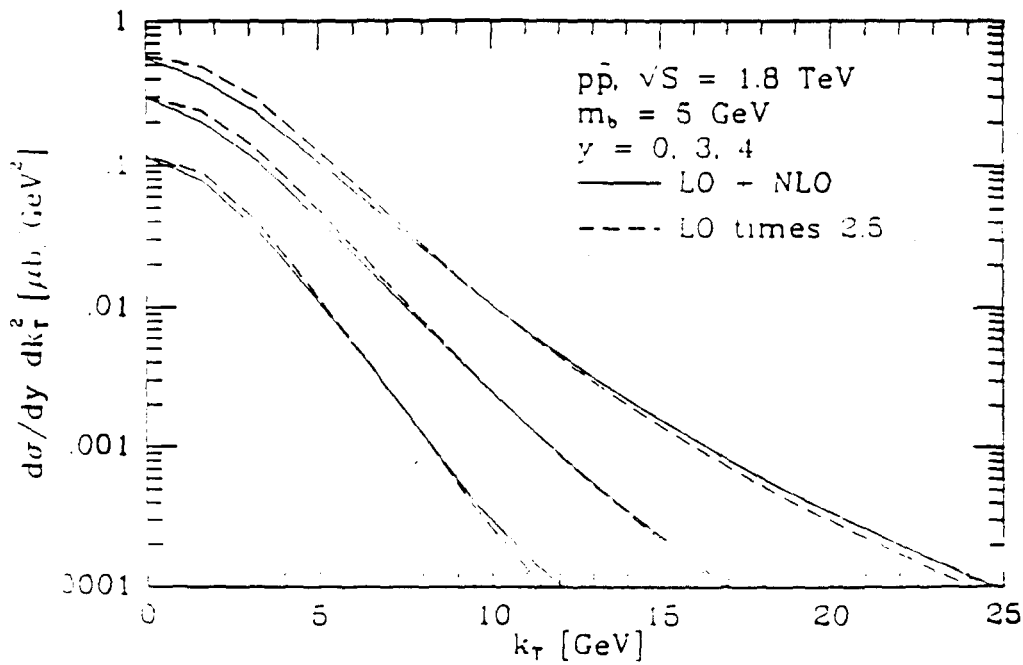
Figure 2.13: NDE predictions for $\frac{d\sigma}{d^2 P_T dy}$ at $\mathcal{O}(\alpha_S^2)$ and at $\mathcal{O}(\alpha_S^3 + \alpha_S^2)$

2.3.4 Theoretical Uncertainties

There are several sources of uncertainty in the predictions for the b quark production cross section. These included:

- Higher order terms

- m_b-the mass of the b quark [a]

- Λ_{QCD}

- Choice of structure functions

In the NDE analysis, quantitative estimates of the sensitivity of the cross section to the first three items were made. The uncertainty due to higher order terms was expected to be reflected by the sensitivity of the cross section to the renormalization scale μ. By varying each of the three sources, an estimate of the uncertainty was made as is shown by the dashed lines in Figure 2.14.

One uncertainty not indicated in the NDE calculations was that due to the structure functions. From Equations 2.14 and 2.15, the parton momenta are probed at lower x as the hadron center of mass energy increases. For b quarks produced at $y = 0$ and with $P_T > 10$ GeV/c, the distribution functions are needed for $x > 0.01$ which is near the current upper limits on the gluon structure functions, and some sensitivity to the various parametrizations of gluon distribution function in this region is expected. The present theoretical status makes

---

[a] The mass of a quark is a difficult quantity to define. As with the QCD coupling constant, the effective mass of a pointlike particle should be a renormalizable quantity which relies on its measurement at some scale to define its value at other energy scales. Unfortunately, our present understanding of QCD indicates that free quarks do not occur in nature. Hence, the value of the quark mass to take in calculations is subject to some ambiguity. Quoted values of quark masses were obtained , for example, from meson masses and the assumptions of a quark-quark potential model.

it difficult to compare the effects of varying the structure functions. Different authors tend to choose different values of the input parameters as well as different structure functions. Table 2.3 summarizes several calculations of b quark production cross sections. Note that even with the different input parameters and choice of distribution functions, the predictions for the cross section vary at most by a factor of 2 and that typically the predictions were within 50% of one another.

Assuming that the uncertainties in the input parameters are reflected in the NDE calculated errors, a comparison of various predictions shows that the different cross sections vary by about the same amount as the NDE calculations due to changes in μ, Λ_{QCD}, or m_b. If a large sensitivity to the structure functions were present, then the predicted cross sections would be expected to differ by an amount larger than that due to variations of the other parameters. That the different predictions were not very different suggested an uncertainty in the calculated cross section of about a factor of two due to the structure functions.

An alternative study of the uncertainty in heavy quark production due to structure functions was the analysis of Harriman, *et. al.* [30]. That analysis used the NDE amplitudes and varied the parameters of the HMRS structure functions to estimate the uncertainty in cross sections for heavy quark production. Their analysis estimated an uncertainty in the predicted cross section of about a factor of three.

2.3.5 Comparison with Present Measurements

The analysis presented in this thesis will measure the b quark cross section at $\sqrt{s} = 1.8$ TeV. The CDF collaboration has several other measurements with different P_T^{min} [32]. These are shown in Figure 2.14. Note that all of these measurements are noticeably greater than the predictions of the NDE calculations.

Figure 2.15 shows the same type of predictions for energies at which the UA1 experiment
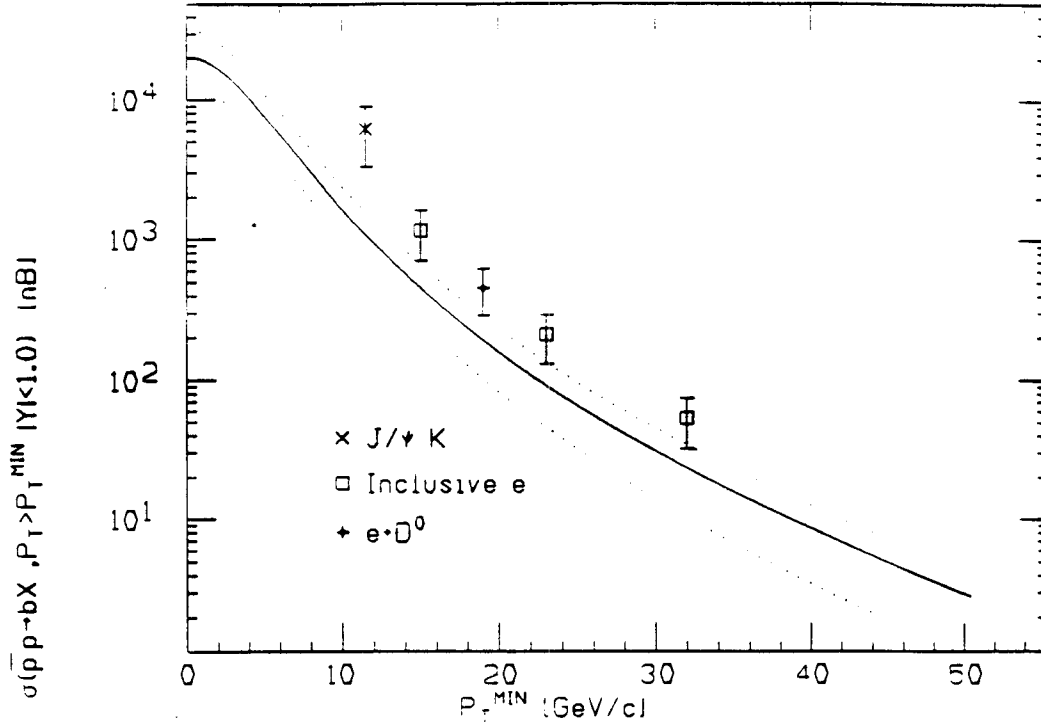
Figure 2.14: α_s^3 predictions for the b quark production cross section together with present CDF results.

	Λ (MeV)	μ	b Mass (GeV/c^2)	Structure Functions	σ(total) (μb)	$|y| < 1$	$P_T > 10\ GeV$ $|y| < 1$
Nason, *et. al.*	170	$\sqrt{m^2 + P_T{}^2}$	4.75	DFLM	-	20	2
Berger	200	$4m_b{}^2$	5	DO (set 1)	40	-	-
Berger, Collins, Soper	200	$\hat{s}$	5.4	DO (set 1)	-	6	-
Berger and Meng	200	$\sqrt{(m^2 + P_T{}^2)}$	4.75	MT ^{b}	-	15	1
Beenaker, *et. al.*	200	m_b	5	EHLQ	67	12	-
Harriman, *et. al.*	100	$m_b/2$	5	HMRS(E)	30	-	-

Table 2.3: $\mathcal{O}(\alpha_s^3)$ predictions for the b quark production cross section at the Tevatron.

measured b quark production rates and their measured values [33]. The UA1 measurements agree with the theoretical predictions within the uncertainties quoted for the calculations.

2.3.6   Theoretical Predictions for Production of t Quarks

At this time, the predicted top quark has not been observed. While upper limits on the mass of the top quark are based on theoretical grounds, the lower limits are experimental results. The current lower limits assume the validity of the theoretical predictions for top cross sections using the same parton model discussed above. An important issue is whether testing the predictions of bottom quark production can address the reliability of the predictions for top quark production.

The main difference between top and bottom production is the quark mass. The mass of the top quark has been well established to be greater than 45 GeV/c^2 by the study of Z^0 production [34]. This limit relies only on the assumption of the couplings of the top quark to the Z^0 boson. The large mass of the top quark implies that its production will be dominated by regions of much larger x than in b quark production. At the values of x which are expected to contribute to top production, the quark annihilation subprocess is expected to be dominant. Since the parton distribution functions are better known at higher x and better known for quark distribution functions than gluon distribution functions, the uncertainty in top production due to the distribution functions is expected to be much smaller than in b quark prodcution.

A study of the sensitivity to the structure functions was made in Reference [30], as discussed in the previous section. For top production, that study varied the parameters present in the HMRS structure functions to estimate a top quark production cross section uncertainty which was typically less 40% for a top quark mass between 100 and 200 GeV/c^2. Another study of the sensitivity to structure functions was made made by Ellis [35]. The
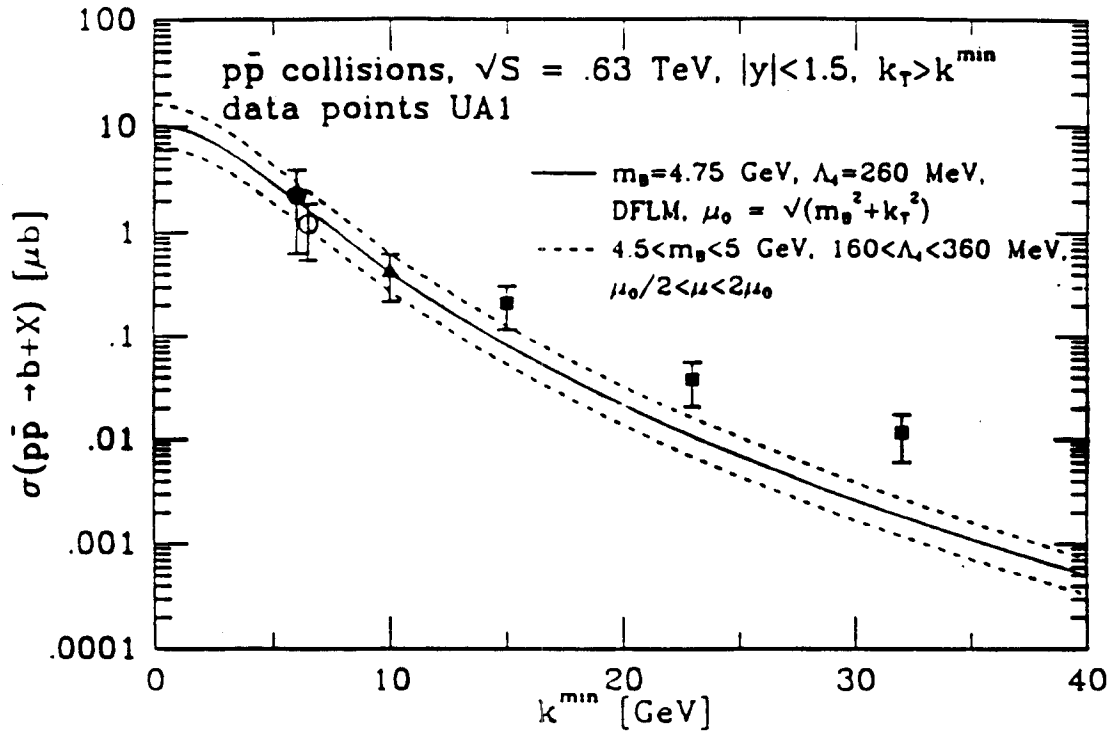
Figure 2.15: The predicted and measured α_s^3 b quark production cross section at $\sqrt{S} = 630$ GeV. The measurements were made by the UA1 collaboration [33].

study showed roughly a 10-30 % sensitivity to choices of structure functions.

Another effect of the larger top mass is that the sensitivity of the short distance cross section to the exact value of the mass should be smaller. This is because the lowest order cross section varies by $1/m_T{}^2$, where m_T is the transverse mass. This leads to a smaller sensitivity to the mass than in the case of b production.

Finally, the higher order contributions to top production are expected to be smaller. This effect is discussed in References [25] and [26] and is due to the effects on the short distance cross section from higher order processes involving the exchange of gluons. The effect leads to the presence of factors proportional to $log(m_b/s)$ which are significantly smaller for the case of top.

In summary, the calculations for top quark production are thought to be much more reliable than those for b quark production. Figure 2.16 [25] shows the predicted top production cross section showing the theoretical uncertainties obtained by variations in the Λ_{QCD} , m_t, and μ. The error band can be seen to be smaller than in the case for b production. Combined with the uncertainty due to the structure functions, the theoretical error on the top quark cross section is less than a factor of two, compared with an uncertainty of 2-3 for b quarks .

Nevertheless, the same techniques applied to the calculation of the b quark cross section are also relied on for the predicted top cross section, and therefore, a comparison of the predicted and measured b quark production cross section would provide the only available evidence that these techniques are correct. The existence of any discrepency between the predicted and measured b quark production cross section could imply that present upper limits on top quark production are conservative.
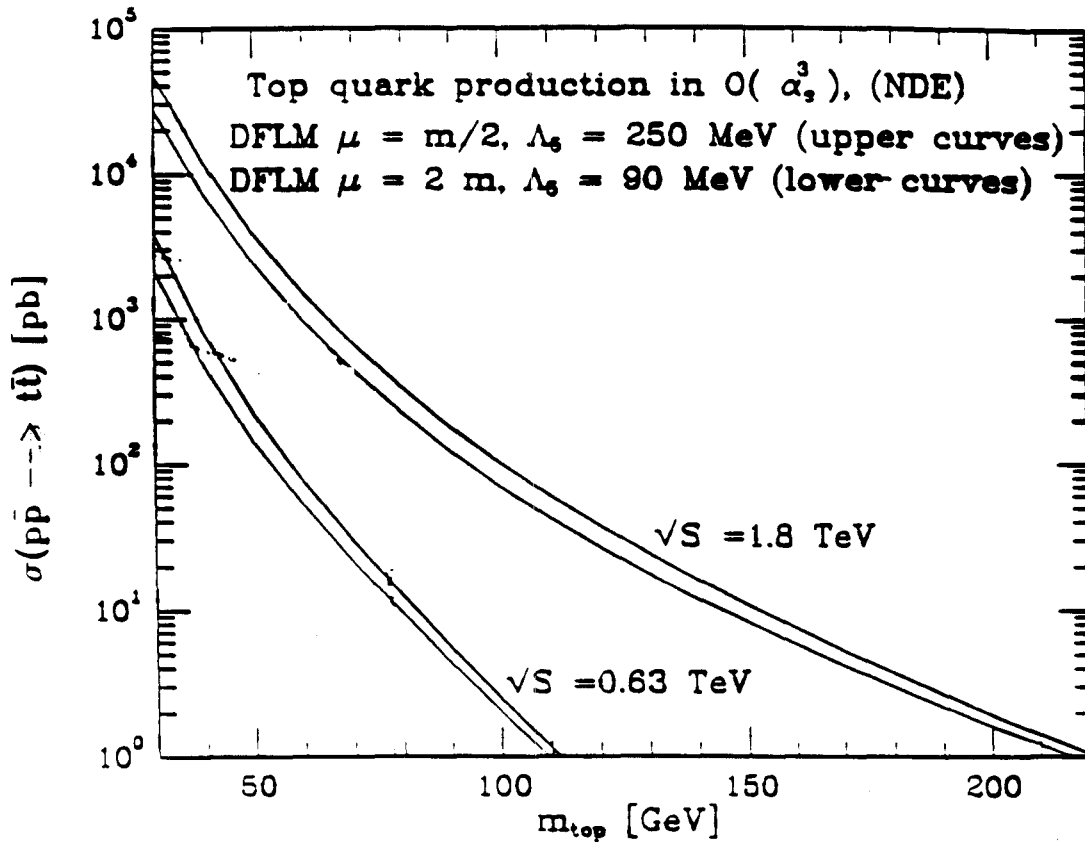
Figure 2.16: αs^3 predictions for the t quark production cross section at $\sqrt{S} = 1.8$ TeV.

Chapter 3

Experimental Setup

3.1 The Tevatron

The Tevatron was a superconducting synchrotron designed to store and collide bunches of protons and antiprotons. In addition to the Tevatron itself, a number of other particle accelerators were used to provide the protons and antiprotons and to accelerate them to sufficient energy for injection into the Tevatron. What follows is an overview of the machinery and processes by which protons and antiprotons are created, accelerated, and finally brought to collide with one another.

Figure 3.1 shows the layout of the different accelerators at Fermilab. The production of accelerated protons began with hydrogen gas. Ionized hydrogen was accelerated to 750 keV in a Cockroft-Walton electrostatic accelerator. The next stage was a linear accelerator which took the protons up to 200 MeV, followed by a synchrotron (the Booster Ring) which accelerated the protons to 8 GeV and injected them into the Main Ring. The Main Ring was a synchrotron in which protons were accelerated to either 120 GeV to be used for antiproton
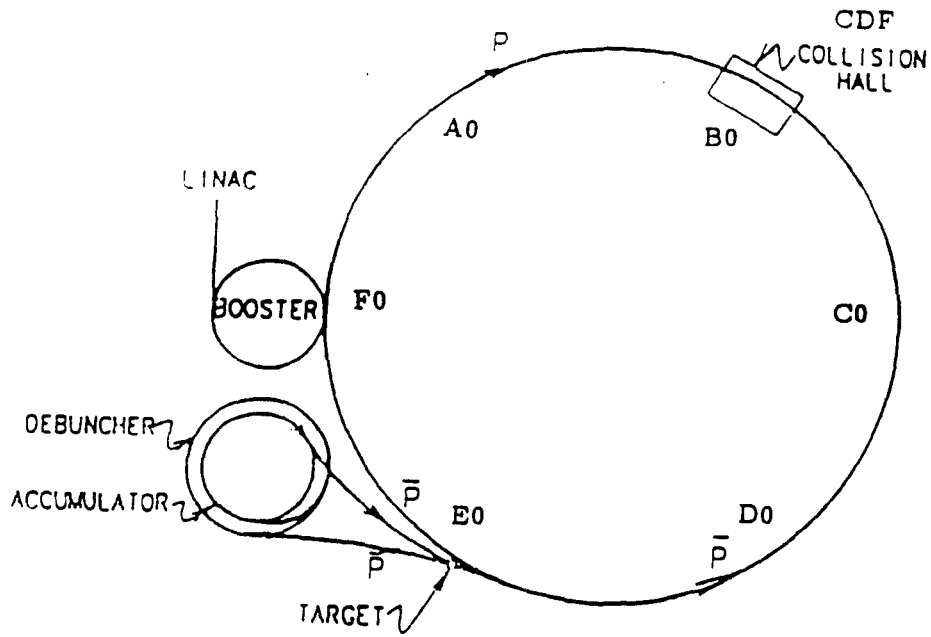
Figure 3.1: Overview of the different accelerators at the Fermi National Accelerator Laboratory (FNAL).

production or to 150 GeV for injection into the Tevatron.

Antiprotons were produced by striking a tungsten target with protons extracted from the Main Ring. The antiprotons were then focused using a lithium electromagnet. The Debuncher ring collected these antiprotons and reduced their spread in longitudinal momentum in order to improve their eventual transfer efficiency to the Main Ring. The antiprotons were then added by the Debuncher to the 'stack' being stored in the Accumulator.

Approximately 1×10^{11} $\bar{p}$'s were required for a typical 'store' of colliding beam in the Tevatron. The antiprotons in a store were delivered by the Accumulator to the Main Ring, accelerated to 150 GeV, and injected in 6 bunches into the Tevatron. The protons and antiprotons in the Tevatron were then simultaneously accelerated to 900 GeV. Quadrupole magnets were then turned on and used to focus the protons and antiprotons at the B0 collision point, the CDF location.

During typical running, 6 bunches of approximately 5 to 10×10^{10} protons were stored with 6 bunches of antiprotons each containing approximately 1 to 3×10^{10} particles. The typical luminosity during a store was $1 \times 10^{30} \mathrm{cm}^{-2} \mathrm{sec}^{-1}$ and the average store lasted about 20 hours. The Tevatron was capable of colliding beams at 6 points, listed as A0–F0 in Figure 3.1. During the 1988-1989 run, experiments were located at B0, C0, and E0.

3.2   The CDF Detector

The Collider Detector at Fermilab (CDF) was a particle detector used to observe and measure properties of particles originating in $\bar{p}p$ collisions at a center-of-mass energy of 1.8 TeV. During data taking, CDF was positioned in the B0 collision hall. Protons entered from the West and antiprotons from the East. The coordinate system defined the proton beam as the positive z axis. The positive y axis was defined to be vertical and the positive x axis pointed

away from the center of the Tevatron. Polar coordinates were defined so that the azimuthal angle, ϕ, was zero along the positive x axis and increased under a counter-clockwise rotation about the z axis. The polar angle, θ, was defined as zero relative to the positive z axis.

Figures 3.2 and 3.3 show the layout and major subsystems of CDF. The components of CDF were arranged in cylindrical fashion around the beamline. The $\bar{p}p$ collisions were normally distributed in z about the center of the detector with a width of approximately 30 cm. From the nominal collision point, particles in the central region ($|\eta| < 1$)[a] encountered the beampipe, a set of time projection chambers (the VTPC), and a wire drift chamber (the CTC). Outside the CTC was a solenoidal magnet which provided a 1.41 T magnetic field in the $-z$ direction. The solenoid was followed by electromagnetic and hadronic calorimetry. Outside of the calorimetry were muon chambers.

3.2.1 The Vertex Time Projection Chamber

The Vertex Time Projection Chamber (VTPC) was designed to track charged particles in the r-z plane close to the interaction point. It was used to find the location of the primary interaction point along the z axis.

The VTPC consisted of a set of 8 individual time projection chambers (Fig. 3.4). Particles traversing the chambers ionized the gas in the chamber (50-50 argon/ethane). The associated electrons drifted toward a set of wires and cathode pads, from which signals were subsequently read out. Individual chambers were subdivided azimuthally into octants. The radial and beamline location of each wire together with the drift time of charge to the wire allowed reconstruction of tracks in the r-z plane.

Reconstructed tracks in the VTPC were parametrized by the polar angle θ and the

---

[a] η is defined as $ln(cot\frac{\theta}{2})$

CENTRAL DETECTOR

26 2 meters

BACKWARD ELECTROMAGNETIC
AND HADRONIC CALORIMETERS

FORWARD MAGNETIZED
STEEL TOROIDS

BACKWARD MAGNETIZED
STEEL TOROIDS

FORWARD ELECTROMAGNETIC
AND HADRONIC CALORIMETERS

CW BETA QUADS
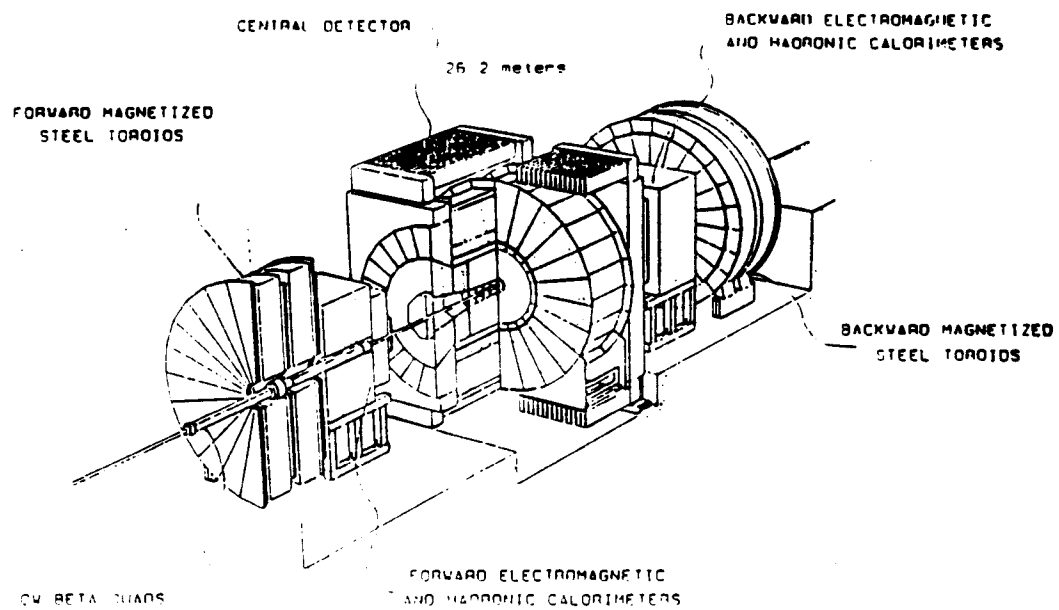
Figure 3.2: Perspective view of CDF showing both the forward and central components of the detector.

ELEVATION VIEW LOOKING SOUTH
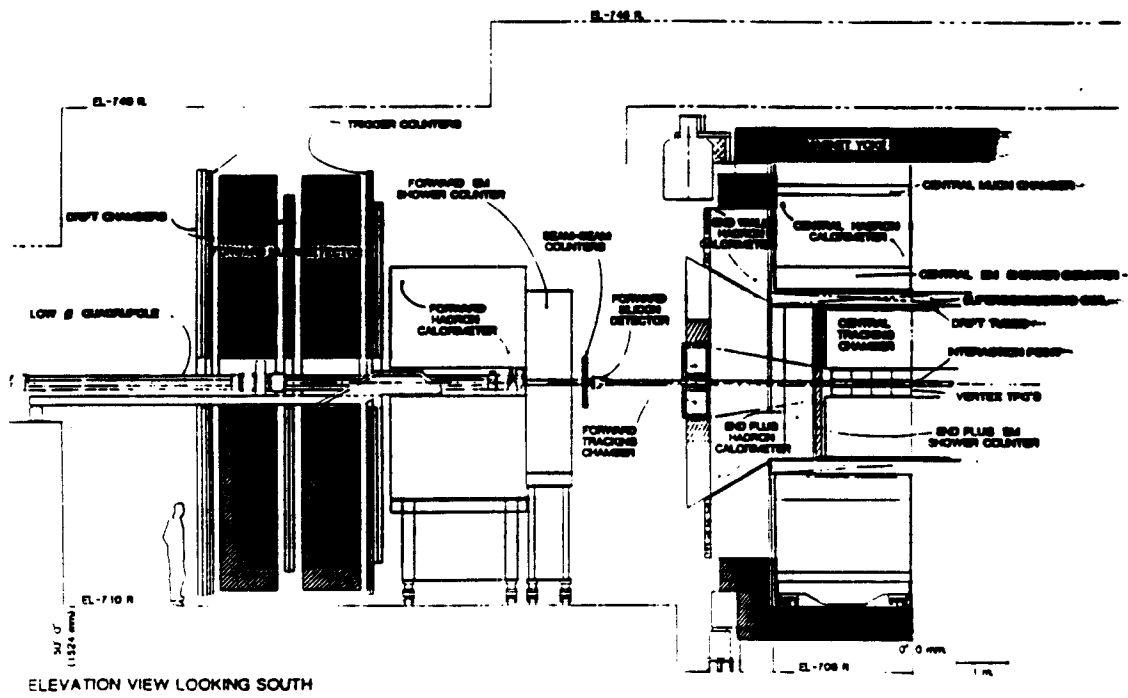
Figure 3.3: Cross sectional view of one half of the CDF detector.

intercept with the z axis. Primary vertices were located by identifying clusters of z intercepts from several tracks. The VTPC could find the z vertex with a resolution of about 2 mm. Figure 3.5 shows the distribution of the z position of primary vertices for a typical CDF data sample. The large width of this distribution (a gaussian fit gives $\sigma = 30$ cm) illustrates the need of determining the z position of primary interactions on an event-by-event basis.

3.2.2 The Central Tracking Chamber

The Central Tracking Chamber (CTC) was a drift chamber which provided charged particle tracking in 3 dimensions (Fig. 3.6). Because momentum measurement from the CTC formed an important component of this analysis, a detailed description of both the mechanical layout and general aspects of the CTC's performance are presented in this section.

Mechanical Layout

The chamber covered the region $|\eta| < 1$ at its outer radius and was cylindrically symmetric, allowing full azimuthal coverage. The CTC included axial and stereo wires and was contained within a solenoidal magnetic field which caused charged particles to follow helical trajectories. The sense wires of the CTC were grouped into nine superlayers, and within each superlayer the wires were further grouped into cells. The sense wires of five superlayers were parallel to the z axis. These were referred to as axial superlayers. The remaining four superlayers consisted of wires with a 3° tilt to provide z information and were called stereo superlayers. The axial and stereo superlayers alternated, with the innermost superlayer being an axial superlayer.

Each cell within a superlayer consisted of field wires , sense wires, potential wires, guard wires, and shaper wires (Fig. 3.7). The field wires provided an electrostatic field of approximately 1350 V/cm. Charged particles left an ionization trail in the gas (50-50 argon-ethane

SENSE WIRES

SENSE WIRE READ-OUT

CATHODE PADS

CENTER HV GRID

CARBON FIBER OCTAGON

RADIAL BOARD

CARBON FIBER OCTAGON

INNER FIELD GRID

PAD READ-OUT

DRIFT

DRIFT

PWC CATHODE GRID

OUTER FIELD CAGE

RESISTIVE DIVIDER
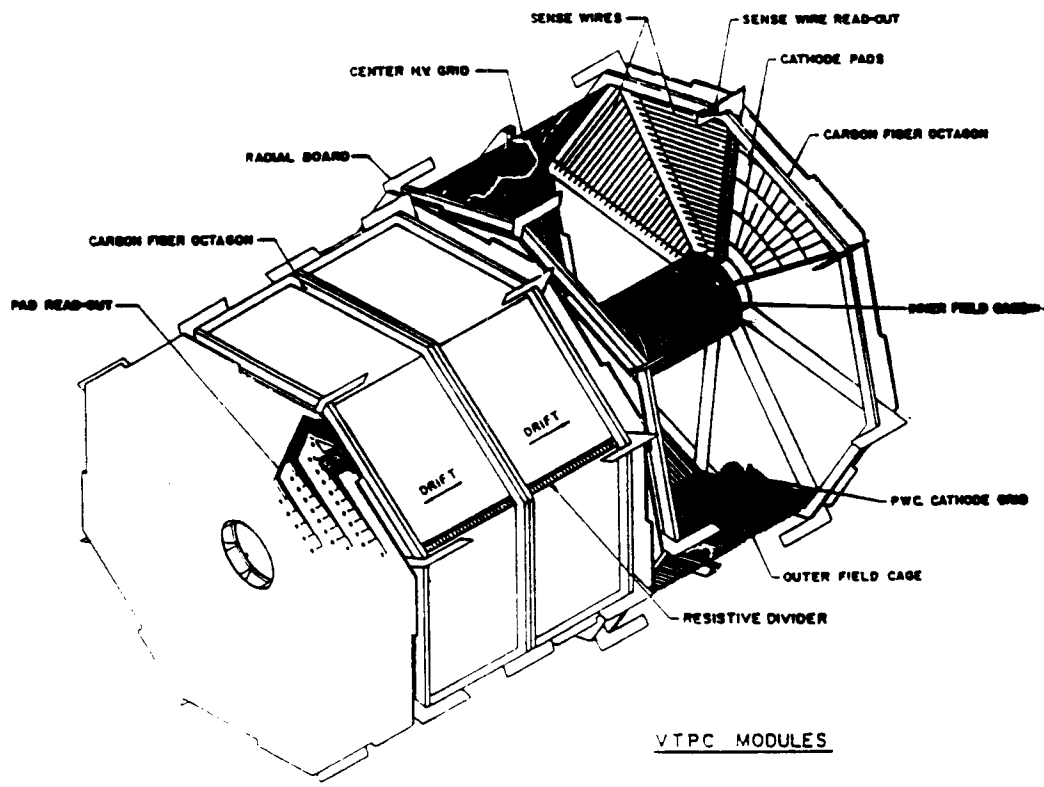
VTPC MODULES

Figure 3.4: Isometric view of two VTPC modules.
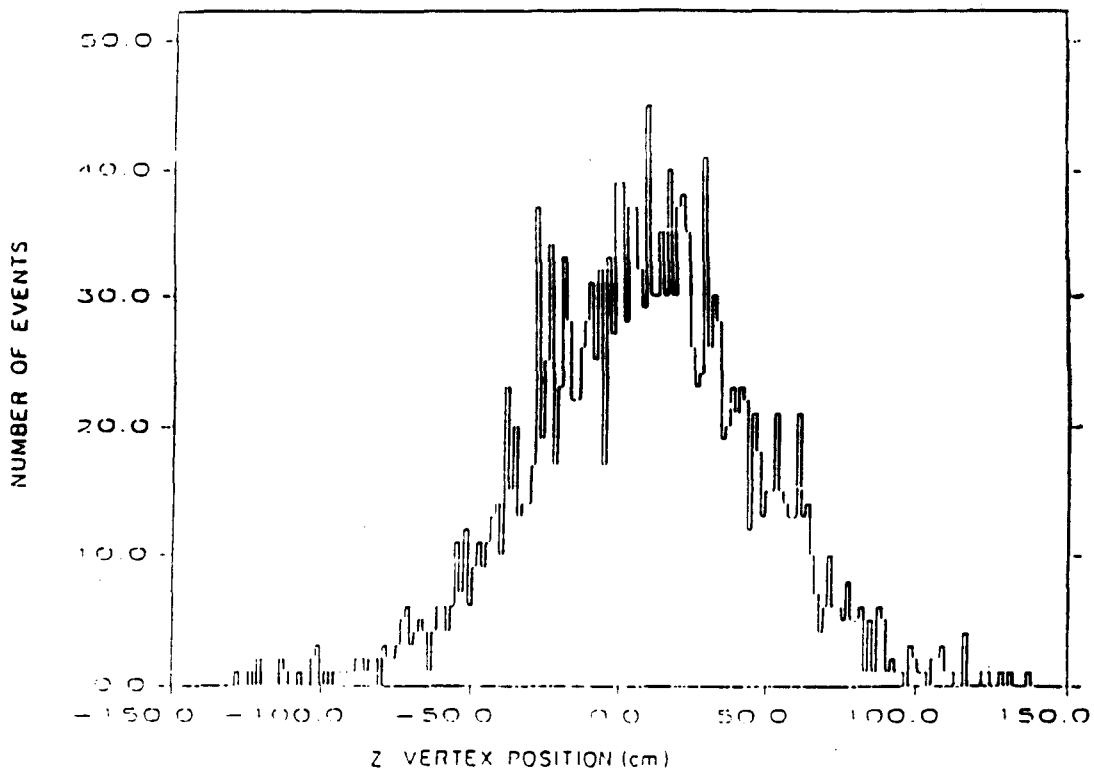
Figure 3.5: Distribution of the z location of primary vertices for a typical CDF run.

with a small percentage of alcohol). The electrostatic and magnetic fields in the chamber caused the charge to drift toward the sense wires. The potential wires allowed the gas gain to be controlled near the sense wires. The guard and shaper wires were used to 'fine tune' the electric field.

The axial superlayers had twelve sense wires and the stereo superlayers had six sense wires. The wire planes within a cell were rotated by 45° relative to the radial direction to accommodate a subtlety of the charge drift. In the presence of a magnetic and electrostatic fields, the drift velocity of charged particles have a component parallel to the electrostatic field and a component in the direction of $\bar{E} \times \bar{B}$ [36]. The net drift velocity forms an angle relative to the electrostatic field given by [37]

$$tan\beta = \frac{vB}{kE},$$

(3.1)

where v is the drift velocity with no magnetic field and k is a parameter which depends on the particular gas used in the drift chamber. Under normal operating conditions in the CTC, k was approximately 0.7, resulting in a Lorentz angle of $\sim 45°$. Figure 3.8 shows the resulting drift trajectories in the CTC. The precise value of the angle could be adjusted by varying the electrostatic field. The 45° tilt of the wire planes was chosen to allow the drift trajectories to be approximately azimuthal. This feature simplified track reconstruction and ensured that every stiff track crossed each superlayer such that the drift time to at least one wire in the superlayer was less than 40 nsec. This last feature was exploited in the implementation of a fast hardware trackfinder (the CFT) discussed in Section 3.2.6.

Figure 3.9 shows the components of the CTC readout electronics. The signals from the sense wires were input into a preamplifier card which was mounted on the CTC endplate. A resistor network on the preamplifier card reduced cross talk between neighboring sense wires to about 1%. The preamplifier output signal (typically 40 mV) was then sent to

Amplifier-Shaper-Discriminator (ASD) cards which were mounted on the outside of the detector.

The ASD's produced an ECL logic level signal of time duration proportional to the time over threshold of the CTC pulse. The ASD's also produced an amplified and filtered analog signal. The ECL signals were used by LeCroy 1879 FASTBUS TDC's to produce a digital output proportional to the time over threshold. Finally, the digitized output of the TDC's was read out by the CDF data aquisition system, which is described in more detail in Section 3.2.7.

Tracking in the CTC

The process of finding tracks in the CTC consisted of three steps, all of which were achieved offline. In the first step, a list of hits and associated drift times was established. Next, a process known as *pattern recognition* attempted to group hits which originated from a single particle. The result of the pattern recognition was a list of tracks and the hits which formed them. Individual hits were allowed to be associated with more than one track.

The third step in reconstructing tracks was to fit the hits of a given track to a helix. The complete specification of a helix requires five parameters. Conventionally, the parameters chosen are

- z_0 - The z position at the point of closest approach of the helix to the origin ($x = 0, y = 0, z = 0$).

- d_0 - The distance of closest approach to the origin in the $x - y$ plane.

- ϕ_0 - The azimuthal angle relative to the positive x axis at the point of closest approach to the origin.

- c - The half-radius of curvature. The half-radius of curvature is directly related to P_T

by the relation

$$\mathrm{P}_T = \frac{0.000149898 \, B}{c}$$

where B is the magnetic field in Tesla and P_T is in GeV/c.

- *cotθ* - The cotangent of the polar angle at the point of closest approach to the origin.

There were several different types of track fits relevant to this analysis. Their use is discussed in Chapter 4. Briefly, the fit options were:

Unconstrained In this type of fit, the only information used was that provided by the hits themselves. This included the location of hits and their residuals relative to the fit. The latter were incorporated by performing the fits in an iterative fashion and weighting the hits by the inverse of the residuals.

Beam Constrained This type of fit constrained tracks to originate in the *x-y* plane at the same point as the beam axis.

Mass Constrained This type of fit constrained some set of tracks to have originated from the decay of a particle of known mass.

Vertex Constrained This fit constrained a set of tracks to have originated from a common vertex. The constraint could be imposed in the *x-y* plane only or in all three dimensions.

Aspects of the CTC performance were studied using both cosmic ray data and p̄p data. Studies of cosmic ray data indicated that the spatial resolution of the sense wires was approximately 155 μ and that the P_T resolution of the chamber was approximately $\sigma/\mathrm{P}_T = 0.002\mathrm{P}_T$. Data from p̄p events differed from cosmic rays in that ~ 30 tracks were present in a typical event. The effect of these high track multiplicities on the CTC performance

will be detailed in Section 4.2. Additionally, the different fitting constraints described above improved the P_T resolution. The improvement was manifested as an improvement in the mass resolution of J/ψ and B^0 candidates. This will also be discussed in Section 4.2.

3.2.3 Calorimetry

CDF had both electromagnetic and hadronic sampling calorimetry covering almost 4π steradians of solid angle. The calorimetry in the central region was divided into four arches (see Figure 3.2). Each arch covered $180°$ in ϕ. Two arches on the East end of CDF covered the region $0 < \eta < 1.1$ while those on the West end covered the region $0. > \eta > -1.1$ An arch was composed of twelve wedges, each subtending $15°$ in ϕ. Each wedge was further subdivided into towers, each of which subtended 0.1 units of η. In the central region, the electromagnetic calorimeters (CEM) consisted of alternating sheets of lead and scintillator. Light originating in the scintillators was transported by light pipes to photomultiplier tubes. The CEM had a resolution of $\sigma_E/E = 13.5\%/\sqrt{E}$. The hadronic calorimeters (Central Hadron Calorimeter or CHA) used layers of steel alternated with sheets of plastic scintillator. As with the CEM, light signals originating in the scintillator were detected by photomultiplier tubes. The energy resolution (σ_E/E) of the CHA was measured to be $70\%/\sqrt{E}$ with E measured in GeV.

3.2.4 Central Muon Chambers

Outside of the calorimetry were the Central Muon Chambers (CMU). As seen in Figure 3.10, there were three chambers mounted into each calorimetry wedge at the same radius. Each of these chambers contained 16 drift cells operated in limited streamer mode. The drift cells within each chamber were arranged in four radial layers with four cells at the same radius within each layer. Each layer of a chamber contained two sense wires and each wire was
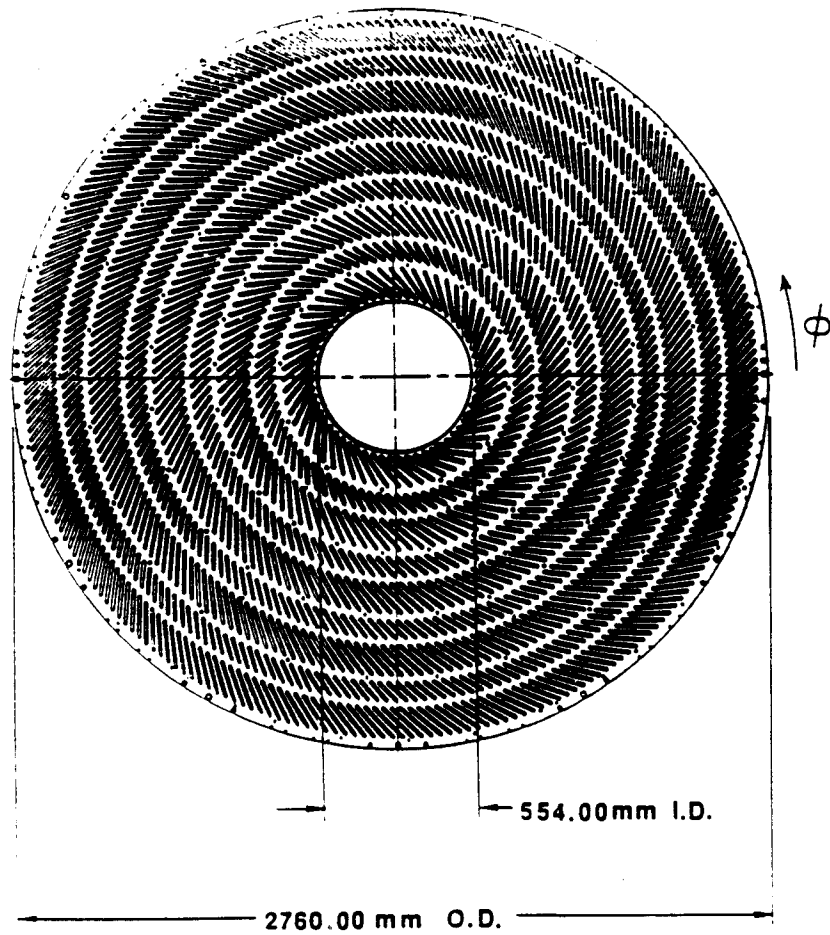
Figure 3.6: Cross sectional view of the CTC endplate showing both axial and stereo wire locations.
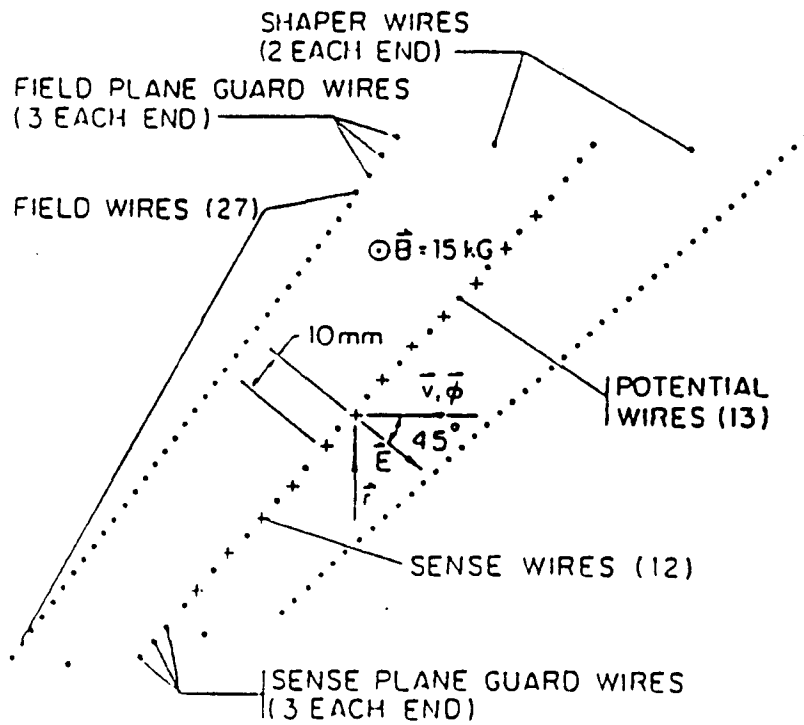
Figure 3.7: CTC wire configuration within an axial layer.
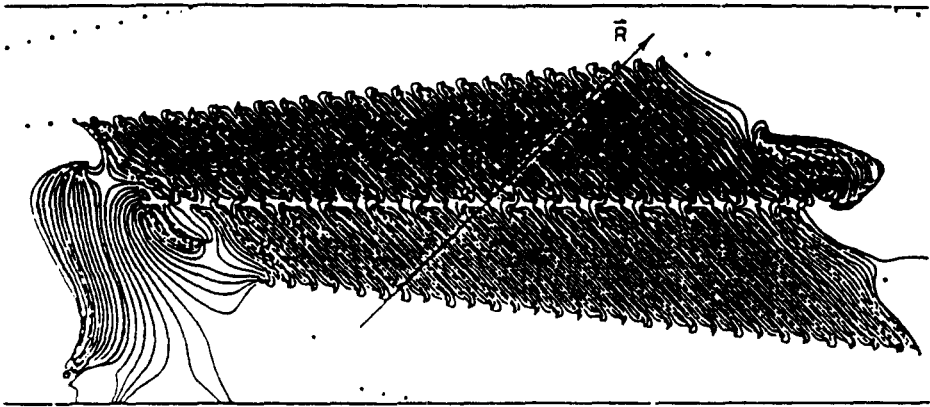
Figure 3.8: Drift trajectories within an axial CTC supercell.
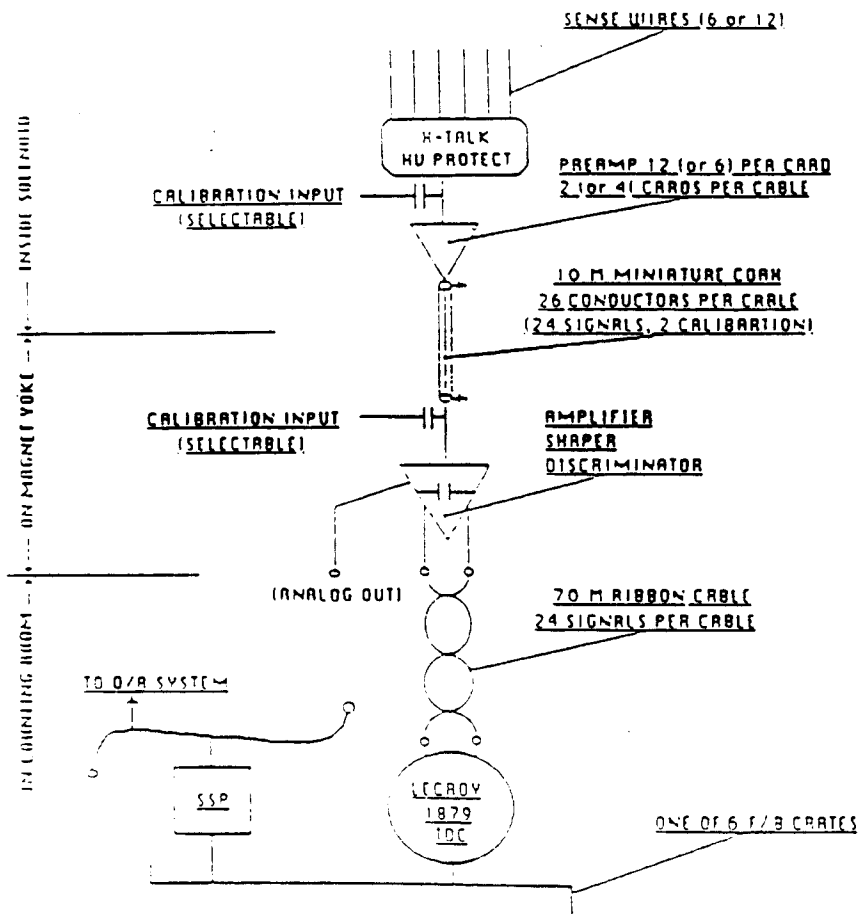
Figure 3.9: Overview of CTC readout electronics.

used in two cells (see Figure 3.11). Wires in alternating layers were offset from one another by 2 mm to resolve the left-right ambiguity.

The CMU served to trigger on and identify muon candidates. Muons traversing the central calorimetry interacted only through ionization, depositing approximately 1.5 GeV in the calorimeters before being detected by the muon chambers. Other particles such as hadrons and electrons were not usually minimum ionizing and produced showers of particles which were absorbed within the calorimetry.

Tracks or 'stubs' reconstructed in the CMU provided a rough measurement of a candidate muon's transverse momentum. Figures 3.11 and 3.12 show the geometry by which the P_T of a muon was related to the differences in drift times for the sense wires in the CMU. If α is the angle between a particle track outside the magnetic field and a radial line through a pair of sense wires, then

$$\alpha \approx \frac{v\Delta t}{H},$$
(3.2)

where v is the drift velocity of the electrons from the ionized gas in the CMU, Δt is the difference in drift times to the sense wires in layers 1 and 3 or 2 and 4, and H is the separation (55.0 mm) between the radial layers. From Figure 3.12, the angle α can also be related to P_T by

$$\alpha \approx sin\alpha = \frac{eL^2B}{2DP_T},$$
(3.3)

where L is the radius (1440 mm) of the solenoid, D is the inner radius (3470 mm) of the CMU, B is the magnetic field strength(1.41 T), and e is the charge of the muon in units of the electron charge. Combining Equations 3.2 and 3.3 yields

$$P_T = \frac{164 \text{ nsec GeV/c}}{\Delta t}.$$
(3.4)

The difference in drift times for the wires thus provided a measurement of P_T . This difference in drift times was utilized by the trigger system to identify muon candidates.

The drift times and pulse heights from the muon chambers were read out and converted to analog voltages by the CMU front end electronics. The front end of the CMU readout electronics consisted of several modules contained within RABBIT[b] crates. The Muon ADC/TDC (MAT) modules[c] were responsible for reading out the drift times and pulse heights from the sense wires. The analog signal from each cell was integrated by charge integrators in the MAT. This information provided a measurement of the z position of stubs using capacitive charge division.

Drift times were converted to analog signals by Time-to-Voltage converters (1 per wire) in the MAT cards. These drift times were subsequently used by the Muon Trigger (MTRG) cards which checked for muon candidates. The existence of muon stubs with P_T above preset and adjustable thresholds was reported to the other components of the trigger system (see Section 3.2.6).

3.2.5 Beam-Beam Counters

In the far forward regions of CDF, planes of scintillators called the Beam-Beam Counters (BBC's) signaled the presence of an inelastic $\bar{p}p$ collision. The BBC's covered the angular region $0.32° < \theta < 4.47°$ and were located 5.8 m from the nominal interaction point. Figure 3.13 shows one plane of the BBC's. The BBC's constituted the first stage of the trigger system by requiring at least one counter in both the East and West planes to have fired within a 15 nsec window centered on the beam crossing time.

The BBC's also served as luminosity monitors. The luminosity was calculated from the

---

[b]The RABBIT or Redundant Analog Bus Based Information Transfer system was a set of custom designed crates made at Fermilab which contained the required dynamic signal range needed by CDF and not typically achieved in the more standard FASTBUS system.

[c]The name MAT is misleading since it did not actually perform any digitization. The circuits within a MAT card performed charge integration and time to voltage conversion.
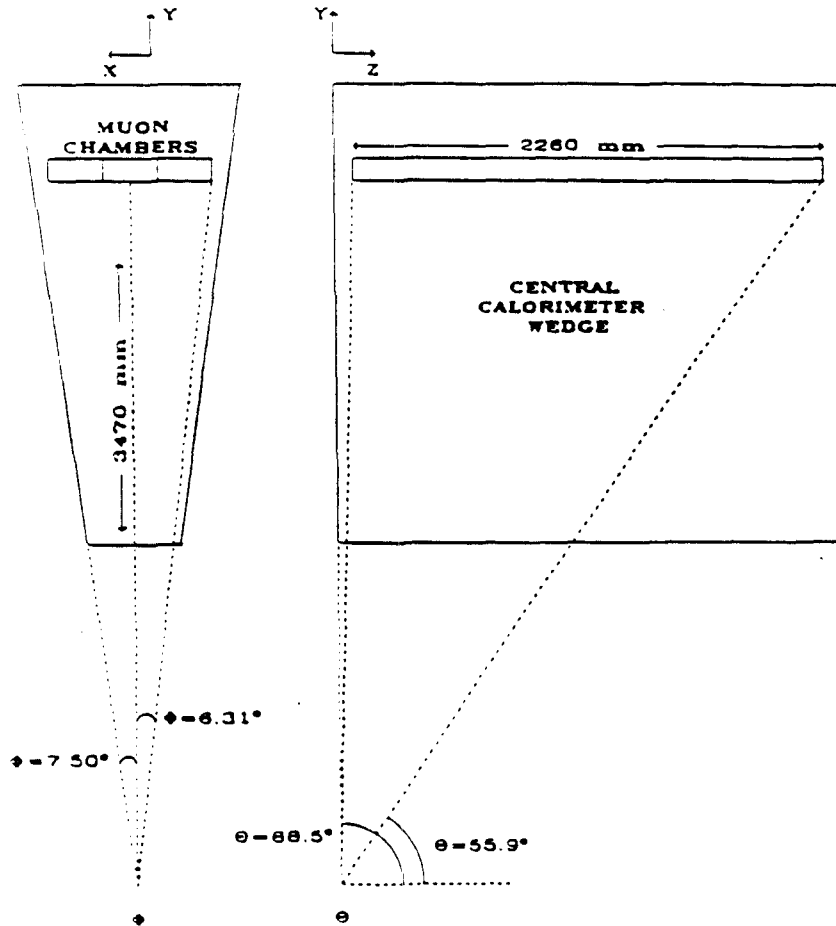
Figure 3.10: Central Muon Chambers for a single CDF wedge.
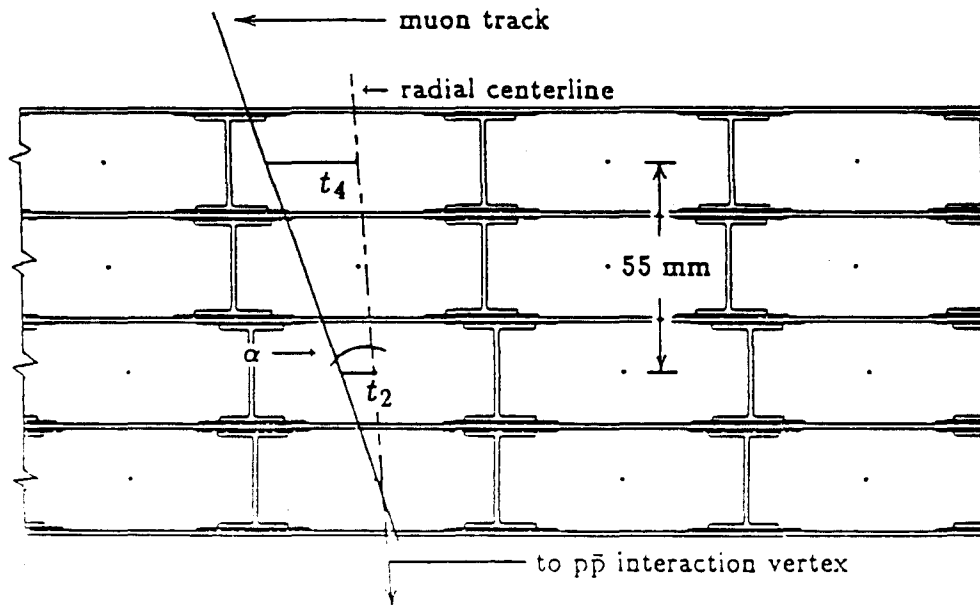
Figure 3.11: Detail of a single muon chamber in the x-y plane showing an incident muon. Every other cell in a single layer used the same sense wire. The angle α was directly related to differences in drift times. The drift time differences were then used to signal the presence of muons candidates.
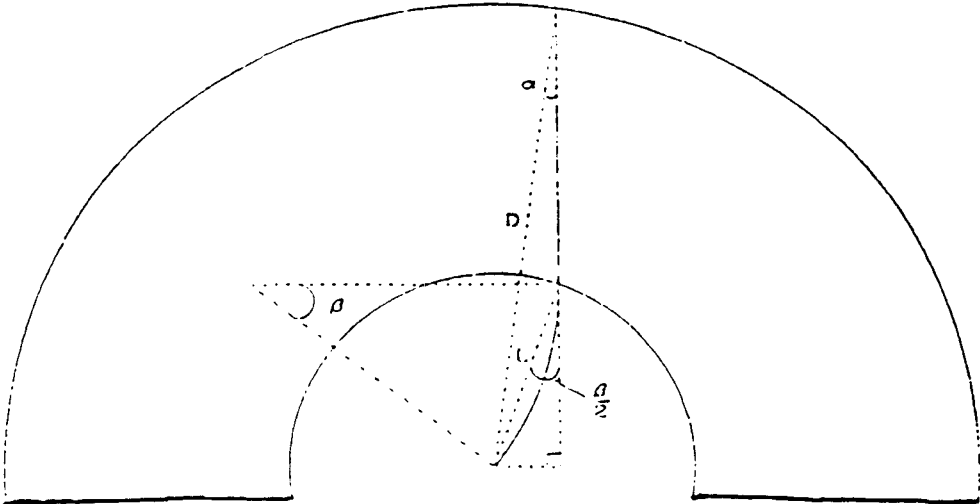
Figure 3.12: Geometry relating muon P_T to angle of incidence at CMU.

BBC hit rate and the effective cross section for the BBC's (σ_{BBC}):

$$\int \mathcal{L} dt = \frac{\int R_{BBC} dt}{\sigma_{BBC}}$$

where R_{BBC} is the BBC coincidence rate and $\mathcal{L}$ is the instantaneous luminosity. The effective BBC cross section, σ_{BBC}, was measured by comparing the BBC rate at $\sqrt{s} = 546$ GeV to that at 1800 GeV [38]. The ratio of these rates was proportional to the ratio of the effective BBC cross sections at the two energies. The normalization of σ_{BBC} at 546 GeV was determined from measurements by the UA4 experiment [39] and by direct calculation using accelerator parameters. A value of $\sigma_{BBC} = 47.0 \pm 2.21 \pm 2.17$ mb was obtained for the effective cross section at 1800 GeV. The first error represents the error due to the uncertainty of σ_{BBC} at 546 GeV and the second error is due to the uncertainty in the luminosity ratios in the measurements of the relative rates at the two energies. The overall uncertainty in the luminosity at 1800 GeV was about 6.6%.

3.2.6 The CDF Trigger

A critical component of any experiment using hadronic collisions is the trigger because only a small fraction of all interactions are recorded on tape. The rate of inelastic collisions at Tevatron energies and at a typical luminosity of 1×10^{30} cm^{-2}sec^{-1} was approximately 50 kHz but could be recorded at rates of only about 1 Hz. In order to record events at a manageable rate, CDF designed a multilevel trigger to find the hard collisions by identifying high energy gammas, electrons, muons, or jets. The trigger was composed of four stages, or levels. A detailed description of these levels is provided in the following sections, but first a brief sketch of their function is given here.

Each successive level of the trigger system reduced the event rate using data from individual subsystems of the CDF detector. The Level 0 trigger was designed to detect a
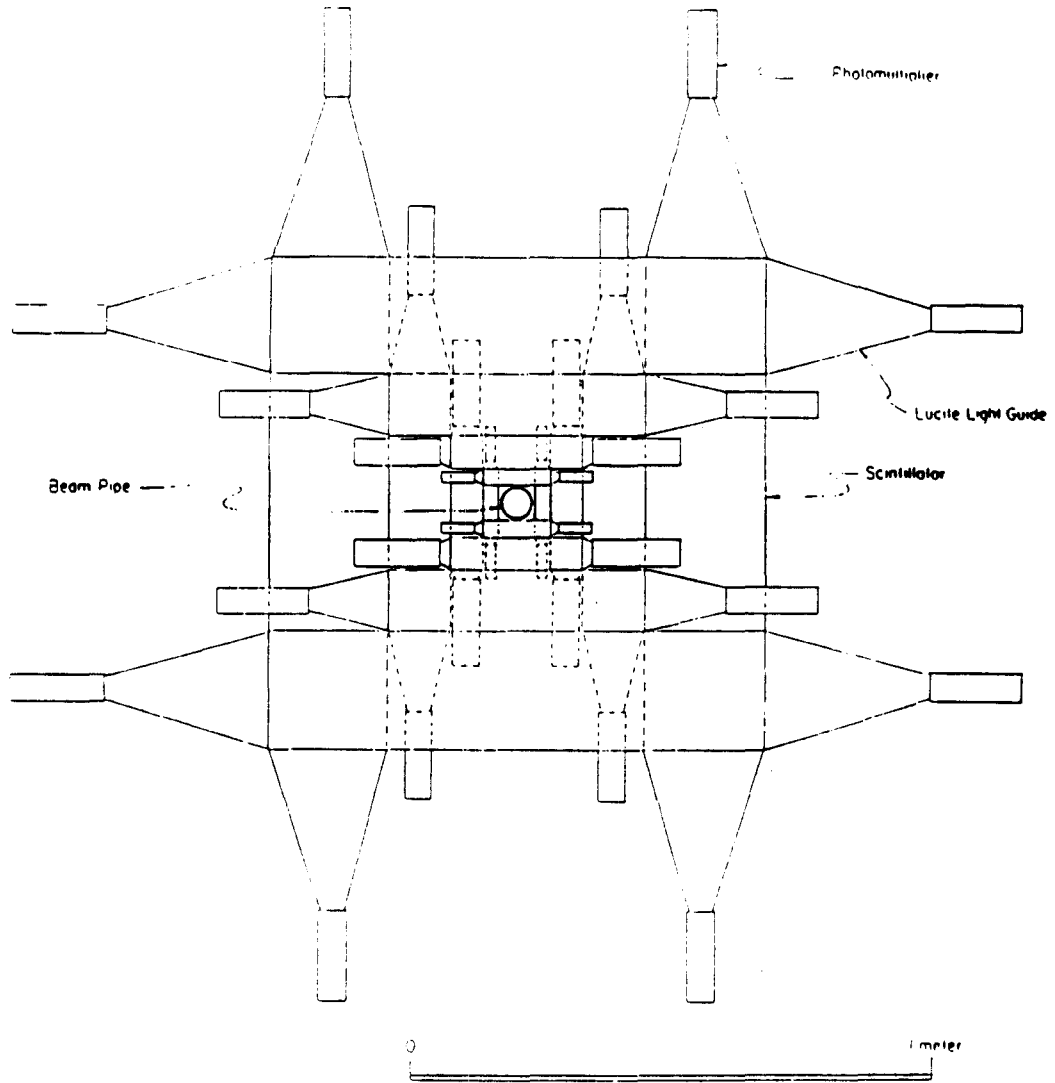
Figure 3.13: One set of Beam-Beam Counters.

hard p̄p collision identified by simultaneous hits in the East and West planes of the BBC's. The Level 1 trigger utilized the most rapidly available data from the calorimetry and muon chambers to reduce the accepted event rate to about 1 kHz. The Level 1 trigger was also responsible for finding stiff tracks in the CTC with which the Level 2 trigger identified electron and muon candidates. The Level 2 trigger accepted events based on clusters of energy in the calorimetry and on the presence of electron and muon candidates, reducing the event rate to less than 10 Hz. After satisfying a Level 2 trigger, events were digitized and read out, or scanned, into event memory buffers. The data contained within these buffers was filtered by the Level 3 trigger and written to magnetic tape at approximately 1 Hz.

The CDF trigger required coordination between the detector front end electronics and the trigger components. This included, for example, preventing the front end electronics from being reset while the trigger system was still making a decision about an event. Additionally, it was important to synchronize the activities of the different trigger components in order to minimize any potential dead time. The timing and synchronization of the trigger system was provided by the Timing Control modules. These were a set of FASTBUS modules which included a master clock and a memory containing the different instructions specifying the required timing sequences. Figure 3.14 shows the different components used at Levels 0–2.

Level 0

The Level 0 trigger was provided by the Beam-Beam Counters. Output signals from the phototubes attached to the BBC scintillators were sent to the Level 0 trigger electronics. The Level 0 trigger was provided by latching the signal from each scintillator with a gate coinciding with the time at which outgoing particles were expected to strike the BBC's. This gate was generated by modules used to monitor the Tevatron. Hits in both the East and West BBC's which coincided with this gate produced a Level 0 accept, which was required

Figure 3.14: Overview of components in the CDF trigger system (Levels 0–2).

for all Level 1 triggers.

Level 1

There were three types of information available on which the Level 1 trigger decision was based. This information was composed of data from the calorimetry and muon chambers. The Level 1 trigger was designed to process signals and make a decision within the 3.5 μsec between beam crossings. In this section, the operation of the calorimetry and muon triggers is provided, followed by an overview of the Central Fast Tracker.

The Level 1 calorimetry triggers were based on the total transverse energy (E_T) detected by pairs of individual calorimeter towers with signals above preset thresholds. Thresholds were implemented separately for electromagnetic, hadronic, and total E_T to help distinguish electron and photon candidates from jet activity. A succession of FASTBUS modules combined the analog output of these calorimeter towers into digital sums of the energy deposited in the calorimetry. Comparisons of these digital sums to the thresholds set for the different triggers determined whether the trigger was satisfied. The steps involved in the operation of the Level 1 calorimetry triggers are sketched below.

During initial processing, calorimetry signals added together and amplified the analog signals from pairs of individual calorimeter towers, subtracted pedestals, and corrected output signals for gain variations. By adding calorimeter towers pairwise, the number of signals was reduced thereby improving the manageability of the system. In the central region the analog signals came from phototubes attached to the scintillator plastic within the calorimeter, and a pair of towers subtended 0.2 units of pseudorapidity.

The next step in the Level 1 processing was to sum the outputs from those pairs of towers which were above a preset threshold. This summation isolated those towers which contained a signal which was above noise levels. The sums were formed for five different regions of

pseudorapidity covered individually by the central, forward, and plug calorimeters. Sums for the forward and plug calorimetry were divided into eastern and western components. Ten sums (five regions of pseudorapidity for hadronic and electromagnetic calorimeters separately) were formed for each of four possible thresholds. The different thresholds allowed the definition of different triggers, each using a different threshold.

The third step in the Level 1 processing was to digitize the analog sums, form grand sums of the total, hadronic, and electromagnetic transverse energies, and compare the grand sums to preset thresholds. Again, this step was repeated a total of four times, once for each of the four thresholds employed during the analog summation. The grand sums included the digitized data from all five regions of pseudorapidity. Grand sums for electromagnetic, hadronic, and total E_T were compared to corresponding thresholds which defined a specific trigger. The results of the three comparisons were OR'd together to yield a single pass or fail result. The output of this step in the Level 1 processing was thus a set of four bits, each corresponding to one of the four analog thresholds. These four bits were utilized in the final Level 1 trigger decision discussed below.

The Level 1 central muon trigger was based on the drift time measurements in the CMU. As discussed previously, the differences in drift times from individual wires provided a measurement of the transverse momentum of CMU stubs. The drift times for pairs of wires (see Figure 3.12) were input to the Muon Trigger (MTRG) cards. The MTRG card generated a gate for each wire with a programmable time duration relative to the arrival time of the signal from the Muon ADC/TDC (MAT) card. A trigger was generated if the gates from both wires of a pair overlapped.

The Level 1 trigger was also responsible for finding stiff tracks using the Central Fast Tracker (CFT). This information was used in some of the Level 2 triggers to identify electron and muon candidates. The CFT was a FASTBUS module which relied on the fact that stiff

tracks had ionization drift times of less than 40 nsec for at least one wire in each superlayer of the CTC. The CFT then used lookup tables which contained the bit patterns of hits corresponding to tracks within some region of P_T .

The final trigger decision at Level 1 was made by the 'Fred' [d] module. This module received signals from the calorimeter and muon trigger electronics indicating whether individual trigger requirements had been satisfied. The Level 1 trigger decision was made by comparing the trigger information with lookup tables contained in 4k RAM. The Fred module contained several such tables allowing for prescaling of different patterns. The trigger accept signal was then generated from the logical OR of the decisions made within each table. If a trigger was passed, the Fred module then communicated this to the Trigger Supervisor module which prevented the front end electronics from being reset until a Level 2 accept or reject was received. The allowed Level 1 accept rate was 1 kHz

Level 2

The Level 2 trigger was used to reduce the rate of accepted events to less than 10 Hz. The acceptance of an event by Level 2 initiated the readout of data from the entire detector into data buffers (see Section 3.2.7). With scan times of less than 10 msec, the deadtime incurred by the Level 2 trigger was less than 10%.

The decision to accept an event at Level 2 was based on calorimetry, tracking, and muon information. A description of how this information was included in the Level 2 trigger decision is discussed in this section.

The Level 2 calorimetry triggers were based on clusters of towers with energies above preset and adjustable thresholds. These clusters were formed by a FASTBUS module (the Cluster Finder) from the towers determined by the Level 1 trigger to have been above a

---

[d]The name 'Fred' was not an acronym, but was a name chosen to refer to this piece of hardware.

certain threshold. After all clusters were found, their energy and location were digitized and sent to the Level 2 processors as two 64 bit words. One word contained data corresponding to the electromagnetic transverse energy and one word contained data corresponding to the total transverse energy. The Level 2 processors are described below.

Electron triggers were formed by combining identified CFT tracks with clusters of electromagnetic energy. The CFT track processor monitored the locations of the calorimetry clusters found by the Cluster Finder. When the coordinates of a cluster matched that of a stiff track, the presence of the track and its momentum were encoded as part of a third 64 bit word which was sent to the Level 2 processors with the data from the energy clusters described above.

The Level 2 central muon triggers were based on matching of CFT tracks to stubs in the CMU. The matching of stiff tracks with muon stubs was accomplished in a set of Muon Level 2 Trigger (MU2T) modules. There was one MU2T module for each CMU wedge and the collection of MU2T modules was referred to as the Muon Matchbox.

A matched muon (also called a gold muon) was identified by extrapolating the CFT track to the CMU. If the track extrapolated to the chamber containing a stub or to the chambers on either side of the stub then the CFT track and the CMU stub were combined to define a gold muon. The list of gold muons and their momentum information was then sent to the Level 2 processors.

The Level 2 processors determined the number and characteristics of the different energy clusters, electron candidates and gold muons. There were three types of processors. The first type of processor was the Cluster Memory module which stored digitized data from the Cluster Finder, Muon Matchbox, and CFT. As stated previously, this data was in the form of three 64 bit words. The first two words described the energy deposited in the calorimetry by the cluster and the last word indicated the presence and momentum of CFT

tracks (electron candidates) and gold muons. Note that the format of these three words did not depend on whether the cluster originated from the calorimeters or the muon chambers.

The second type of Level 2 processor was called a Mercury module. These modules analyzed data stored in the Cluster Memory modules, calculating simple characteristics of each type of cluster. Different Mercury modules were dedicated to specific types of physics objects. For instance, the Mercury-Electron module was designed to look for candidate electrons. It calculated quantities such as the ratio of electromagnetic to total E_T in a cluster or checked for the presence of a CFT track with some minimum P_T .

The final set of Level 2 processors were the Jupiter modules. The Jupiter modules received the results of the Mercury module calculations and determined if the requirements of individual triggers were satisfied. The requirements of each trigger was compared with the Mercury module data by programmable microprocessors located on the Jupiter modules. The output from the Jupiter modules was a sequence of bits corresponding to the success or failure of each individual trigger. This information was sent to the Fred module for the final Level 2 decision.

As in Level 1, the Fred module decided whether to accept the event as having passed Level 2 or whether to reject it. By its design, the Fred module was able to make decisions for either Level 1 or Level 2. At Level 2, this decision was based on the results of the Jupiter modules. The Fred module formed the logical OR of each individual trigger result determined by the Jupiter modules. Examples of individual Level 2 triggers from a typical run included:

JET_60 Required a calorimeter cluster with E_T above 60 GeV.

TOTAL_ET_150 Required E_T summed over all calorimeters to above 150 GeV.

PHOTON_20 Required a calorimeter cluster with $E_T^{EM}/E_T^{TOT} > .889$, $E_T^{EM} > 20$ GeV

and fewer than 5 trigger towers in the cluster. The Level 1 Photon_2_7 trigger was required to have passed.

ELECTRON_12_6 Required a calorimeter cluster with $E_T^{EM}/E_T^{TOT} > 0.889$, a stiff track matched to the calorimeter cluster, cluster $E_T^{EM} > 12$ GeV, and P_T of the track > 5.5 GeV/c. It also required the centroid of the cluster in η to be in the central region of the CDF detector.

CENTRAL_MUON_13 Required the Level 1 Central_Muon_5 trigger to have passed and a gold muon with track P_T above 13 GeV/c where the efficiency was expected to have been 50%.

DIMUON_5_V2 Required the Level 1 Dimuon_2 trigger to have passed and a gold muon with track P_T above 4.8 GeV/c.

Once a Level 2 Accept had been generated by the Fred module, the Trigger Supervisor directed the different scanners in the DAQ system to begin readout of digital information into their buffers. This process is discussed in the next section along with the Level 3 component of the trigger system.

3.2.7 Data Acquisition at CDF

The CDF Data Acquisition (DAQ) system was designed to digitize the analog output from all subsystems and direct this data to tape. Figure 3.15 shows the different parts of the CDF DAQ system and their relationship to each other. Upon receiving an accept from the Level 2 part of the trigger system, the front end electronics were directed to digitize the analog signals. The digitized data was then read into data buffers for further processing. Additional processing and filtering was accomplished by the Level 3 part of the trigger system. Events passing Level 3 were then permanently recorded on tape.
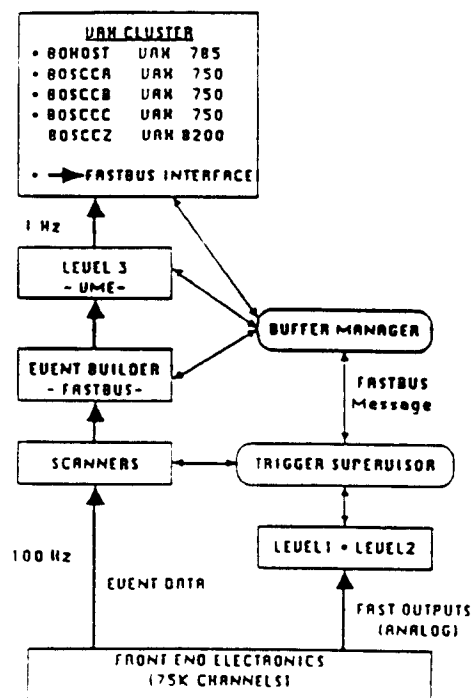
Figure 3.15: The CDF Data Acquisition system. The process of writing data to tape began with the acceptance of a Level 2 trigger. The Buffer Manager then directed the event through the Event Builder, Level 3 Trigger, and finally to tape.

Readout and Digitization of Detectors

The analog readout of each subsystem has already been discussed in Sections 3.2.2– 3.2.5. Once a Level 2 trigger was satisfied, the analog information from each subsystem was digitized and read into buffers which held the information for a given event. Depending on the particular subsystem, the digitization process was done either by FASTBUS or RABBIT modules.

The MAT cards were a typical example of modules which were incorporated within the RABBIT architecture on the front end. As discussed in Section 3.2.4, these modules performed charge-to-voltage and time-to-voltage conversions for the Central Muon Chambers. The front end crates also contained a number of other auxiliary and control modules. Examples of such modules include the BAT (Before-After-Timing) modules which provided timing signals and EWE (Event Write Encoder) modules which were responsible for digitizing the various signals provided by the subsystem modules. The EWE modules also provided the communication between a single RABBIT crate and the rest of the DAQ system.

The analog signals of the VTPC and CTC subsystems was provided by the ASD cards (see Sec. 3.2.1- 3.2.2). The output from the ASD cards, used by both the CTC and VTPC, was digitized by LeCroy 1879 TDC FASTBUS modules. Timing and control for the LeCroy TDC's was provided by other FASTBUS modules.

Once a Level 2 trigger accept was issued, the Trigger Supervisor module instructed the different types of scanners to begin reading the digital information into buffers. The digitized output from each type of front end was read into buffers by either MX scanners for RABBIT digitized components or by SSP scanners for the FASTBUS digitized components. Both types of scanners contained buffers which held the digital information.

Level 3 Filtering and Final Processing

The next step after scanning was to reformat the data and provide further filtering to reduce the accepted event rate to the 1-2 Hz level. The components of the DAQ system for these processes were the Event Builder and Level 3 trigger. These components were directed by a software process known as the Buffer Manager. Data read by the MX or SSP scanners was reformatted by the Event Builder and filtered by the Level 3 trigger. Events which passed the Level 3 trigger were then logged to tape or disk.

The Event Builder was a collection of modules which reformatted data from the different scanners into their final event record format. Reformatted data was then sent to the Level 3 trigger. The Level 3 trigger consisted of FORTRAN code which was run on custom designed microprocessors located in VME crates. The algorithms run in Level 3 were capable of filtering on more complicated quantities than elsewhere in the trigger system. The cuts and calculations used were similar to those in offline analyses. During the 1988-1989 Collider run, the Level 3 trigger reduced the event acceptance rate from approximately 10 Hz to 1-2 Hz.

The flow of data between the scanners, the Event Builder and Level 3 was directed by the Buffer Manager, a software package which ran on a dedicated computer. The Buffer Manager issued messages which initiated data processing and received messages signaling the completion of processing for each element in the DAQ pipeline. Figure 3.16 shows the time-ordered set of instructions issued to and from the Buffer Manager. On receiving information from the Trigger Supervisor that a new event was ready in the scanner buffers, the Buffer Manager directed the Event Builder to begin processing the new event. When the Event Builder completed its processing, the Buffer Manager then instructed it to push the event into the Level 3 processors. If an event passed the Level 3 trigger, the Buffer

Manager initiated the readout of the event to disk or magnetic tape by software processes referred to as 'consumers'. Data stored on disk was used to monitor the performance of the detector during data taking, while that on tape formed the raw data used in offline analysis.
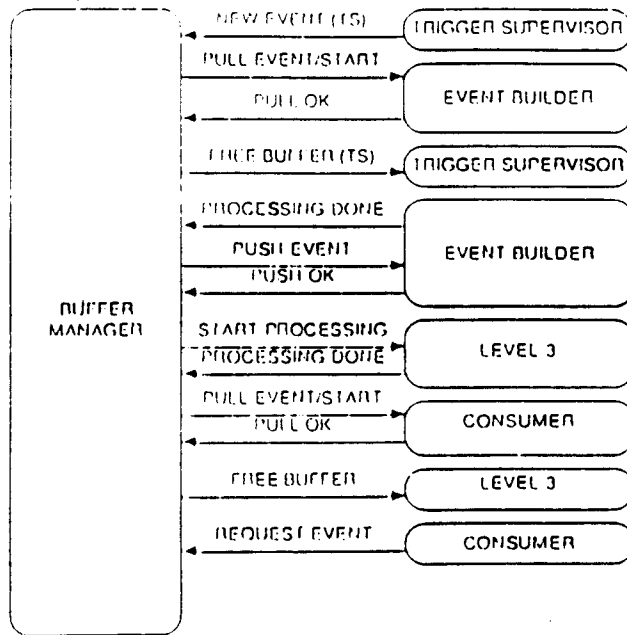
Figure 3.16: The order of messages between the Buffer Manager and the DAQ system. The messages listed here are time-ordered with time increasing from top to bottom.

Chapter 4

Analysis

This thesis reports the measurement of the b quark and B^0 meson cross sections in $\bar{p}p$ collisions at $\sqrt{S} = 1.8$ TeV for b quarks with $P_T > 10$ GeV and $|y| < 1.0$. The measurement was obtained from the number of B^0 mesons reconstructed in the decay chain:

$$B^0 \to J/\psi \; K^{0*},$$

$$K^{0*} \to K^+ \; \pi^-,$$

$$J/\psi \to \mu^+ \mu^-.$$

The cross section is related to the number of these decays observed, N_B, via

$$\sigma = \frac{N_B}{\mathcal{L} \times \epsilon \times \mathcal{B}}, \tag{4.1}$$

where $\mathcal{L}$ is the integrated luminosity, ϵ is the combined efficiency and acceptance, and $\mathcal{B}$ is the product of the branching fractions in the decay chain.

The decay $J/\psi \to \mu^+ \mu^-$ was a particularly useful signature since muon pairs are easily distinguished in a $\bar{p}p$ environment from the background of hadrons produced in the majority of $\bar{p}p$ collisions. The events used for this analysis were required to satisfy one of two dimuon

84

triggers used by CDF in the 1988-1989 Collider run. After identifying events with candidate J/ψ 's, all oppositely charged tracks were combined pairwise to form K^{0*} candidates. The K^{0*} candidates in each event were then combined with the J/ψ candidate to form candidate B^0's .

This chapter details the measurements of the efficiencies and acceptances, the details of B^0 identification, and the cross section result. Section 5.1 describes the measurement of the trigger efficiency. Section 5.2 describes the Monte Carlo and simulation of the CDF detector used to obtain the cuts needed to extract the B^0 signal, and the efficiency of these cuts. The Monte Carlo and detector simulation was also used to obtain the geometric acceptance for the observation of the B^0's . Finally, Section 5.3 describes the results obtained from the B^0 signal observed in the data.

4.1   Trigger Efficiencies

As was discussed in Chapter 3, the trigger system was designed to select events of interest in $\bar{p}p$ collisions. In order to have a well-known efficiency for selecting events of a particular type, it is desirable for an analysis to form a data set from those events which satisfied a particular trigger. Because the presence of a J/ψ meson decaying into two muons is required for the analysis presented in this thesis, events in the data sample must have satisfied a dimuon trigger.

Almost 3000 $J/\psi \rightarrow \mu^+\mu^-$ decays were reconstructed in 4.3 pb^{-1} taken in the 1988-1989 Collider run. About 2600 of these events satisfied a dimuon trigger. Most of the remaining J/ψ events were triggered by a single muon trigger whose nominal P$_T$ threshold of 9 GeV/c was chosen to optimize electroweak and top quark search analyses.

At Level 2 two dimuon triggers selected events to be written to tape. These were the

Dimuon_5_V2 and Dimuon_3_3 triggers. The respective luminosities recorded with these triggers were approximately 1.7 and 2.6 pb^{-1} and the triggers operated in nonoverlapping portions of the Collider run. Both dimuon triggers selected events with two muon candidates above a preset P_T threshold, but differed somewhat in how they were implemented. In order to present the efficiencies of these triggers, a more detailed knowledge about their specific requirements is necessary.

As described in Chapter 3, muon triggers were based on the identification of 2-dimensional tracks, or 'stubs', in the muon chambers, and stiff tracks found by the Central Fast Tracker (CFT). Stubs found by the trigger were also called 'brass muons', and stubs which matched a CFT track were called 'gold muons'.

The Level 1 muon triggers were based solely on the presence of brass muons. The drift time differences from each pair of sense wires in a chamber were calculated by the MAT modules. Based on these drift time differences, a pair of Muon Trigger (MTRG) modules on each wedge checked for the presence of stubs with P_T greater than a preset threshold. One of the MTRG modules identified single brass muons. The threshold for this module was set to either 3 or 5 GeV/c. The P_T threshold for the second MTRG module was set at 2 GeV/c. During a portion of the run, dimuons could be identified at Level 1 with stubs which passed the 2 GeV/c threshold. The presence of muons in each wedge with P_T above 2 GeV/c was sent to the DIMU module. If more than one wedge contained such a stub, the DIMU module signaled the presence of a muon pair.

During the 1988-1989 Collider run, three different muon triggers were implemented at Level 1. These were:

Central_Muon_5 : This trigger required at least one stub with P_T above 5 GeV/c.

Central_Muon_3 : This trigger required at least one stub with P_T above 3 GeV/c.

Dimuon_2: This trigger required the DIMU module to have identified a pair of wedges containing stubs with P_T above 2 GeV/c.

Note that the 2 GeV threshold was only utilized as part of the Level 1 Dimuon_2 trigger. For the sake of maintaining a consistent terminology, the application of the 2 GeV threshold to single muons will be referred to as the Level 1 Central_Muon_2 trigger. The Dimuon_2 trigger is then logically equivalent to requiring two muons in different wedges to have each satisfied the Level 1 Central_Muon_2 trigger.

At Level 2, the MU2T (Level 2 Muon trigger) Fastbus modules identified gold muons by matching stubs with CFT tracks. There was one MU2T module for each wedge (merging both the North and South sides of CDF) for a total of 24 which were collectively referred to as the Muon Matchbox. For each brass muon, the Matchbox determined if there was a CFT track which matched the stub in R-ϕ after extrapolation of the CFT track through the calorimetry and solenoid. The extrapolation included the effects of the magnetic field in the solenoid. To satisfy the matching, the CFT track was required to extrapolate to the same muon chamber as the stub or to an adjacent chamber. In this way, the maximum difference between a matched CFT track and stub was 10.8° (see fig 3.10).

The Level 2 decision could be based on the P_T of the CFT tracks associated with gold muons, the number of gold muons in an event, and any Level 1 data. With this information, three Level 2 muon triggers were formed for the 1988-1989 Collider run. These were

Dimuon_5_V1 This trigger required the Level 1 Dimuon_2 trigger and the presence of a gold muon with $P_T > 6.0$ GeV/c. The luminosity recorded with this trigger was 0.05 pb^{-1} .

Dimuon_5_V2 This trigger required the Level 1 Dimuon_2 trigger and the presence of a gold muon with $P_T > 4.8$ GeV/c. The luminosity recorded with this trigger was 1.65

pb^{-1} .

Dimuon_Central_3 This trigger required two gold muon clusters with $P_T > 3.0$ GeV/c

The luminosity recorded with this trigger was 2.61 pb^{-1} .

The requirement of two *clusters* in the Dimuon_3_3 trigger implied requirements on the

spatial separation of the two gold muons. As discussed in Section 3.2.6, the Level 2 trigger

decision was based on information sent to the Level 2 processors. Gold muons were identified

to these processors as clusters-meaning that adjacent wedges containing gold muons were

merged to form one gold muon cluster. For the Level 2 muon triggers, this meant that to

be counted as two clusters by the processor, the muons would have to be separated by at

least one wedge in phi when on the same end (East or West) of the detector. When the

muons were on separate ends, they could not be in the same wedge, but could be in adjacent

wedges.

The Dimuon_5_V2 triggers did not have the same wedge separation requirement. The

decision as to whether the event had two muon candidates was made by the DIMU module

which looked for stubs in any two wedges. Since, however, the identification of stubs was

made on a wedge by wedge basis, muon pairs were required to be in different wedges.

Information from both ends of the detector was merged, so this requirement was independent

of whether or not the muons were on the same side of the detector.

In this analysis, events were required to satisfy either the Dimuon_3_3 or Dimuon_5_V2

triggers. The efficiency of the Dimuon_3_3 trigger was measured by obtaining the efficiencies

of the CFT 3 GeV/c threshold and the Level 1 Central_Muon_3 trigger. The total efficiency

was then taken to be the product of these two requirements for each muon of a pair.

The efficiency of the Dimuon_5_V2 trigger was obtained by measuring the efficiency

of the CFT 5 GeV/c threshold, the Level 1 Central_Muon_5 trigger, and the Level 1 Cen-

tral_Muon_2 trigger. The total efficiency for a pair of muons to pass the Dimuon_5_V2 trigger was derived from these component efficiencies by dividing muon pairs into stiff muons and soft muons. For each muon pair, the stiff muon was required to be a 5 GeV/c gold muon while the soft muon was required to pass the Level 1 Central_Muon_2 trigger. The combined efficiency was therefore the product of the CFT 5 GeV/c and Level 1 Central_Muon_5 efficiencies, evaluated for the P_T of the stiff muon, and the Level 1 Central_Muon_2 efficiency, evaluated for the P_T of the soft muon. The measurements of the individual thresholds for both the Dimuon_5_V2 and Dimuon_3_3 triggers are detailed below.

4.1.1   Level 2 Dimuon_5_V2 Trigger Efficiency

As discussed in Section 4.1, the measurements of the Dimuon_5_V2 and Dimuon_3_3 trigger efficiencies required the efficiencies for the Level 1 muon triggers and the CFT. The efficiency of each Level 1 muon trigger was measured by first isolating a sample of muons which was unbiased by the triggers themselves. The muon sample was divided into intervals, or bins, of P_T . For each P_T bin, the number of muons which actually caused the trigger to fire, divided by the total number of muons in the P_T bin, was taken as the trigger efficiency.

The CFT efficiencies were found by obtaining a set of events unbiased by tracking requirements in the triggers and determining if a track found by the offline reconstruction was associated with a CFT track. The measurements required for the Dimuon_5_V2 and Dimuon_3_3 trigger efficiencies (Central_Muon_5 and Central_Muon_2 triggers, and the CFT 5 GeV efficiency) are discussed in the following two sections.

Measurement of the Level 1 Central_Muon_5 Trigger Efficiency

The measurement of the Central_Muon_5 trigger efficiency was based on two samples of muons. One sample was obtained from cosmic rays and another was obtained from p̄p data.

Cosmic ray data for studies of trigger efficiencies were taken in special runs with the CDF detector. Muons from cosmic rays were obtained by triggering on tracks found by the CFT with a nominal P_T threshold of 3.0 GeV/c. The muon trigger information was recorded, but did not form part of the cosmic ray trigger. Approximately 3000 muons were reconstructed offline with the 5 GeV/c muon trigger threshold. The P_T distribution of the trigger efficiency for the 5 GeV/c threshold obtained from these muons is shown in Figure 4.1.

The efficiency of the Level 1 Central_Muon_5 trigger was also measured with muons found in $\bar{p}p$ interactions. This method complemented the cosmic ray measurement in that the P_T distribution of the muons from $\bar{p}p$ data was dominated by muons with P_T's below about 10 GeV/c, whereas most of the muons in the cosmic ray data had P_T's above 5 GeV/c.

Events which contained at least one muon candidate were selected with the requirement that a trigger which did not incorporate either tracking or muon information was satisfied. Examples of such triggers included photon and jet triggers, both of which employed calorimetry information only. By looking at the event record it was possible to determine if a wedge with a muon candidate satisfied the Level 1 Central_Muon_5 trigger. If a wedge contained two or more muon stubs, it was not possible to determine which one did or did not pass the trigger. To remove the ambiguity, only muon candidates with one stub in a wedge were considered. For J/ψ events, both muons were contained within the same wedge approximately 5% of the time.

Selecting events with at least one muon candidate produced a data set which contained a mixture of real and fake muons. Sources of fake muons included interacting and noninteracting 'punch-through'. Punch-through occurred when hadrons from an event were not stopped by the calorimeter. If the punch-through was accompanied by a hadronic shower
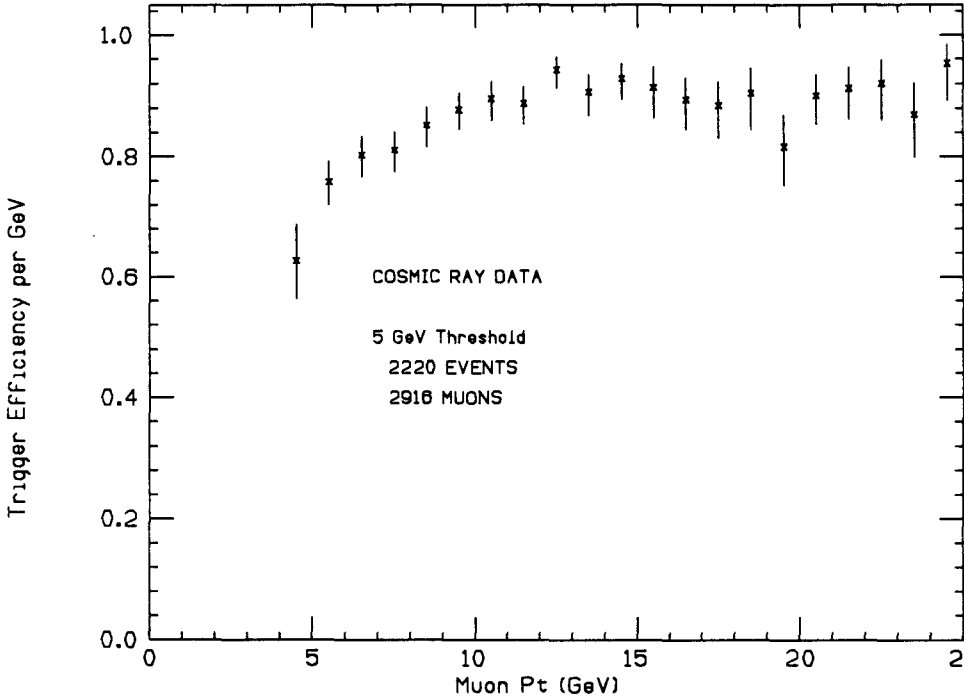
Figure 4.1: Efficiency of the Central_Muon_5 trigger obtained using cosmic rays .

in the calorimetry, it was called interacting. Noninteracting punch-through occurred when a hadron passed through the calorimetry without showering. Muons from decays of K and π mesons also contributed to the background. Fake muons from decays and interacting punch-through will lower the trigger efficiency while noninteracting punch-through should behave very similarly to real muons.

To remove the background from interacting punch-through, a cut was placed on the energy deposited in the calorimeter towers traversed by the muon. The energy cuts were obtained by examining the energy distributions from muons in J/ψ events. Muon pairs in the J/ψ mass region are approximately 90% real J/ψ 's based on fitting the peak in Figure 4.2 to a linear background plus a Gaussian signal. The reconstructed J/ψ sample shown in Figure 4.2 was arrived at by combining all oppositely signed muon pairs in the 1.7 pb^{-1} for which the Dimuon_5_V2 trigger was operated. The muons in the J/ψ sample employed here were beam constrained rather than vertex constrained as was done for the J/ψ sample utilized to identify B^0 mesons. A fit to the beam constrained J/ψ sample had a width of approximately 18 MeV/c^2 and a mean of 3.0965 ± 0.0007 GeV/c^2 [40], in good agreement with the world average mass value of 3.09693 ± 0.00009 GeV/c^2 [51]. Figure 4.3 shows the energy deposited in the electromagnetic and hadronic calorimetry for muons in J/ψ events and for muon candidates selected for the efficiency measurement. Using the energy distributions of the J/ψ muons, the following cuts were made:

$$3.5 > E_{HAD} > 0.2 \text{ GeV} \tag{4.2}$$

$$1.0 > E_{EM} > 0.05 \text{ GeV,} \tag{4.3}$$

where E_{EM} and E_{HAD} are the energy deposited in the electromagnetic and hadronic calorimeter towers respectively.

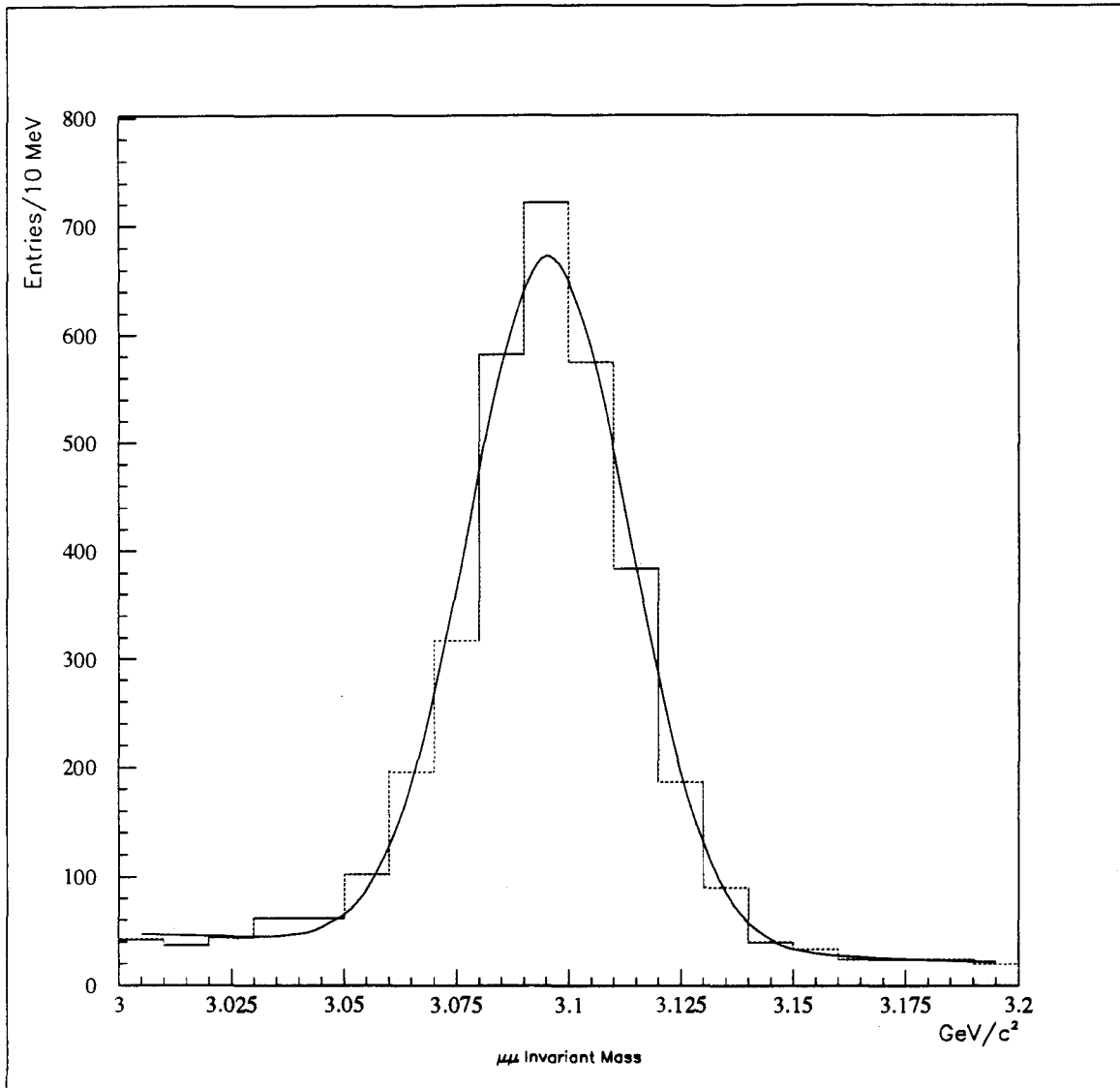Figure 4.2: Dimuon invariant mass distribution in the region near the J/ψ resonance. The matching cuts of Equations 4.4 and 4.5 were included. A fit to a Gaussian and a linear background indicates that dimuons in this region are approximately 90% pure J/ψ 's.
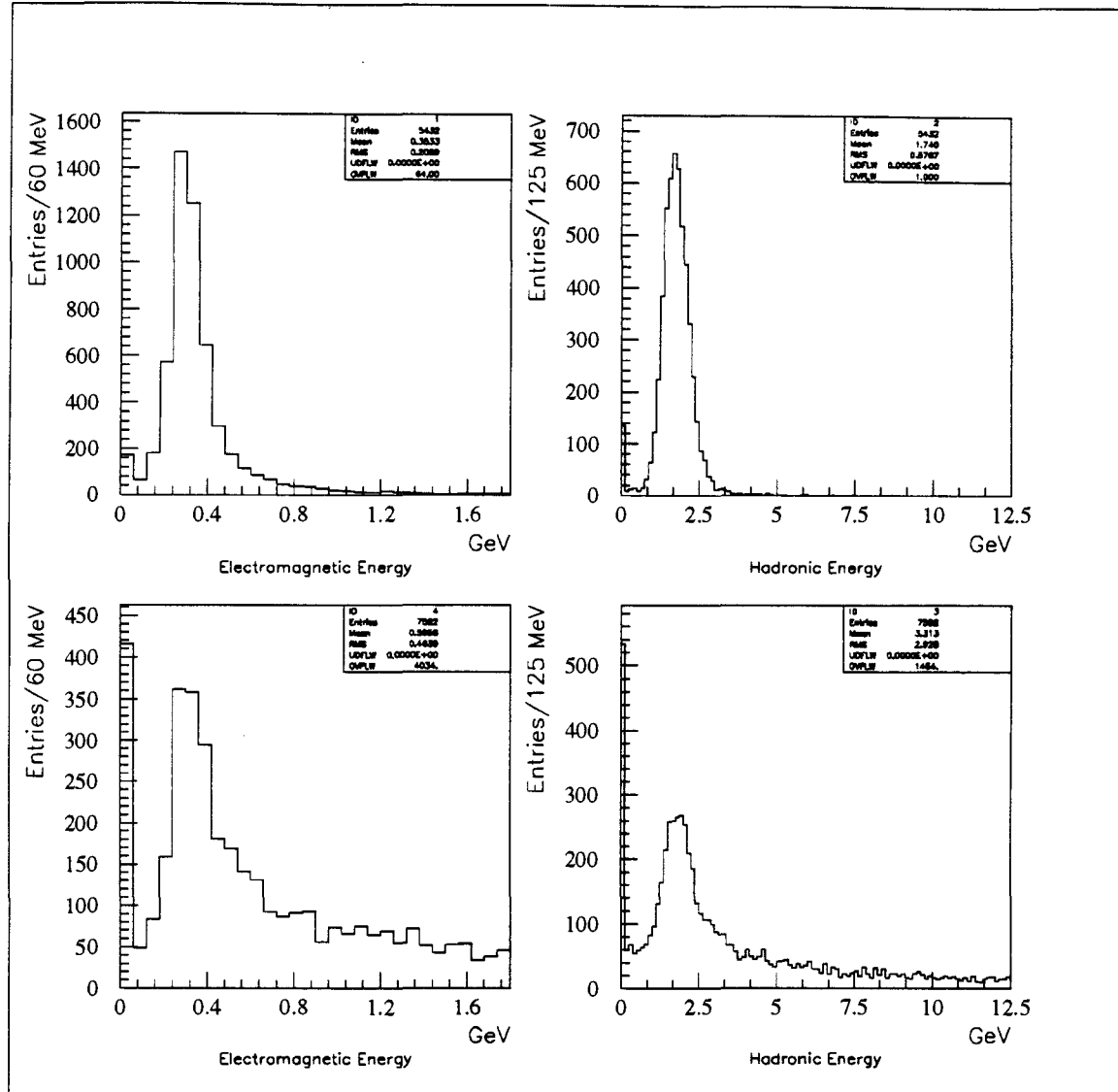
Figure 4.3: Energy deposited in calorimeter towers for muons in J/ψ sample (top) and muon candidates used in the trigger efficiency study (bottom).

Additional background was removed by requiring a good quality CTC track associated with a prompt vertex (see Appendix B) and imposing cuts on the match between the CTC track and the muon stub. The matching cuts are described in Appendix A, and involved scaling the track-stub mismatch by that expected due to Multiple Coulomb Scattering (MCS). The cuts were:

$$|\Delta I_{XY}| < 3 \, \sigma_{MCS}, \tag{4.4}$$

$$|\Delta I_{ZY}| < 3 \, \sigma_{MCS}, \tag{4.5}$$

where ΔI_{XY} and ΔI_{ZY} are the differences between the stub and track at the inner radius of the muon chamber in a plane parallel to the chamber wires, and σ_{MCS} is the standard deviation of the expected mismatch due to Multiple Coulomb Scattering.

The above cuts did not remove all the punchthrough and decay-in-flight background. Figure 4.4 shows the distribution of ΔI_{ZY} for the candidate events, with the cuts of Equations 4.2 - 4.4 applied, and the same distribution for muons from the J/ψ sample. The non-J/ψ muon candidates (Fig. 4.4 (b)) show a broader distribution reflecting some remaining background. Rather than trying to remove this background with further cuts, an estimate of the fraction of the data sample which was background was made on the basis of the zy matching distributions for each P_T bin.

Real muons were assumed to have the same matching distribution as that obtained from the J/ψ sample. The matching distribution characterizing non-muon candidates was obtained by fitting the matching distribution of the trigger study sample, shown in Figure 4.4(b), to the sum of two Gaussians. The first Gaussian was constrained to have the same width as the matching distribution from muons in the J/ψ sample. The mean of the second Gaussian was fixed to zero and the total area contained within the two Gaussians was constrained to be the total number of candidate muons. Note that the distribution shown

in Figure 4.4(b) included the cuts of Equations 4.2 - 4.5. The fitted width of the second Gaussian was then assumed to characterize the background in the muon data sample.

The number of real and fake muons in each P_T bin was estimated from these two Gaussians for two subsets of the trigger study sample. The set of muons candidates which passed the trigger comprised Set A and the set of all muon candidates formed Set B. The respective numbers of real muons in these sets were designated Sets A' and B'. For a given P_T , the efficiency was calculated as the ratio A'/B'. Figures 4.5 and 4.6 show the ΔI_{ZY} matching distributions from which the estimate of the background fraction in each P_T bin was made. For each P_T interval, the muon candidates in Sets A and B were fit to the background and signal Gaussians discussed above, allowing only the number of events in each Gaussian to vary, but constraining the sum of the two to be the total number of candidates in the specific P_T bin. The Gaussians were then integrated from $+3\ \sigma$ to $-3\ \sigma$ to estimate the number events which satisfied Equation 4.5.

Figure 4.7 shows the resulting efficiency $\epsilon_5(P_T) = A'/B'$ combined with the efficiency found from the cosmic ray data. Table 4.1.1 shows the number of muons before and after the background subtraction for all candidates and for those which passed the trigger. Because the number of real plus fake muons was constrained to equal the total number of candidates, the uncertainty in the number of background events is not shown. The uncertainty in the efficiency for each P_T bin was calculated assuming the trigger to be described by a binomial process. Additionally, there was assumed to be an error in the number of muons in each P_T bin due to the background subtraction. The P_T distribution of the efficiency was fit to a formula based on Multiple Coulomb Scattering. The best fit is also included in Figure 4.7 and indicated an asymptotic efficiency of $95 \pm 3\%$.
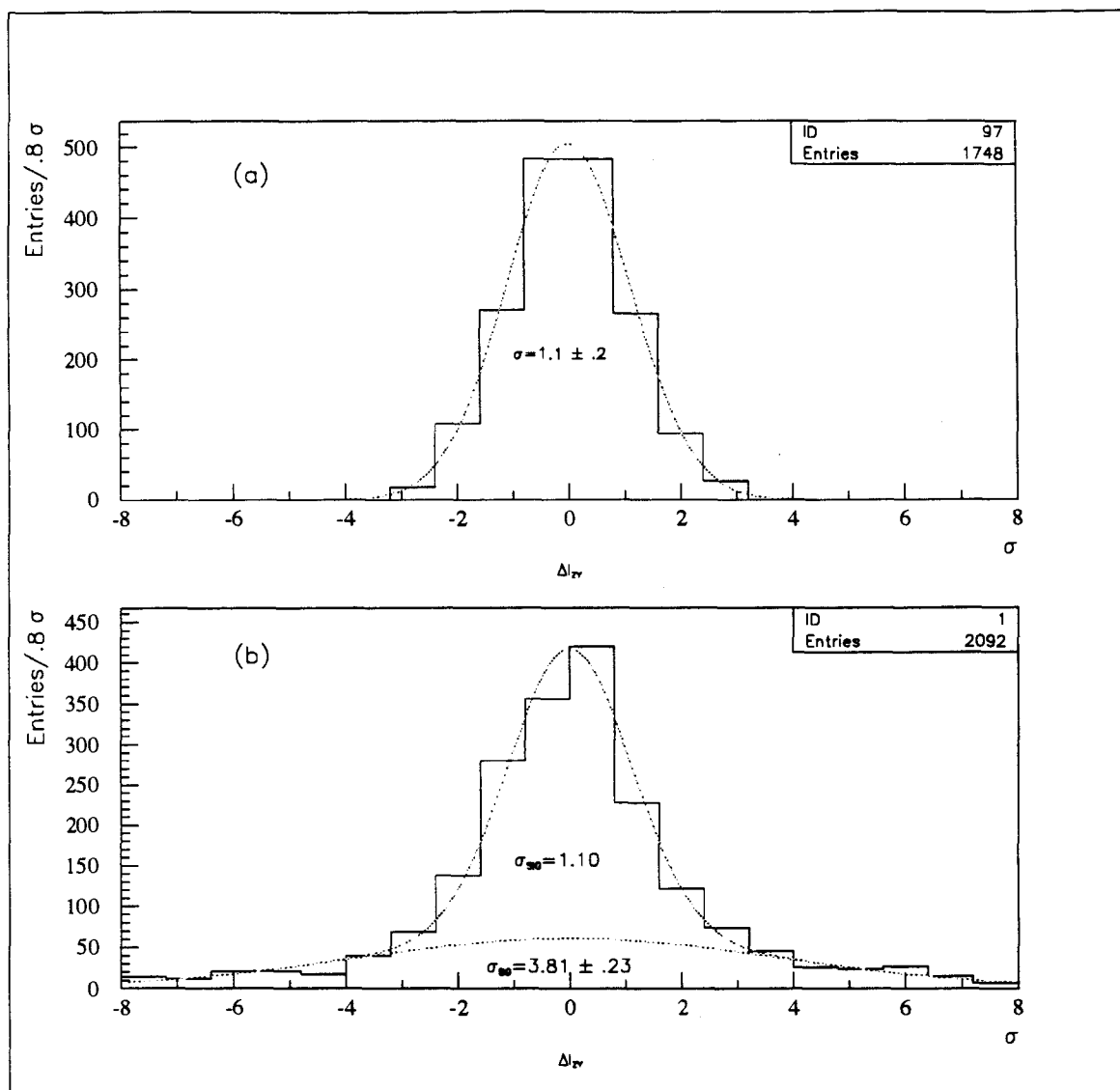
Figure 4.4: ΔI_{ZY} matching distribution for (a) J/ψ muons and (b) for all muons from which the Central_Muon_5 trigger efficiency was obtained. The distribution in (b) was fit to the sum of two Gaussians. The parameters of the first Gaussian were fixed based upon the same distribution from J/ψ muons. The second Gaussian was assumed to characterize the distribution from the background of fake muons.
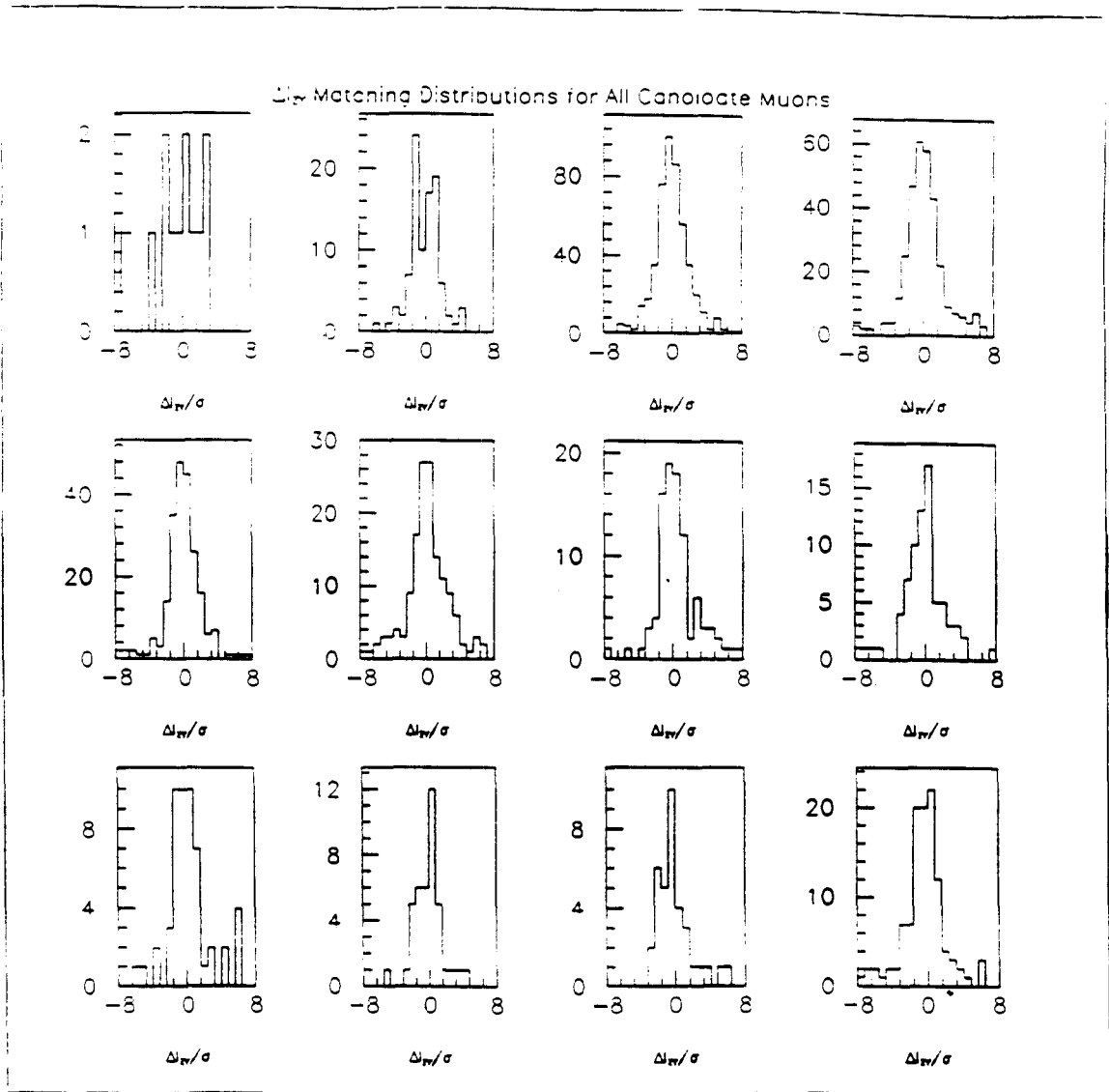
Figure 4.5: ΔI_{ZY} Matching Distributions for the different P_T bins examined in the Central_Muon_5 trigger efficiency study. The distributions contain contributions for all the muon candidates in the study.
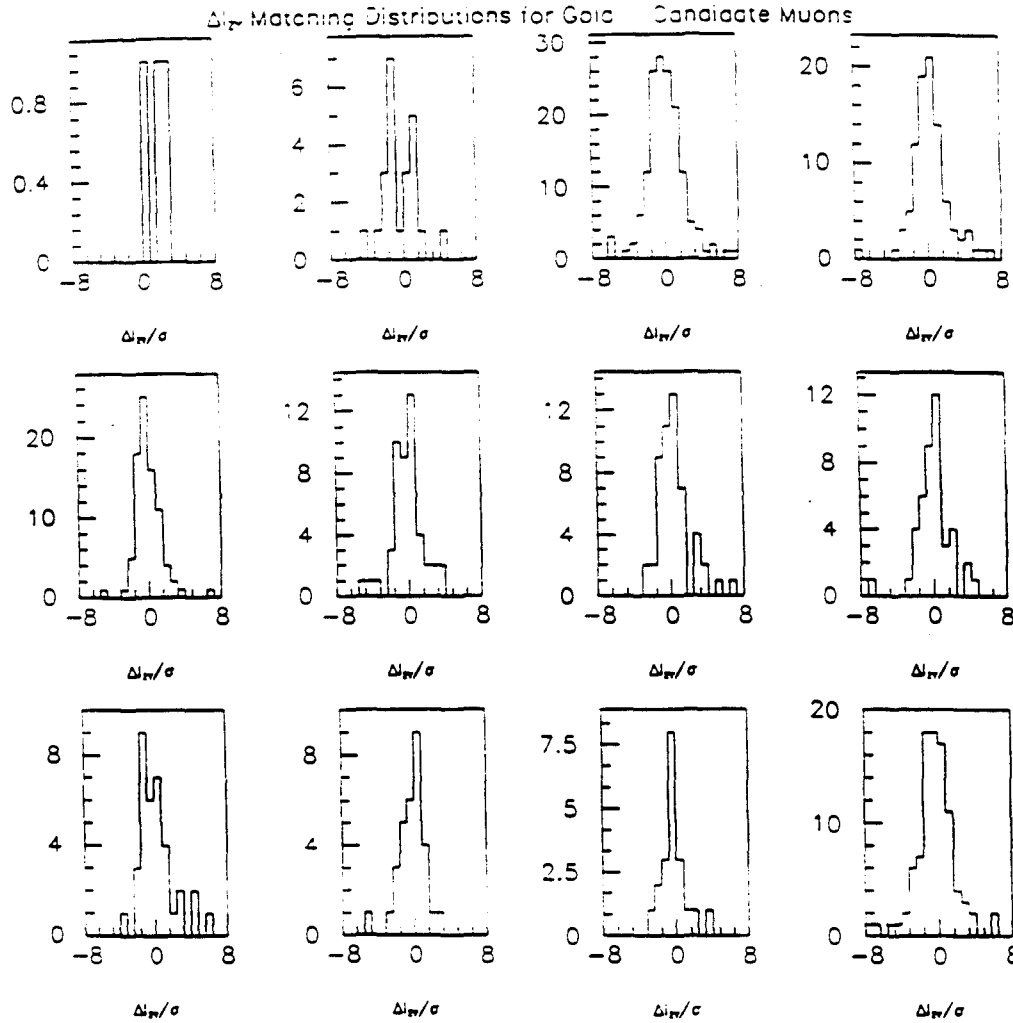
Figure 4.6: ΔI_{xy} Matching Distributions for candidates which satisfied the Central_Muon_5 trigger (Set A).
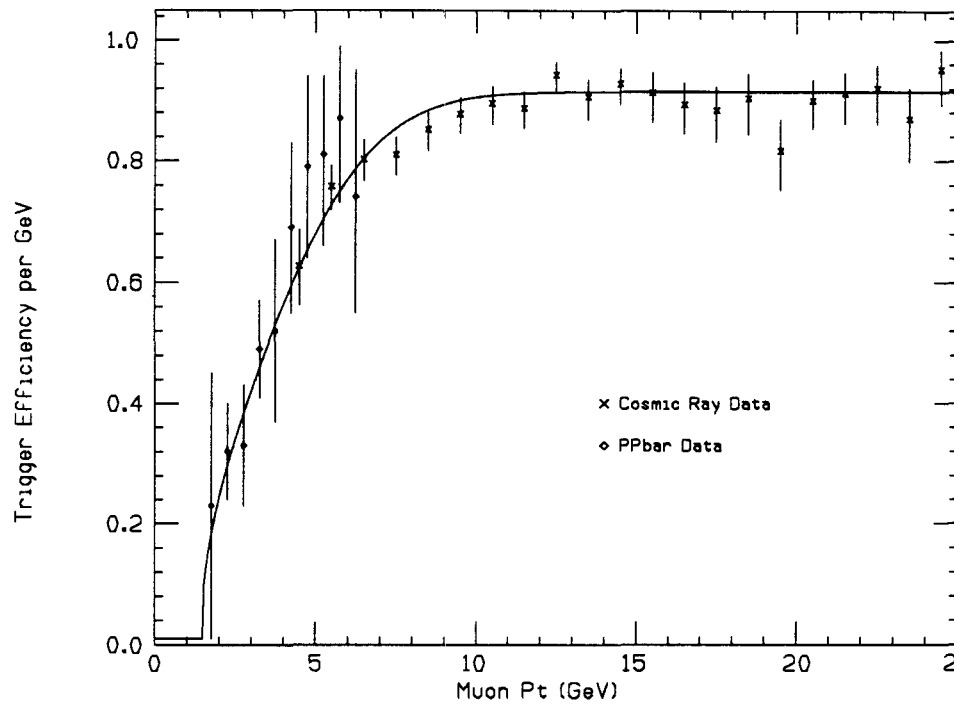
Figure 4.7: Measured efficiency of the Level 1 Central_Muon_5 trigger. The curve is a best fit to a function based on Multiple Coulomb Scattering.

P_T (GeV/c)	All Candidates (Set B)		Candidates Passing Trigger (Set A)		
	Set B'	N_{BG}	Set A'	N_{BG}	ϵ
0.0-1.5	17.4 ± 2.7	1.4	.9 ± 1.8	1.2	.052
1.5-2.0	70.9 ± 7.4	14.0	16.3 ± 3.9	3.8	.23 ± .22
2.0-2.5	318.3 ± 17.4	88.5	102.4 ± 9.4	27.2	.322 ± .078
2.5-3.0	198.9 ± 14.4	67.6	65.3 ± 6.7	15.5	.328 ± .094
3.0-3.5	156.4 ± 10.6	33.9	77.1 ± 4.3	4.2	.493 ± .069
3.5-4.0	70.1 ± 9.0	42.3	36.2 ± 4.8	6.6	.519 ± .127
4.0-4.5	56.1 ± 7.8	21.3	38.6 ± 5.1	7.5	.688 ± .115
4.5-5.0	42.3 ± 7.1	17.8	33.2 ± 4.4	5.5	.785 ± .135
5.0-5.5	31.2 ± 5.6	12.3	25.2 ± 4.5	6.1	.808 ± .112
5.5-6.0	31.4 ± 4.4	4.8	27.4 ± 3.1	2.1	.866 ± .101
6.0-6.5	23.6 ± 4.9	6.4	17.4 ± 2.7	1.4	.737 ± .178
>6.5	65.6 ± 8.2	25.6	61.4 ± 7.7	18.3	.936 ± .039

Table 4.1: Muon and background candidates from which the trigger efficiency was determined with $\bar{p}p$ collision data. Sets A' and B' are the background subtracted number of muons passing the trigger and the total number, respectively. N_{BG} refers to the number of background candidates estimated in each P_T bin.

Measurement of the Level 1 Central_Muon_2 Trigger Efficiency

The estimation of the Central_Muon_2 trigger efficiency was made with two methods. The first method obtained the efficiency for muons with $P_T > 5$ GeV/c from cosmic rays, as was done for the Central_Muon_5 trigger. The second method measured the efficiency at lower P_T with Monte Carlo data based on measurements of the J/ψ production cross section with the Dimuon_3_3 trigger. In principle, a direct measurement of the low P_T efficiency from $\bar{p}p$ data was possible. However, complications related to the design and implementation of the trigger prevented a direct measurement of the efficiency at low P_T with $\bar{p}p$ data.

The first complication in the measurement of the Central_Muon_2 efficiency was that no direct information was kept as to whether an event satisfied the Level 1 Dimuon_2 trigger. The Level 1 Dimuon_2 trigger was the only format in which the 2 GeV/c threshold was utilized, and the only recorded information for each event was whether the Level 2 Dimuon_5_2 trigger was satisfied, whether the Level 1 Central_Muon_5 trigger was satisfied, and/or whether there were any 5 GeV/c gold muons in each wedge. This complication was circumvented by requiring at least one gold muon in a muon pair. If the muon pair passed the Dimuon_5_V2 trigger, then the Central_Muon_2 trigger must have been satisfied.

The second complication with the measurement of the Level 1 Central_Muon_2 efficiency was that no information was provided as to *which* two wedges had the muons. This presented a problem for measuring the efficiency because if a reconstructed dimuon pair failed the trigger, there was no way of knowing which particular muon, or both, failed. As with the first complication, this problem was solved by considering only muon pairs where one or both muons were known to have been gold. Knowing which muons were gold , combined with knowing whether the Dimuon_5_V2 trigger passed, provided an effective 'label' for which muons passed the Central_Muon_2 trigger.

These complications made it unfeasible, however, to measure the Level 1 Central_Muon_2 trigger efficiency with the same methods employed to estimate the Central_Muon_5 trigger efficiency. To do so, an unbiased set of muon pairs where one of the muons was gold would have been required. There were approximately 200 such events in the 1988-1989 data, which was not enough to make a sufficiently precise measurement of the Central_Muon_2 trigger efficiency. Instead, the efficiency was derived from a simulated muon sample obtained with the measured J/ψ differential cross section $\frac{d\sigma}{dP_T \times B(J/\psi \to \mu\mu)}$ (see Figure 4.8). The J/ψ differential cross section was measured using only the Level 2 Dimuon_3_3 trigger [40]. The P_T distribution of muons from the J/ψ 's passing the Central_Muon_5 trigger was obtained by simulating the decays of the J/ψ 's into muon pairs, and imposing the measured efficiencies of the Central_Muon_5 trigger and CFT 5 GeV/c threshold as a function of P_T . The P_T distribution of the non-gold muons in these simulated events formed the 'denominator' for the Central_Muon_2 efficiency. The 'numerator' was just the number of J/ψ 's observed in the data which passed the Dimuon_5_V2 trigger. Figure 4.8 shows the J/ψ differential cross section obtained from the J/ψ 's which passed the Dimuon_3_3 trigger.

The simulated and real J/ψ 's used for this measurement were required to have passed the same cuts as those in Reference [40]. The cuts were

- $|\eta_{J/\psi}| < 0.5$

- 6 GeV/c $< P_T <$ 14 GeV/c

- Both muons were required to satisfy the matching cuts of Equations 4.4 and 4.5.

Additionally, the stiff leg of both simulated and real J/ψ 's was required to have been identified as gold muons passing the 5 GeV/c threshold. Furthermore, the P_T of the stiff leg was required to be larger than 5 GeV/c. A number of other cuts and effects in the real data were corrected for in the simulated data. The J/ψ candidates in $\bar{p}p$ data were required
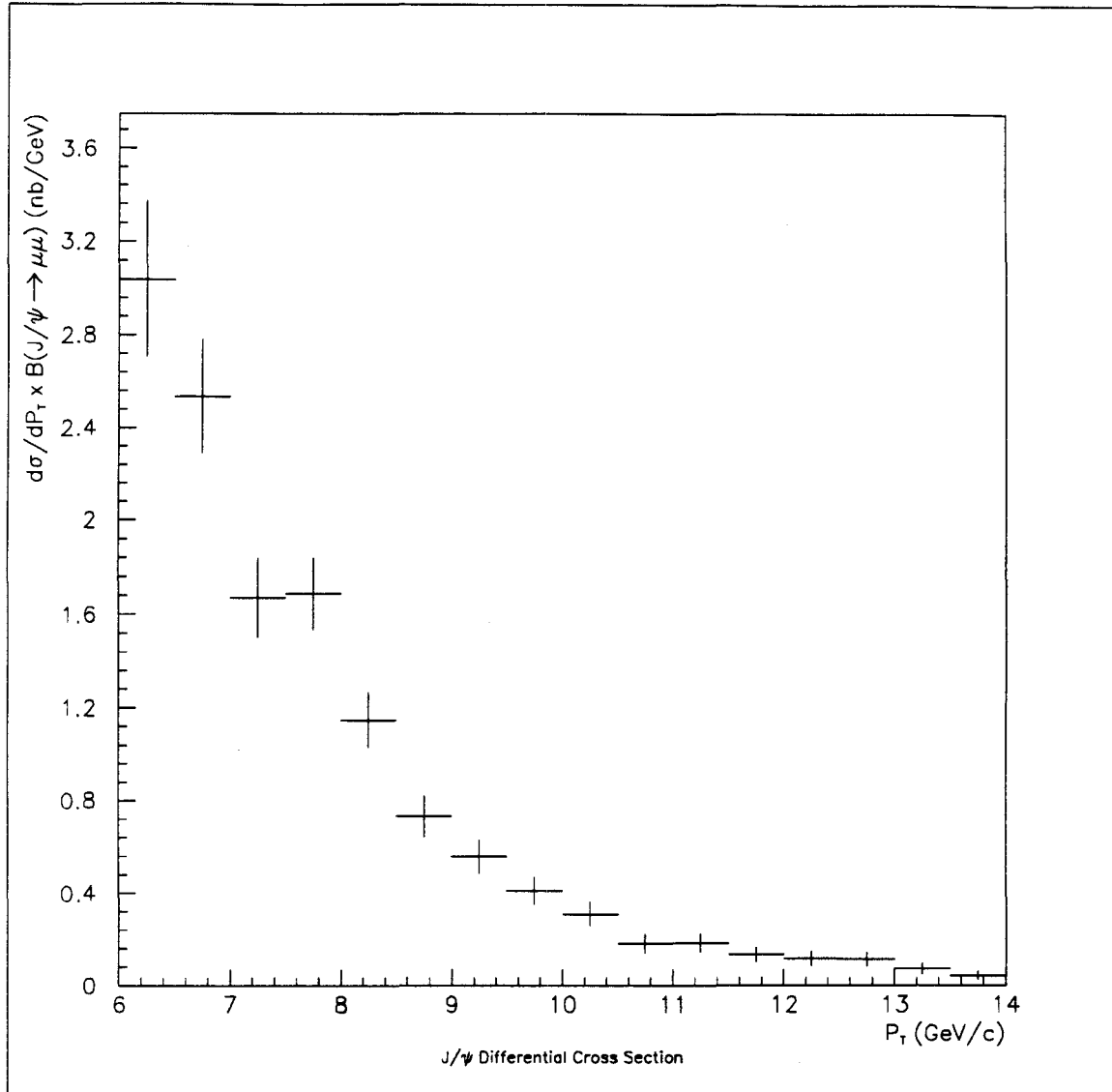
Figure 4.8: Measured differential cross section for the production of J/ψ at CDF. The cross section was obtained using J/ψ 's which satisfied the Dimuon_3_3 trigger.

to have an invariant $\mu\mu$ mass within approximately 1.83 σ of the fitted J/ψ mass, where σ was the fitted width of the vertex constrained J/ψ mass in the data (approximately 23 MeV/c^2). The efficiency of this cut was determined from the data to be 0.932 and was imposed as a multiplying factor in the number of reconstructed simulated J/ψ 's.

Another effect in the $\bar{p}p$ data was an inefficiency due to hardware problems in the Dimuon_5_V2 trigger. These losses are discussed more fully below. The loss of data implied an equivalent luminosity loss of approximately 14%. This was included as an inefficiency in the number of J/ψ 's reconstructed in the simulated data.

Background in the P$_T$ distribution of the soft legs from J/ψ 's in the data was subtracted using the J/ψ mass distribution for each P$_T$ bin. The mass distributions were fit to a Gaussian plus a flat background. The ratio of the soft muon P$_T$ distributions in real and simulated data formed the estimate of the Level 1 Central_Muon_2 trigger efficiency. Figure 4.9 shows the 2 GeV/c efficiency result obtained, combined with the efficiency from cosmic ray data.

The systematic errors in Figure 4.9 arise from several sources. These include the uncertainty in the J/ψ differential cross section, in the parameterization of the CFT and Level 1 Central_Muon_5 requirements, and in the estimation of the hardware losses at the beginning of the run. Also included in the systematic errors were the effects of the stub multiplicity in the wedges and the number of wedges with muon candidates. The simulated events did not reflect the latter two effects. Events in the data where there were three muons or where there were more than one stub in a wedge led to an overestimate of the efficiency. The different measured values of the efficiency were corrected downward to reflect this effect. The correction was estimated to be 3 ± 3 %. The systematic errors were added in quadrature with the statistical errors for each P$_T$ bin.
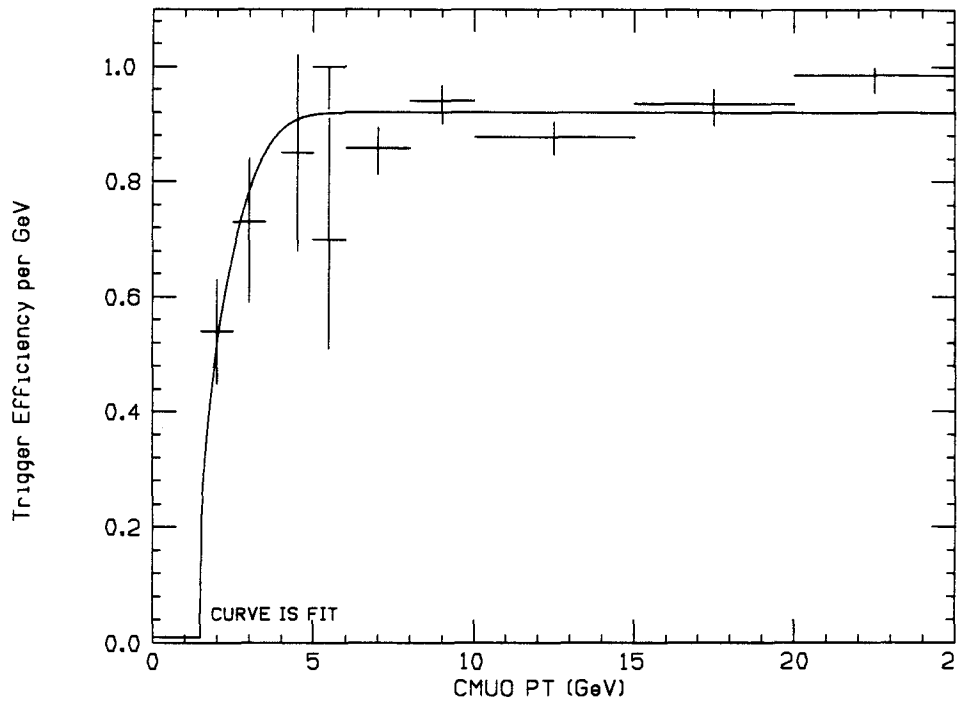
Figure 4.9: Efficiency of 2 GeV/c Threshold Level 1 Trigger using both methods described in the text.

Efficiency of the 5 GeV/c CFT requirement

The CFT efficiency was complicated by the fact that there was not a guaranteed correspondence between tracks found in the offline code and the CFT's themselves. In principle it was possible for several tracks to share the same hit on a wire. Additionally, the particle track which was responsible for the firing of the CFT did not have to include the hits associated with the CFT track in the determination of the CTC track parameters. As an approximation to the CFT efficiency, an offline search was made for CTC tracks which were isolated within events which were unbiased by triggers utilizing the CFT. Figure 4.10 shows the angle between the nearest wire with a prompt hit and the extrapolated phi position of the reconstructed track in superlayer 8. Tracks whose fits did not include hits from superlayer 8 were excluded from consideration. Tracks which had no nearby prompt hit were assigned an angular difference of exactly zero. This can be seen as the spike in Figure 4.10. A track was considered to have been found by the CFT if the angular difference at superlayer 8 was less than 16 mradians. The ratio between those events having a prompt hit and those without one determined the P_T distribution of the CFT efficiency. Figure 4.11 shows the resulting P_T distribution of CFT efficiency for the 5 GeV/c threshold. Below the nominal threshold, the efficiency falls rapidly. At low values of P_T (less than 3-4 GeV/c), the non-zero efficiency was not understood. A cut of $P_T > 5$ GeV/c for gold muons was made for the remainder of the analysis to avoid this region. Above 5 GeV/c, the efficiency was measured to be 0.96 ± 0.01.

The efficiency of the 3 GeV/c CFT threshold was measured in the same way and is shown in Figure 4.12
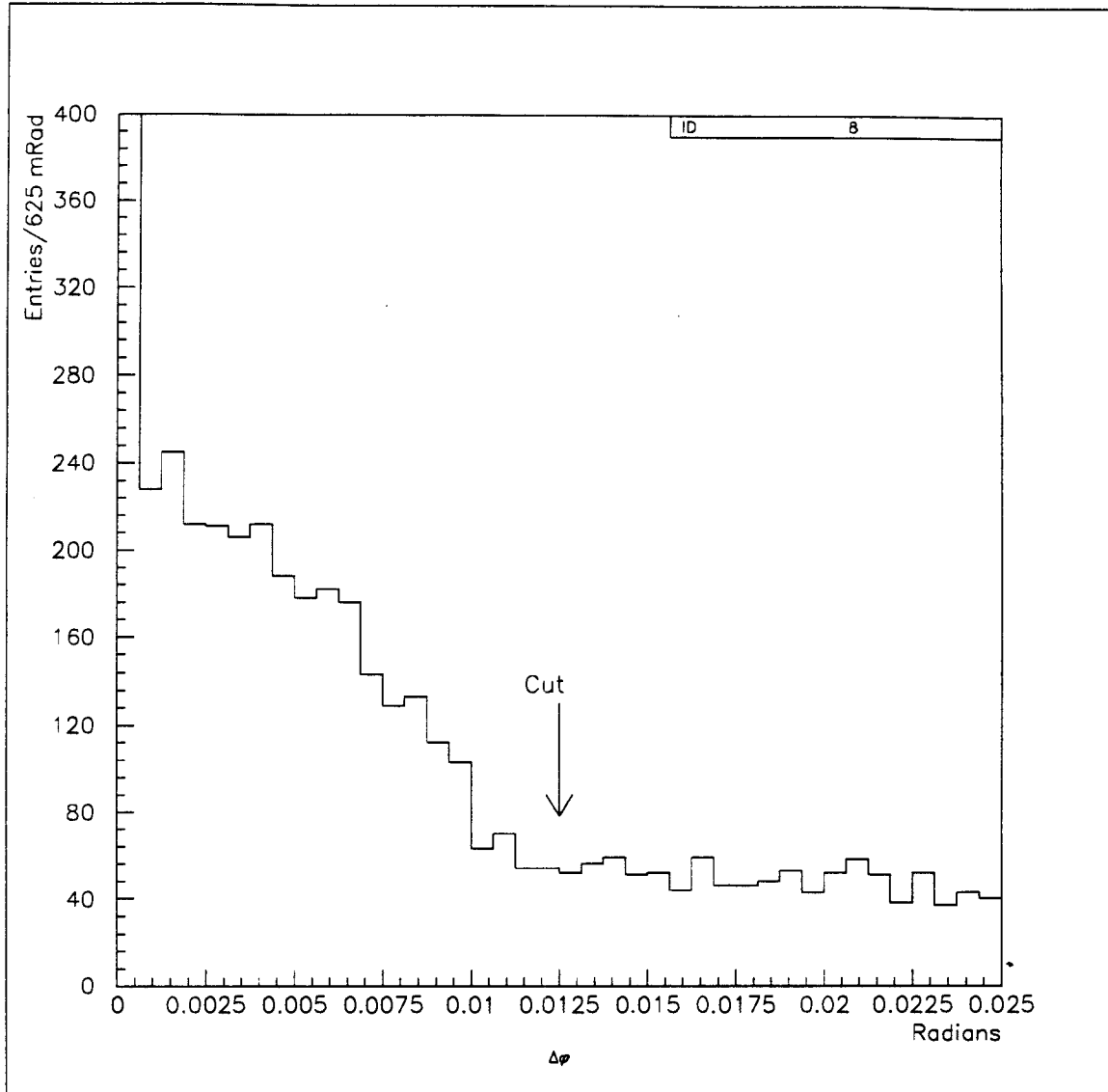
Figure 4.10: Angular separation between reconstructed tracks in the CTC and prompt hits from CFT tracks. The angular difference was taken between a radial line coinciding with the track position at the radius of the largest radius sense wire included in the track fit and the position of a prompt hit from any CFT track.
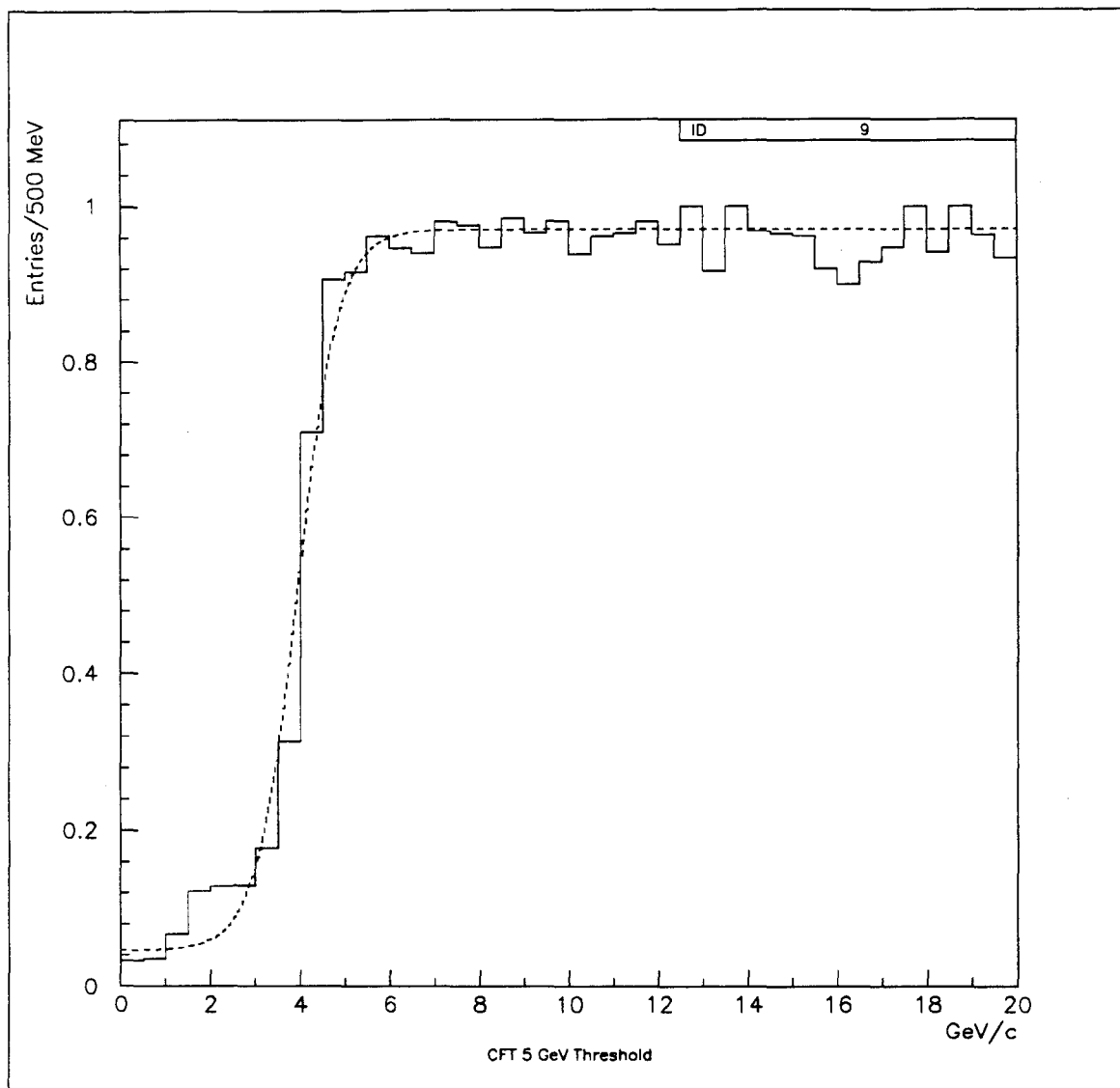
Figure 4.11: Efficiency of the CFT trackfinder with the nominal 5 GeV/c threshold.
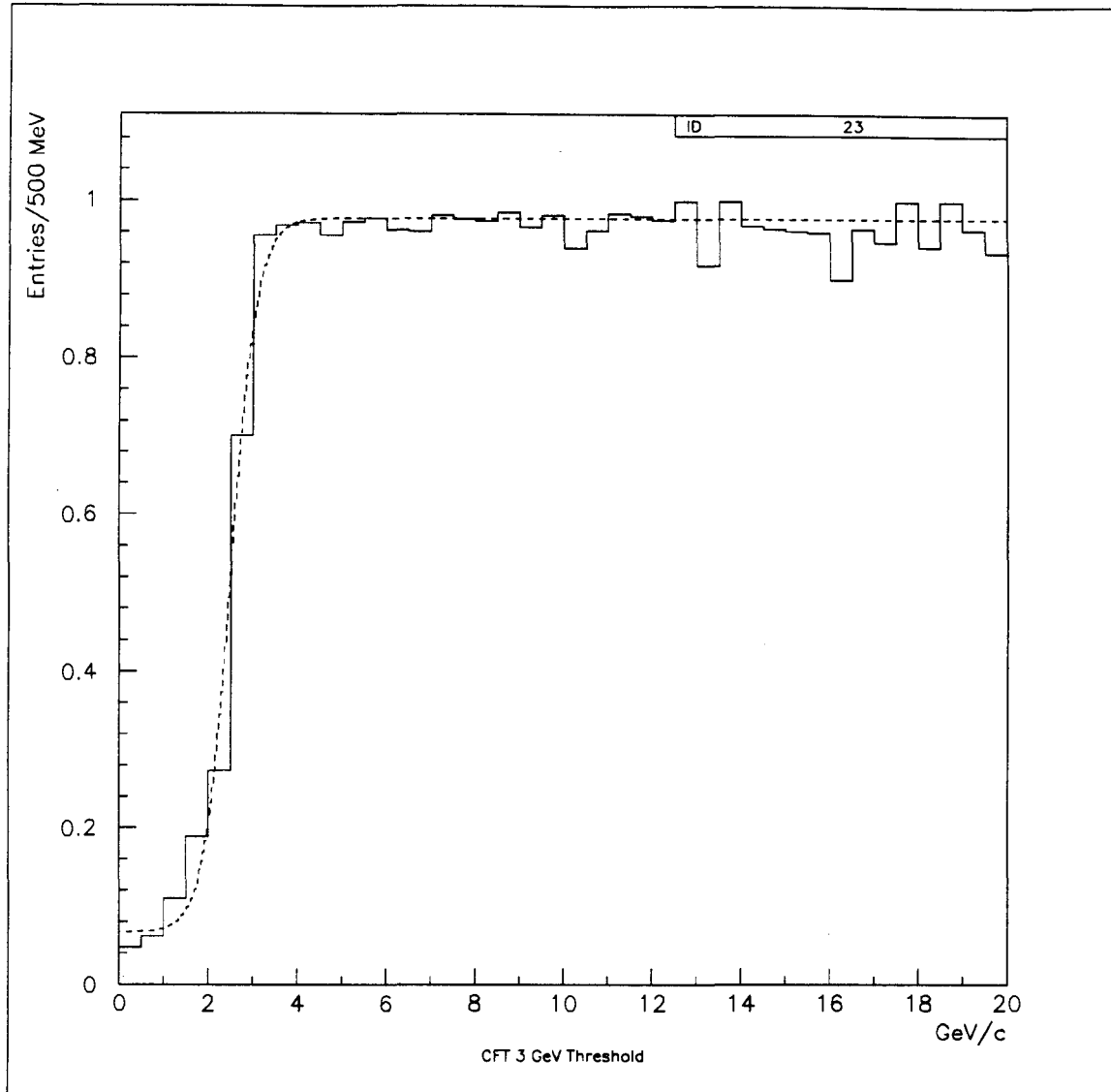
Figure 4.12: Efficiency of the CFT trackfinder with the nominal 3 GeV/c threshold.

Hardware Problems Early in the Run

Early in the 1988-1989 Collider run, problems with the Level 2 trigger system resulted in the loss of identified gold muons. Investigations of this problem revealed that timing problems inhibited the identification of gold muons to the Level 2 trigger processors. The problem was limited to events with only one gold muon in the event and to those events where the associated CFT track happened to be the last CFT track processed.

Evidence of the problem was checked for in the J/ψ data by comparing the number of times a gold muon was associated with the last CFT track during the runs with the problem to the number of these events during the rest of the runs (see Figure 4.13). The ratio of luminosities for the two periods was 0.567. Gold muons not associated with the last CFT track were consistent with this ratio, while the ratio for gold muons matched to the last CFT track gave a ratio of 0.35 ± 0.09. This implied that the fraction of events not triggering was 0.38 ± 0.16 for data taken with the problem. This fraction was accounted for in the measurement of the 2 GeV/c threshold by assuming an equivalent loss of luminosity. The same factor was also utilized as an inefficiency in the reconstruction of B^0 mesons discussed in Section 4.2.

4.1.2 Efficiency of the Level 2 Dimuon_3_3 Trigger

As stated above, the efficiency for the Dimuon_3_3 trigger was taken to be the product of the efficiencies for each muon to pass both the CFT 3 GeV/c threshold and the Central_Muon_3 trigger.

The efficiency of the Central_Muon_3 trigger was previously measured in a separate analysis [41]. The efficiency was obtained from $\bar{p}p$ data using a technique similar to that employed in the measurement of the Central_Muon_5 trigger efficiency, but using a different
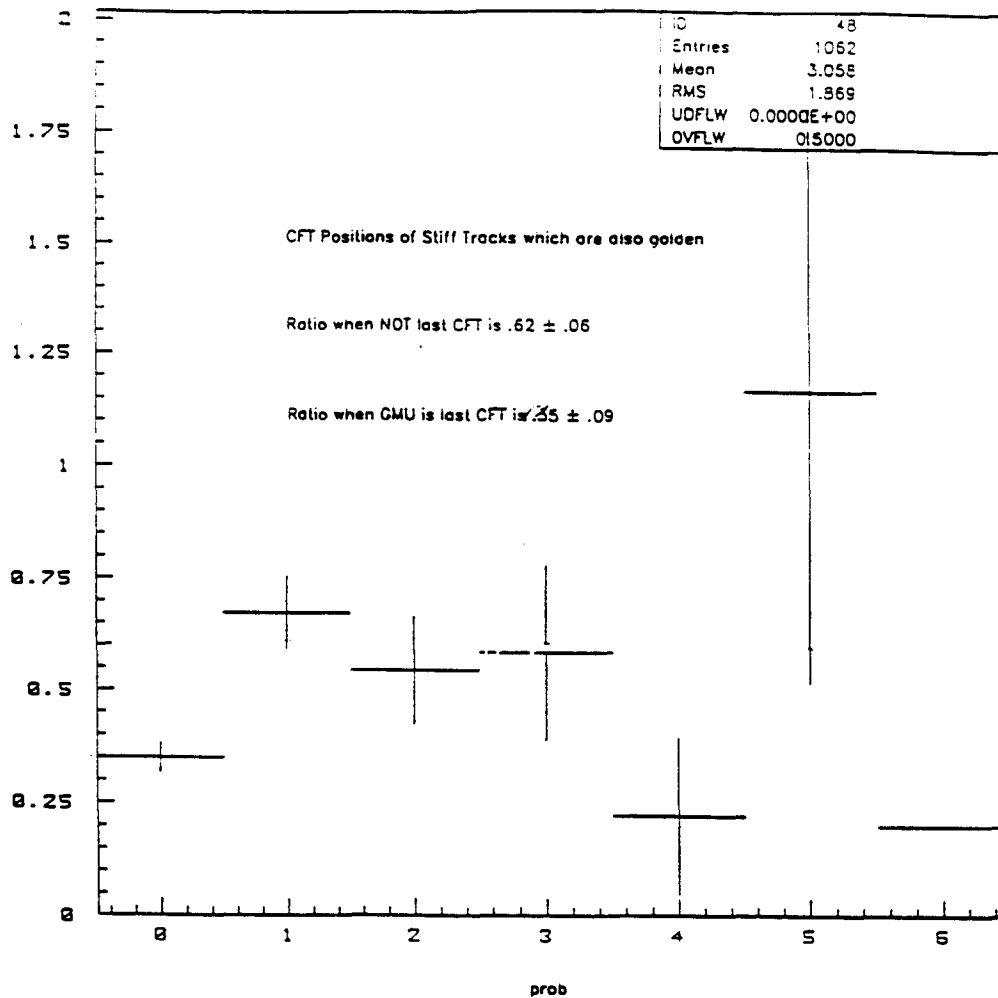
Figure 4.13: Hardware losses of muons early in the 1988-1989 collider run. The plot shows the ratio of the number of gold muons identified to the trigger processors between the period of the run with the problem to that without the problem, as a function of which CFT track the muon was identified with. The first bin corresponds to those cases when a gold muon was identified with the last track identified by the CFT. The second bin corresponds to the cases when a gold muon was matched to the next-to-last CFT track, etc. If there had been no loss of events, the ratio would be 0.567.

method to estimate the background. Instead of relying on the matching distributions, the background was estimated with the distribution of energy deposited in the calorimetry by the muons. The Level 1 Central_Muon_3 trigger efficiency is shown in Figure 4.14 together with the best fit of the data to the same parameterization applied to the Central_Muon_5 trigger efficiency measurement.

4.2 Monte Carlo Results

A Monte Carlo simulation of the production and detection of the decay $B^0 \to J/\psi \, K^{0*}$ was used to estimate the acceptance of the CDF detector and to establish the cuts for isolating the signal from combinatoric background. The simulation was also employed to estimate the efficiency of the cuts.

This section is divided as follows. First, the generator and detector simulation are described. The simulated data set is then examined and the selection algorithm for B^0's is described. Finally, the overall efficiency and a summary of the B^0 finding procedure are given.

4.2.1 Monte Carlo Generation of B^0 mesons using the NDE predictions

The Monte Carlo produced b quarks in the rapidity range $|y| < 1.5$ with a P_T distribution of the same shape as that predicted by NDE (see Chapter 1). Figures 4.15 and 4.16 show the P_T and rapidity distributions of b quarks produced by the NDE Monte Carlo generator.

The kinematics of the B^0 meson were obtained from that of the b quark using the Peterson fragmentation model [42] for the energy and momentum along the b quark flight direction and an ansatz for the momentum perpendicular to the b quark flight direction. The
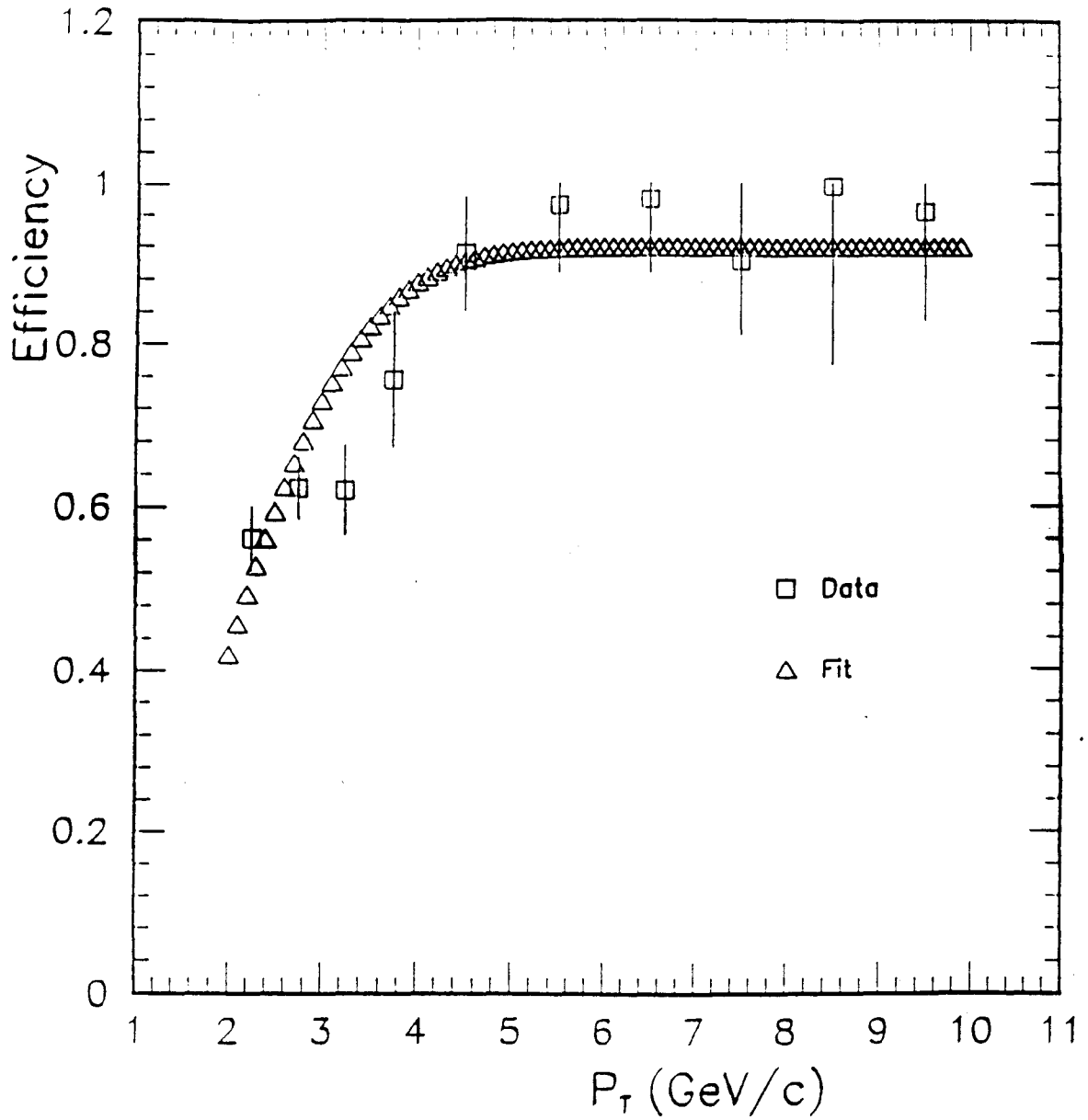
Figure 4.14: Efficiency of the Level 1 Central_Muon_3 trigger (From Reference [41]).
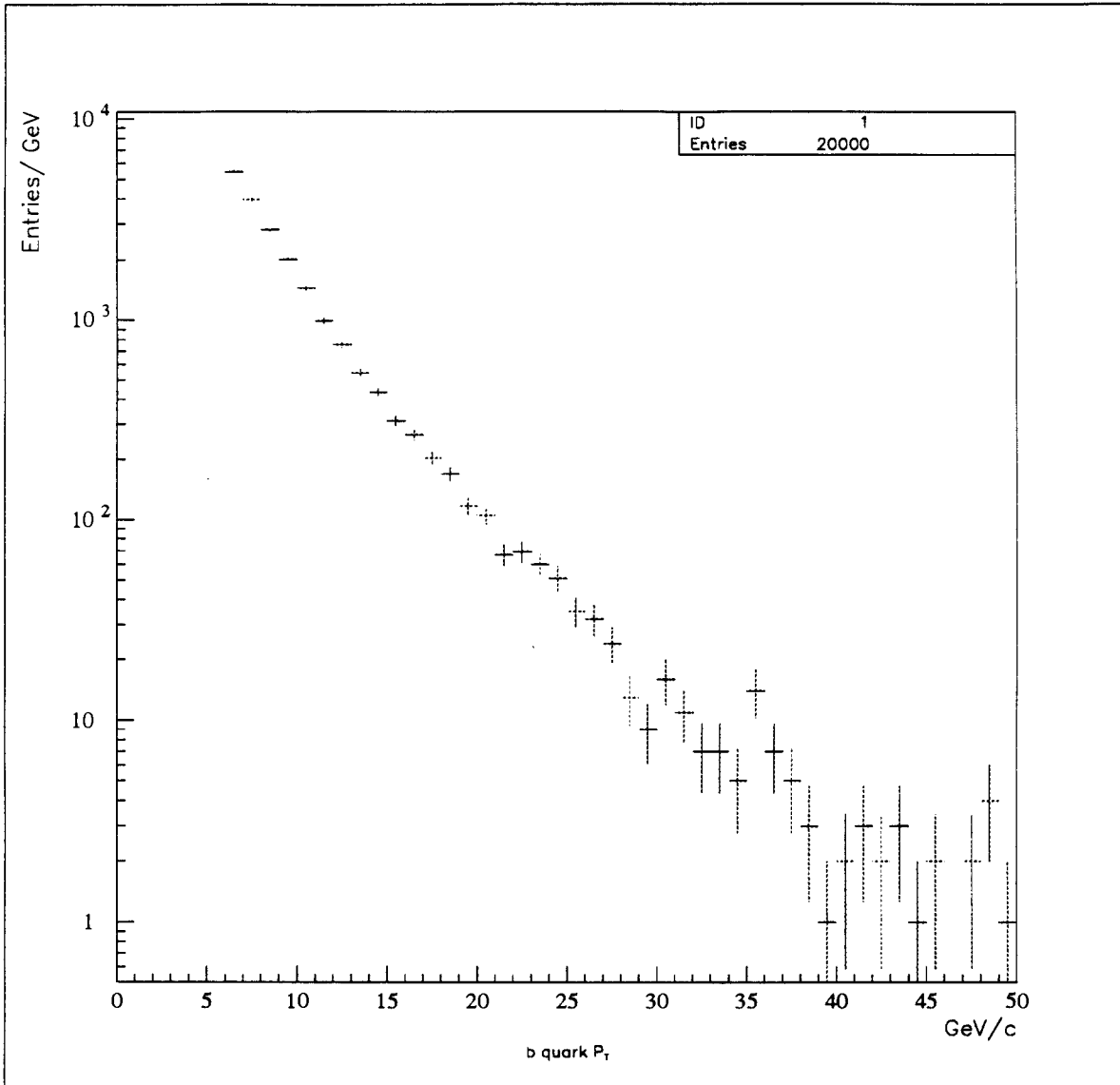
Figure 4.15: b quark P_T distribution from a Monte Carlo using the NDE calculation.
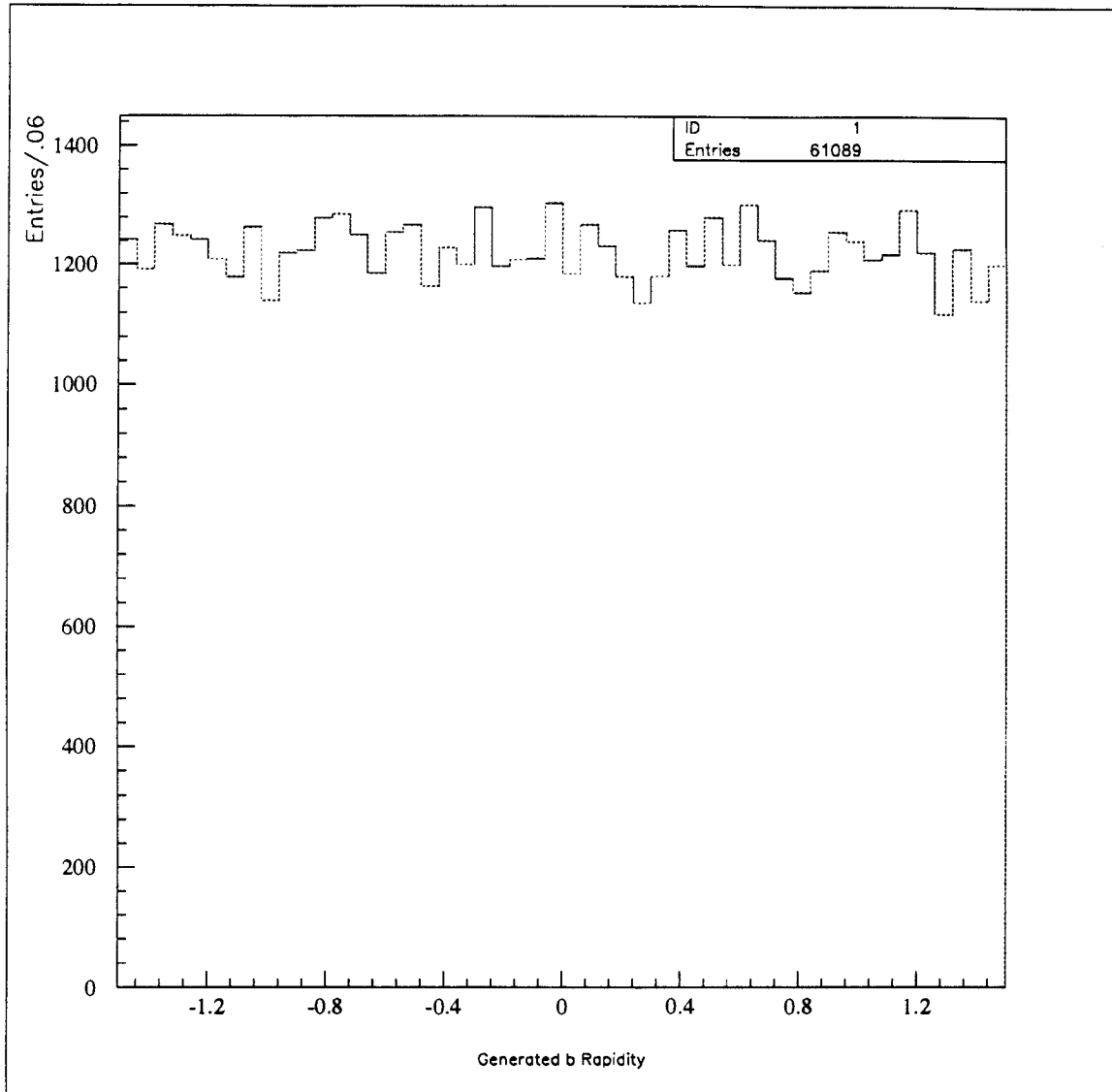
Figure 4.16: *b* quark *y* distribution from a Monte Carlo using the NDE calculation.

Peterson model was an analytic parameterization of the amount of energy and momentum carried by a meson which was produced from a fragmenting quark. The ansatz was based on a picture of fragmentation first described by Field and Feynman [43]. Specifically, the Peterson model gave the energy carried by the resulting meson via the expression:

$$P(z) = \frac{Nz(1-z)^2}{[(1-z)^2 + \epsilon z]^2}. \tag{4.6}$$

Here ϵ is a free parameter which is determined by experiment, $z \equiv (E + p_{\parallel})_{hadron}/(E + p_{\parallel})_{quark}$, and $P(z)$ is the probability of the B^0 having a particular value of z. Present measurements of ϵ imply that for B^0 mesons $\epsilon = 0.006 \pm 0.002$ [44]. Figure 4.17 shows the distribution of z for $\epsilon = 0.004, 0.006,$ and 0.008. Note that the larger value of ϵ corresponds to a softer b quark fragmentation.

The magnitude of the B^0 momentum transverse to the quark flight direction was given by uncertainty principle arguments to be roughly on the order of $\hbar$ divided by typical hadronic sizes. This gave a typical momentum scale of $\sim$300 MeV/c. The functional form which described the distribution of this momentum was given by the ansatz

$$f(p_T) = \frac{1}{1 + bp_T{}^2}, \tag{4.7}$$

where b is a constant chosen to give a mean p_T of 350 MeV/c and p_T is the momentum of the B^0 perpendicular to the b quark flight direction.

After determining the lab four-momentum of the B^0 meson, the decay of the meson into a J/ψ and K^{0*} was simulated. The simulation of the B^0 decay included the effects of the finite K^{0*} width (about 50 MeV/c^2 [45]) and the finite B^0 meson lifetime. The K^{0*} width was incorporated by using a non-relativistic Breit-Wigner equation to describe the probability that a K^{0*} had a particular mass. For the K^{0*} mass generated in an event, the momenta of the J/ψ and K^{0*} (and subsequently the $\mu^{\pm}$, K, and π) were calculated using
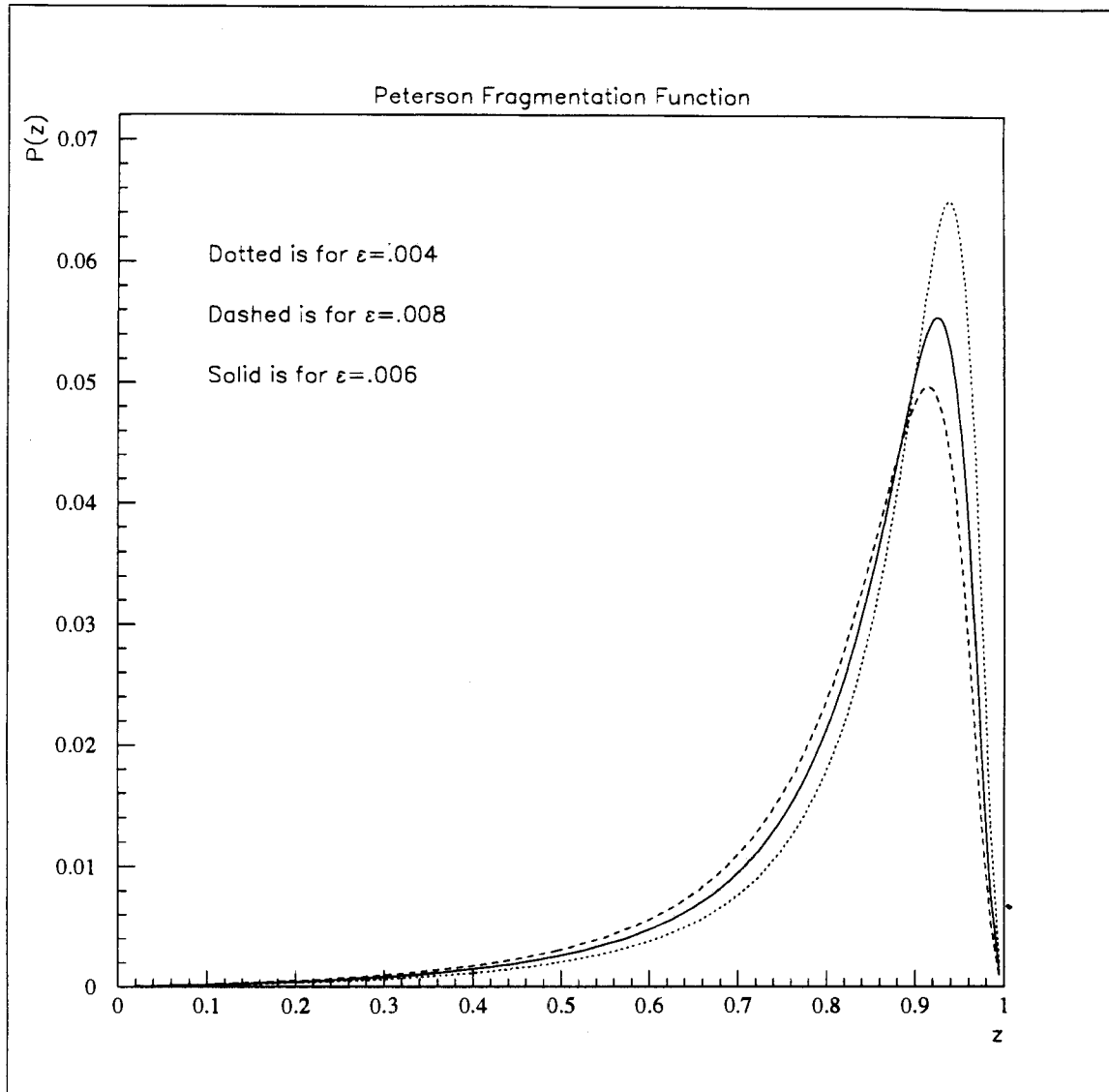
Figure 4.17: Peterson fragmentation function for $\epsilon = 0.004, 0.006$, and 0.008.

conventional two-body decay kinematics.

The B^0 lifetime has been measured by several experiments [46] to be 1.29 ± 0.08 psec. This value was used as the mean lifetime of the B^0's created in the Monte Carlo data.

The J/ψ and K^{0*} are both vector mesons and could, in principle, be polarized in the B^0 decay. This would result in a variety of different angular distributions of the final state K, π, and μ pair. The formalism describing the angular distributions of polarized vector mesons is reviewed in Appendix C. Partial information on the polarization of the J/ψ from other experiments was available [47] but not yet very precise. In this analysis, the K^{0*} and J/ψ were assumed to be unpolarized, and the variation of the acceptance with different polarizations was taken as a systematic uncertainty. Monte Carlo studies indicated that the acceptance relative to unpolarized decays could be as low as 80% and that the acceptance was greatest for the unpolarized case. The systematic error on the acceptance due to possible $J/\psi\,K^{0*}$ polarization was therefore taken to be $^{+0}_{-20}\%$. Table 4.2 shows the acceptance for different parameters describing the polarization relative to the acceptance for unpolarized decays. These parameters are described in greater detail in Appendix C.

4.2.2 Simulation of the CDF Detector

A simulation of the CDF detector was used to obtain the proper detector response and geometric acceptance. The simulation included the following effects:

- dE/dX energy loss of particles traversing the detector;

- Decay-in-flight of unstable particles in the event. This included the decays of the charged K and π mesons and of muons;

- Spread in the z position of primary event vertices. The z vertex was assumed to be distributed according to a Gaussian with a σ of 30 cm;

Γ_T/Γ	$\alpha_1 = 0.0,\ \alpha_2 = 0.0$	$\alpha_1 = -0.621,\ \alpha_2 = 0.123$	$\alpha_1 = -0.462,\ \alpha_2 = 0.0108$
0.0	0.77	0.81	0.77
0.2	0.87	0.93	0.84
0.4	0.96	0.90	0.92
0.6	0.99	0.94	0.99
0.8	1.00	0.93	0.99
1.0	0.98	0.98	0.98

Table 4.2: Relative acceptances for different polarizations of J/ψ and K^{0*} mesons in the decay $B^0 \to J/\psi\ K^{0*}$. The parameter Γ_T/Γ describes the contribution to the B^0 decay from transversely polarized K^{0*} and J/ψ mesons. The parameters α_1 and α_2 originate from interference effects (see Appendix C).

- Delta ray production of energetic electrons resulting from the interaction of particles with material in the detector;

- Multiple Coulomb Scattering, implemented using Moliére theory [48];

- CTC layer dependent efficiencies and resolutions.

The last item requires some elaboration. The process of reconstructing charged particle tracks in a hadron collider environment was non-trivial. Of special concern were the high track multiplicities (typically $\sim$ 50 in candidate J/ψ events). At the inner layers of the CTC the hit density was markedly higher than at the outer layers. This could cause confusion during the pattern recognition where hits on each wire were associated with tracks. Mis-association of hits would appear to worsen the spatial resolution of the tracking chamber since hits which did not really belong with a given track were associated with the track.

Figure 4.18 shows the distribution of the mean spatial residuals for tracks reconstructed in the CTC as a function of CTC layer for J/ψ events [49]. It shows that the resolution of the CTC was nearly twice as large at the inner layers as the outer layers.

The fitting of tracks to the identified hits was also complicated by the high track density in the CTC. If a cell in the CTC was traversed by more than one particle, the added signal caused the time-over-threshold measured by the TDC's (see Chapter 3) to be artificially high. The track fitting procedure would often ignore these hits and the efficiency of the individual wires would therefore appear to be smaller in the inner layers. Figure 4.19 shows the fraction of tracks which included a hit from a wire at a given radius [49]. This data was from J/ψ events. The distribution shows that at the inner radii, hits were included less frequently than hits at the outer radii.

It should be noted that since these resolutions and efficiency effects were expected to be due to track multiplicities, a dependence on the event type may have been present. The J/ψ's from which the efficiencies and resolutions were derived originated from B decays and from the direct process $p\bar{p} \rightarrow J/\psi X$. The fraction of J/ψ's which originated from decays of B's was estimated to be approximately 65% [50]. The track multiplicity in the direct events may be slightly different from B events but should not significantly affect the residual and efficiency distributions.

The Monte Carlo generator included no tracks other than those in the $B^0 \rightarrow J/\psi\ K^{0*}$ decay chain and therefore these efficiency and resolution effects were imposed on the simulation by using the measured wire resolutions and hit efficiencies found in J/ψ events. This was done via a multi-step process. During the initial simulation of charged tracks, the residuals from Figure 4.18 were used to generate the position of wire hits in the CTC. These hits were used by the pattern recognition to identify tracks. Once the tracks were found by the pattern recognition, hits in each track were randomly discarded according to

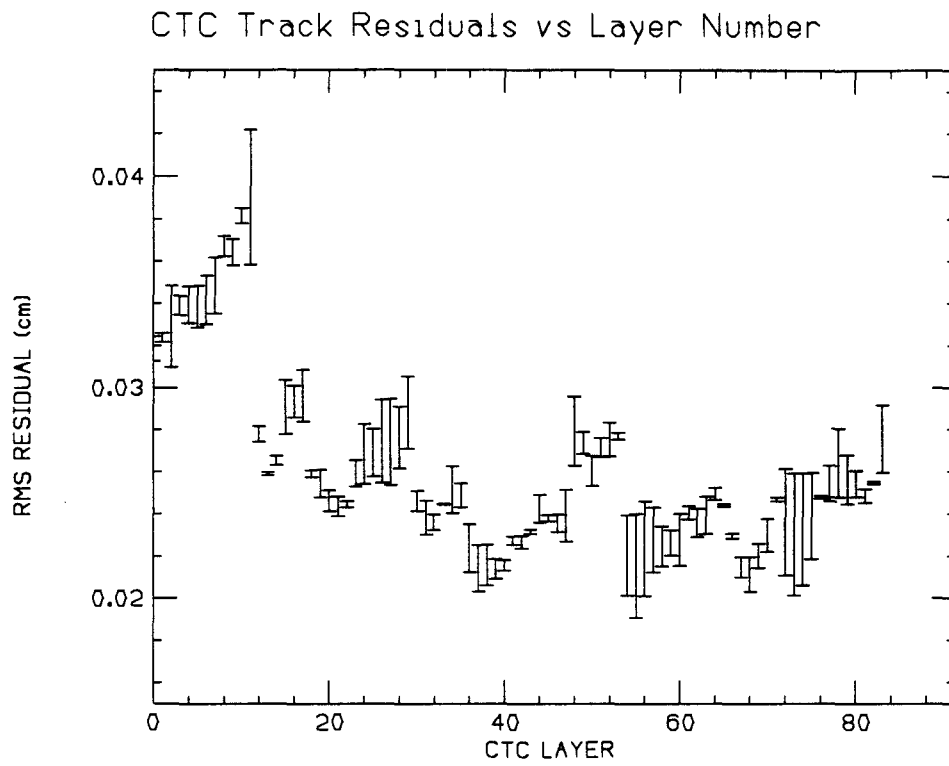CTC Track Residuals vs Layer Number

Figure 4.18: Measured residuals for reconstructed tracks in J/ψ events as a function of CTC layer number.
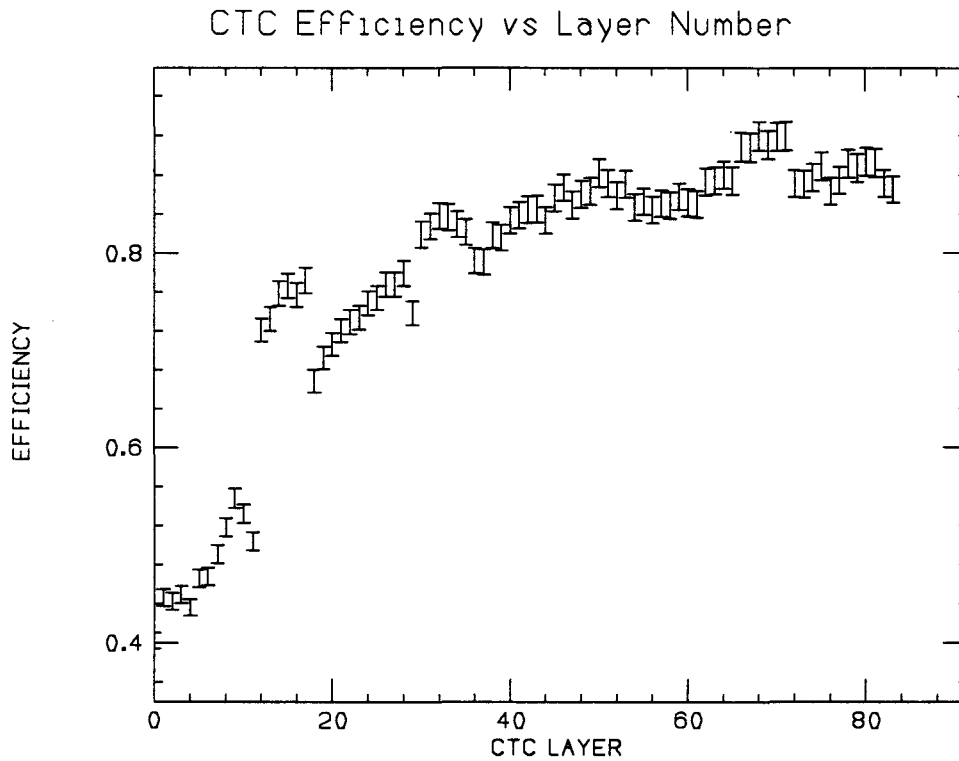
Figure 4.19: Hit 'Efficiency' in the CTC as a function of CTC layer. The efficiency here is defined to be the fraction of the time that a wire in a layer was actually used in the fit to a reconstructed track. The data was obtained from J/ψ events.

the distribution in Figure 4.19 and the track was refit.

This treatment of the CTC simulation resulted in simulated J/ψ events which showed a mass resolution for J/ψ 's similar to that observed in the data. Figure 4.20 shows the reconstructed J/ψ events from simulated data and J/ψ 's observed in the $\bar{p}p$ collision data. The fitted width of the J/ψ's in the simulated data was approximately 18.5 MeV/c^2 compared to 23 MeV/c^2 observed in the data, approximately a 20% difference. This difference between the simulated and observed widths can be attributed to a number of causes. First, the J/ψ's from $\bar{p}p$ data were observed to have a somewhat asymmetric shape not observed in the simulated J/ψ's which was possibly due to initial state radiation. Secondly, the presence of other tracks in the event may have affected the quality of the track parameters in addition to the spatial resolution and the efficiency. Additionally, the model used to implement the CTC wire resolutions and efficiencies was only intended to approximate the effects of these quantities on the pattern recognition and track fitting. Finally, the discrepancy in the mass resolution between the simulated and observed J/ψ's will be used as a 20% systematic error in the mass resolution for B^0's .

Cuts and Efficiencies

A set of simulated $B^0 \rightarrow J/\psi \ K^{0*}$ events was generated in order to arrive at an algorithm for finding B^0 mesons. The simulation of these events included the efficiencies of the dimuon triggers described in Section 4.1.

After the detector response to the simulated events was performed, different distributions were examined to isolate the B^0 meson signal. About 70,000 events were generated with equal numbers of $K^+\pi^-$ and $K^-\pi^+$. The b's were generated with P$_T$ above 6 GeV/c and $|y| < 1.5$. The cross section for the production of b's above P$_T{}^{min}$ was defined by the
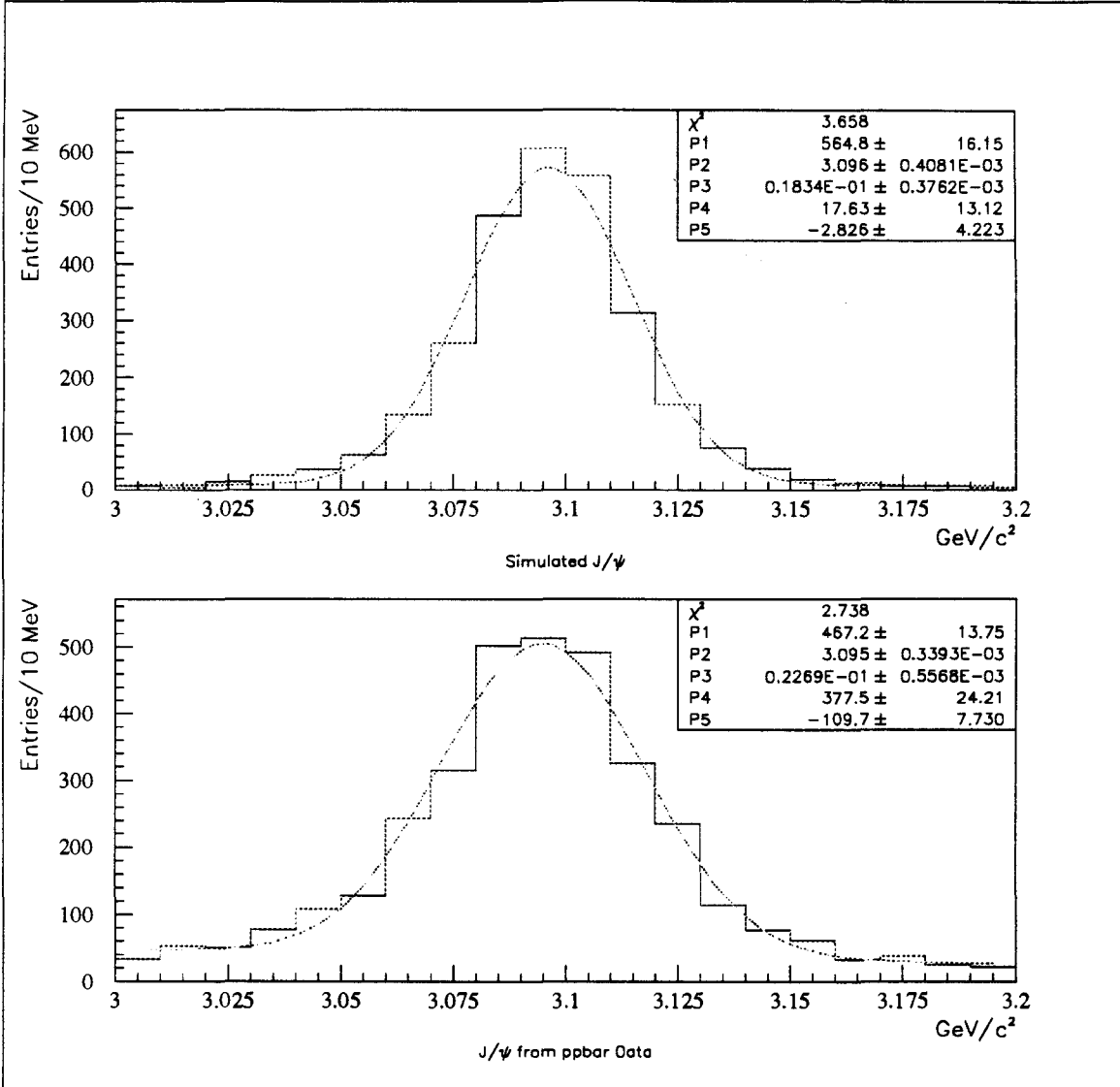
Figure 4.20: Reconstructed J/ψ peaks in (a) simulated events and (b) real data. Figure (a) includes the measured hit efficiencies and sense wire resolutions of the CTC.

relation:

$$\sigma = \frac{Number\ of\ b's\ produced\ with\ P_T > P_T^{min}}{Luminosity}. \tag{4.8}$$

The observed quantity was the number of reconstructed B^0's . The acceptance was therefore defined as:

$$Acceptance = \frac{Number\ of\ B^0's\ reconstructed}{Number\ of\ b's\ produced\ above\ P_T^{min}}. \tag{4.9}$$

Since no information was available about the P_T of the b quark which formed the B^0 , the numerator of the acceptance included b's with any P_T . Since the shape of the b quark P_T distribution was assumed to be that predicted by the NDE calculations, the measurement of the cross section for b's with P_T above P_T^{min} essentially determined the value of the cross section at any other value of P_T^{min} . Most of the reconstructed B^0's , however, originated from b quarks with values of P_T above some lower bound, and therefore the acceptance was not very sensitive to the assumed shape of the P_T distribution below this threshold. In the analysis presented in this thesis, P_T^{min} was defined to be 11.5 GeV/c. This value was chosen so that 90% of the reconstructed events originated from b quarks with the same or higher P_T .

Only b quarks with $|y| < 1.0$ were included in the calculation of the acceptance. Figure 4.21 shows the rapidity distribution of the b quarks from reconstructed B^0 events using the reconstruction algorithm detailed below. The distribution demonstrates that the reconstruction of B^0's was efficient only for b quarks produced within this rapidity range. Note that the rapidity of the b quarks produced by the Monte Carlo was assumed to be flat in the interval $|y| < 1.5$. The NDE analysis predicted the value of $d\sigma/dP_T dy$ at various values of P_T . The variation in the geometric acceptance with differing y distributions was studied with a Monte Carlo and a systematic uncertainty in the acceptance of $\pm 10\%$ was estimated.

Of the 70,000 b quarks generated, approximately 9100 had values of P_T and y which

were within the range required for the acceptance calculation. The B^0's from these b quarks were successfully reconstructed approximately 1-2% of the time. The most significant losses of events were due to the identification of and triggering on muon pairs. The muon pair from each J/ψ was within the fiducial volume of the CMU only about 42% of the time. Muon pairs which were within the fiducial volume of the CMU passed the dimuon triggers approximately 49 % of the time and 25 % of these satisfied the muon P_T cuts described below. Muon pairs were thus identified with an efficiency of only about 5%. As discussed in the rest of this section, the remaining inefficiency was due to a number of cuts placed on the events to isolate the B^0 signal.

Figure 4.22 shows the P_T spectrum for the soft leg of J/ψ 's after applying the Level 2 Dimuon_5_V2 trigger simulation and a 5.0 GeV/c cut on the P_T of the stiff leg. A minimum P_T of 1.43 GeV/c was needed for muons to reach the muon chambers. In order to avoid this P_T region, a cut of 2.0 GeV/c was placed on the soft muon in J/ψ decays when the Dimuon_5_V2 trigger was required. The muons passing the Level 2 Dimuon_3_3 trigger were required to have P_T above 3 GeV/c. In this P_T region, the trigger was efficient and well understood.

Figures 4.23 and 4.24 show the P_T distributions of the K and π mesons in events with simulated J/ψ 's passing the trigger and muon acceptance requirements. The K P_T distribution rises and peaks near 1.0 GeV/c and falls after that. A cut on the K P_T greater than 1 GeV/c will thus be efficient for reconstructing B^0's and will reduce the amount of background from random tracks. The π P_T distribution shows no obvious point at which it would have been efficient to place a similar cut. As charged particles needed a P_T larger than 450 MeV/c to leave the CTC, a cut of P_T larger than 500 MeV/c was placed on π candidates. The $KP_T > 1$ GeV/c and $\pi P_T > 0.5$ GeV/c were approximately 49% efficient for selecting events containing a triggered J/ψ .
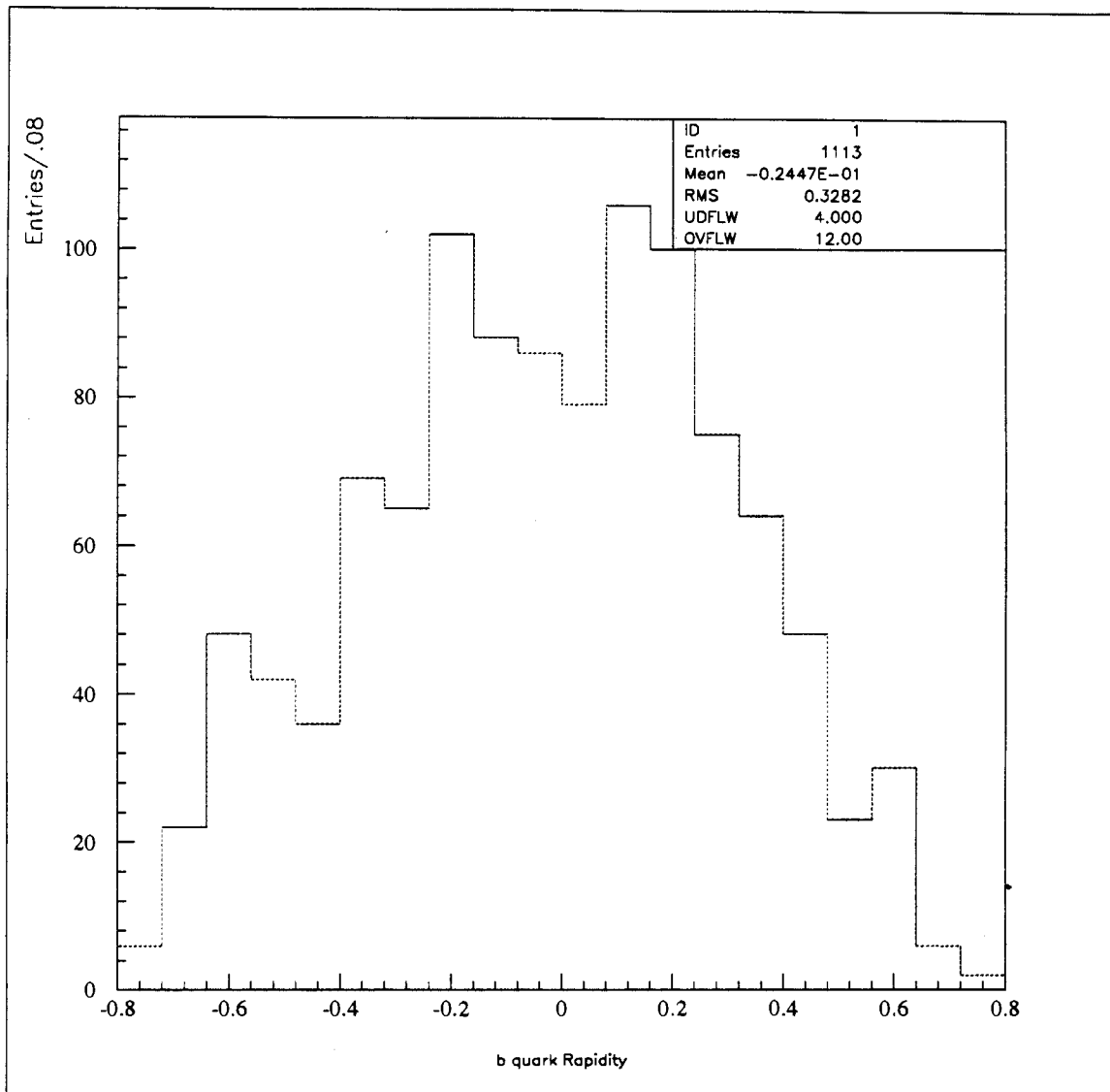
Figure 4.21: b quark y distribution from successfully reconstructed B^0 events in simulated data.
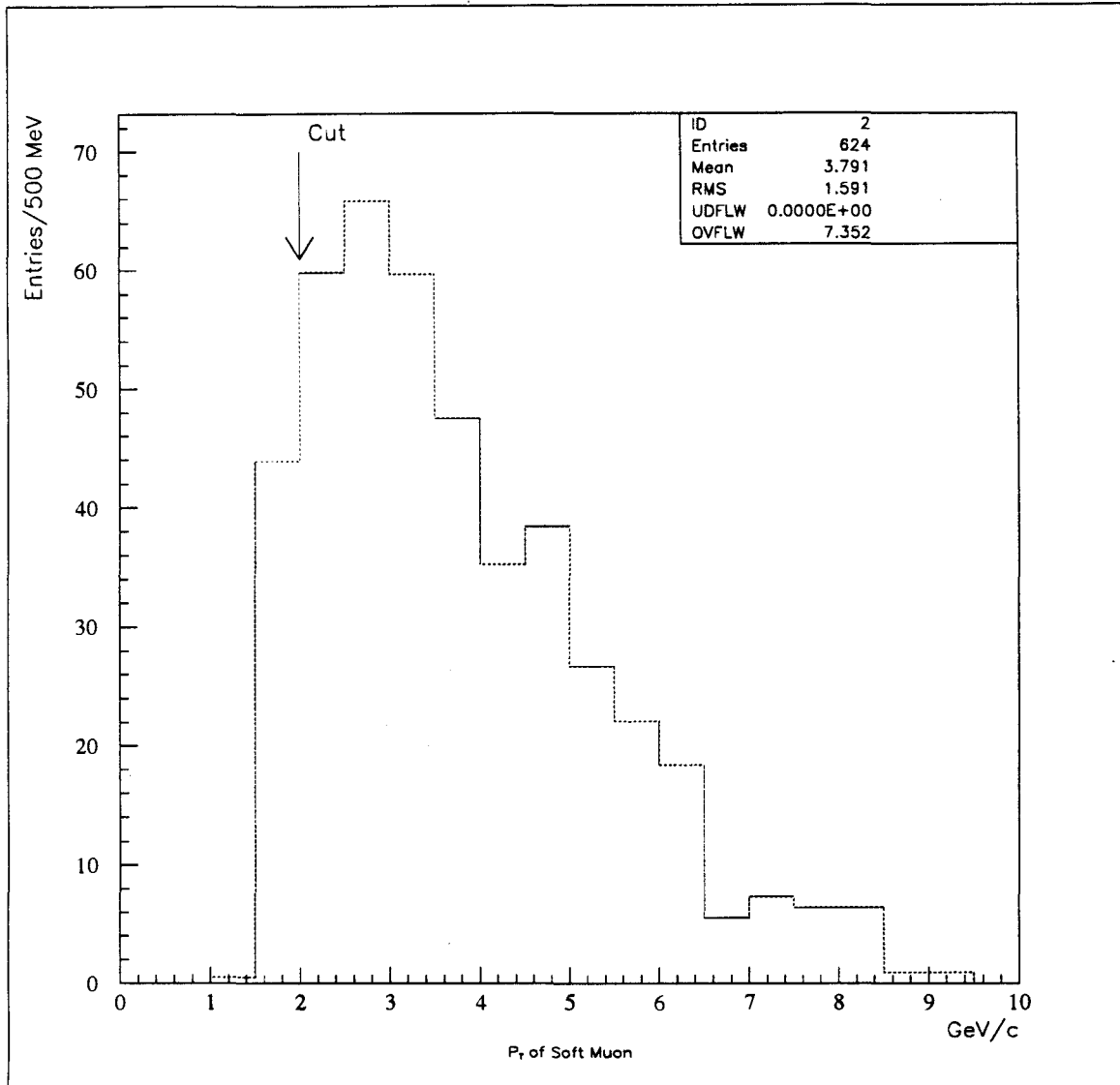
Figure 4.22: P_T distribution of the softer leg in simulated $B^0 \rightarrow J/\psi\ K^{0*}$ decays. The distribution includes a 5 GeV/c cut on the P_T of the stiff leg and the effects of the Dimuon_5_V2 trigger.
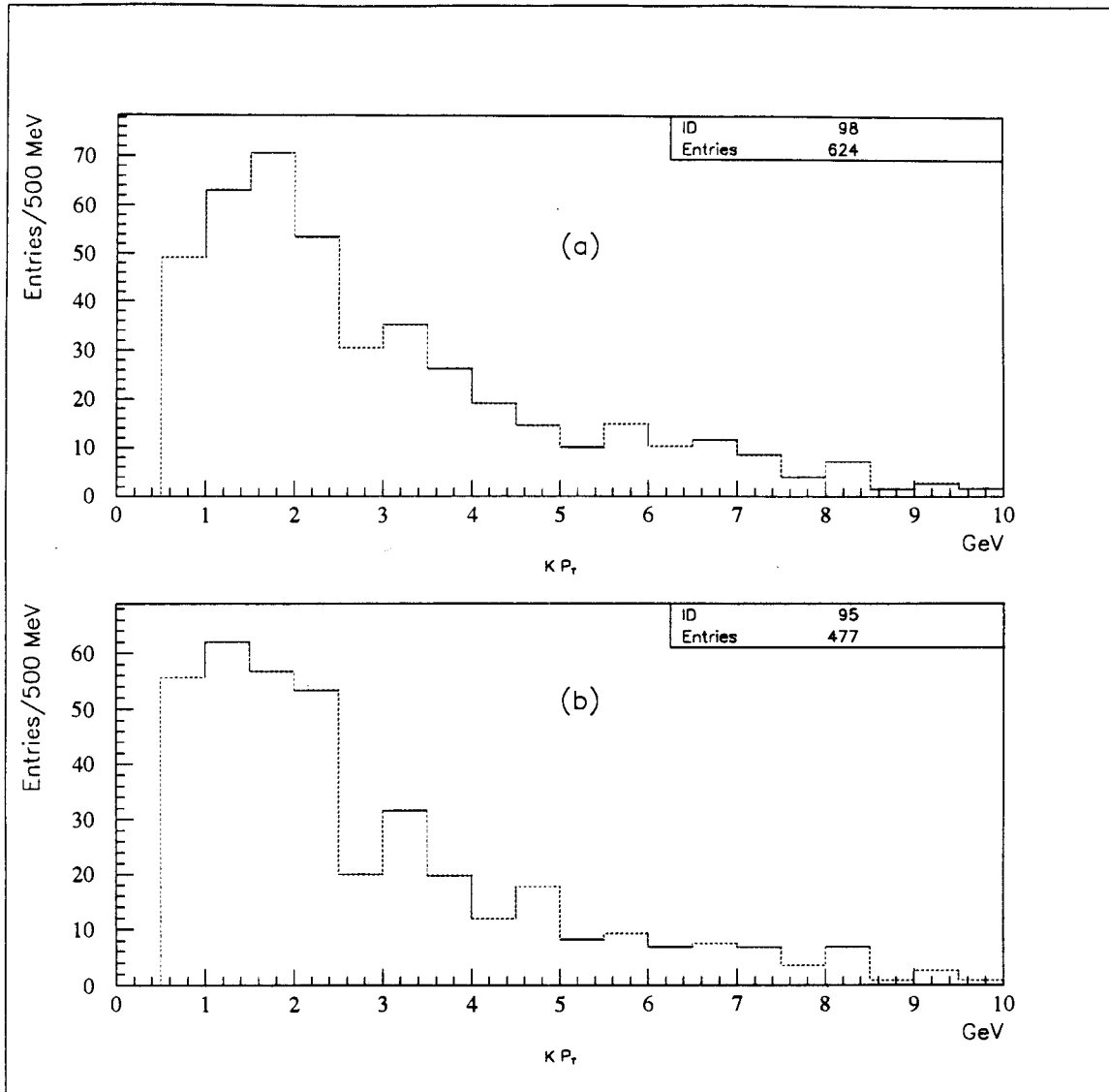
Figure 4.23: P_T distribution of Kaons in simulated $B^0 \rightarrow J/\psi \; K^{0*}$ decays where a J/ψ has been reconstructed and passed either the Dimuon_5_V2 trigger (Figure (a)) or the Dimuon_3_3 (Figure (b)) trigger.
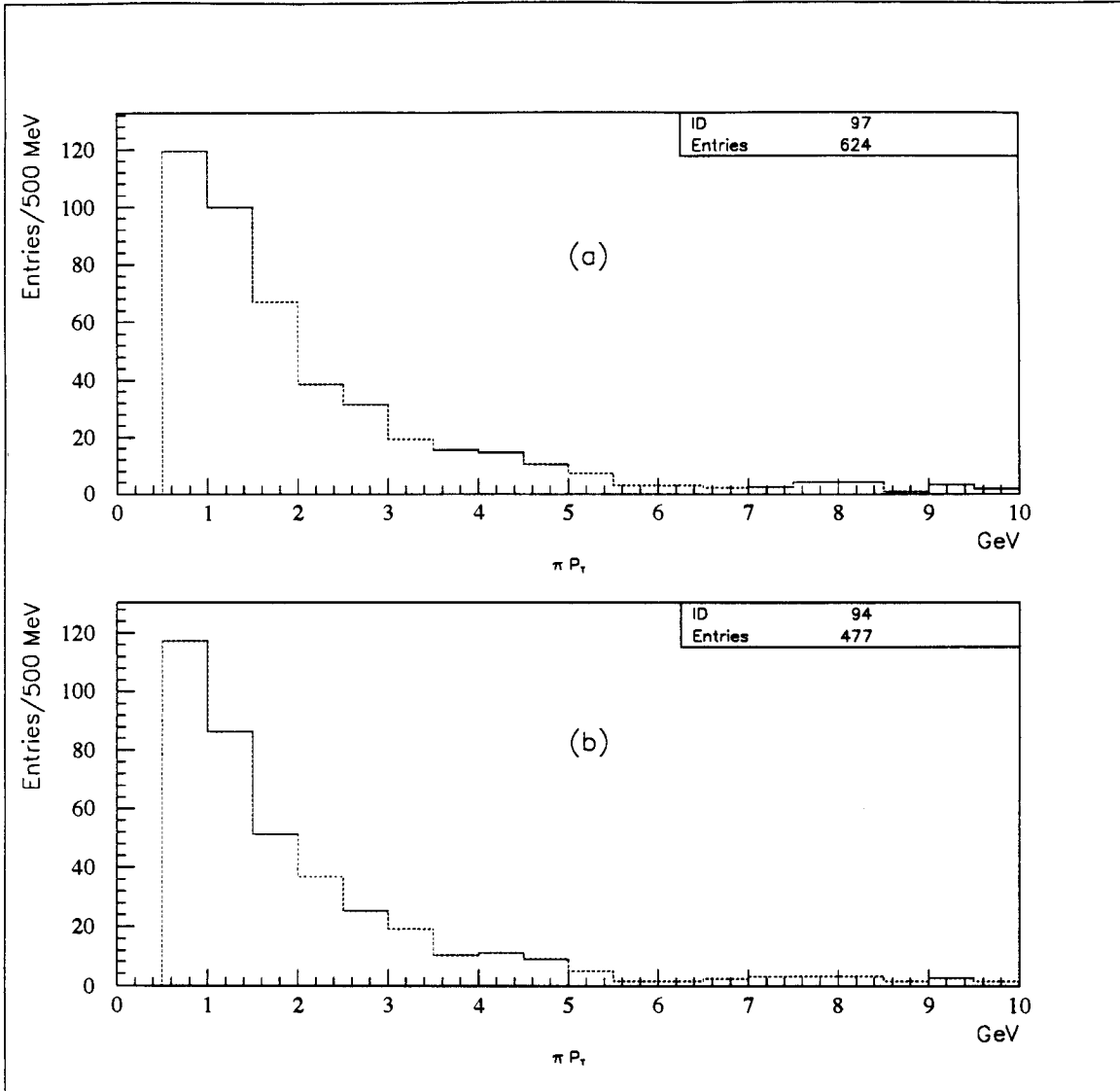
Figure 4.24: P_T distribution of π's in simulated $B^0 \rightarrow J/\psi \ K^{0*}$ decays where a J/ψ has been reconstructed and passed either the Dimuon_5_V2 trigger (Figure (a)) or the Dimuon_3_3 (Figure (b)) trigger.

Because CDF had no particle identification, the observation of a K^{0*} signal necessarily used only oppositely charge tracks. Candidate K^{0*}'s were defined by imposing a mass cut around the K^{0*} mass. Figure 4.25 shows the reconstructed K^{0*} mass in simulated events after the P_T cuts described above were implemented. The distribution has an RMS of 55 MeV/c^2, implying that the mass resolution was dominated by the natural width of the meson. Because of this distribution, the mass window used to identify K^{0*} mesons was chosen to be ± 50 MeV/c^2 centered around the mean K^{0*} mass of 0.896 GeV/c^2.

As will be discussed in Section 4.3.1, the reconstruction of the J/ψ's was accomplished using tracks which were constrained to have originated at a common vertex. The tracks associated with a candidate K^{0*} were then also constrained to have originated at the same vertex while simultaneously constraining the J/ψ to have the current world average mass (3.09693 ± 0.00009 GeV/c^2 [51]). Figure 4.26 shows the reconstructed B^0 signals with and without the mass constraint. It illustrates that in simulated events, the mass constraint improved the B^0 mass resolution by approximately a factor of two, allowing smaller binning to be used in the B^0 data which in turn which should result in an increase in the signal-to-background ratio.

Using the above cuts, the B^0 meson signal reconstructed in the simulated data is shown in Figure 4.27 for both the Dimuon_3_3 and Dimuon_5_V2 triggers. Fitting each distribution to a Gaussian distribution produced a mass resolution of approximately 12-13 MeV/c^2.

Unfortunately, the resolution and efficiency quoted above do not account for an additional feature of the decay $B^0 \rightarrow J/\psi K^{0*}$. A property of this particular decay chain is the insensitivity of the reconstructed B^0 mass to an interchange of the K and π mass assignments. This meant that if the CTC track associated with the K was assigned the π mass and vice-versa, and the $K\pi$ invariant mass remained in the K^{0*} mass window, then it was likely that the resulting B^0 candidate would also be near the B^0 mass. This could
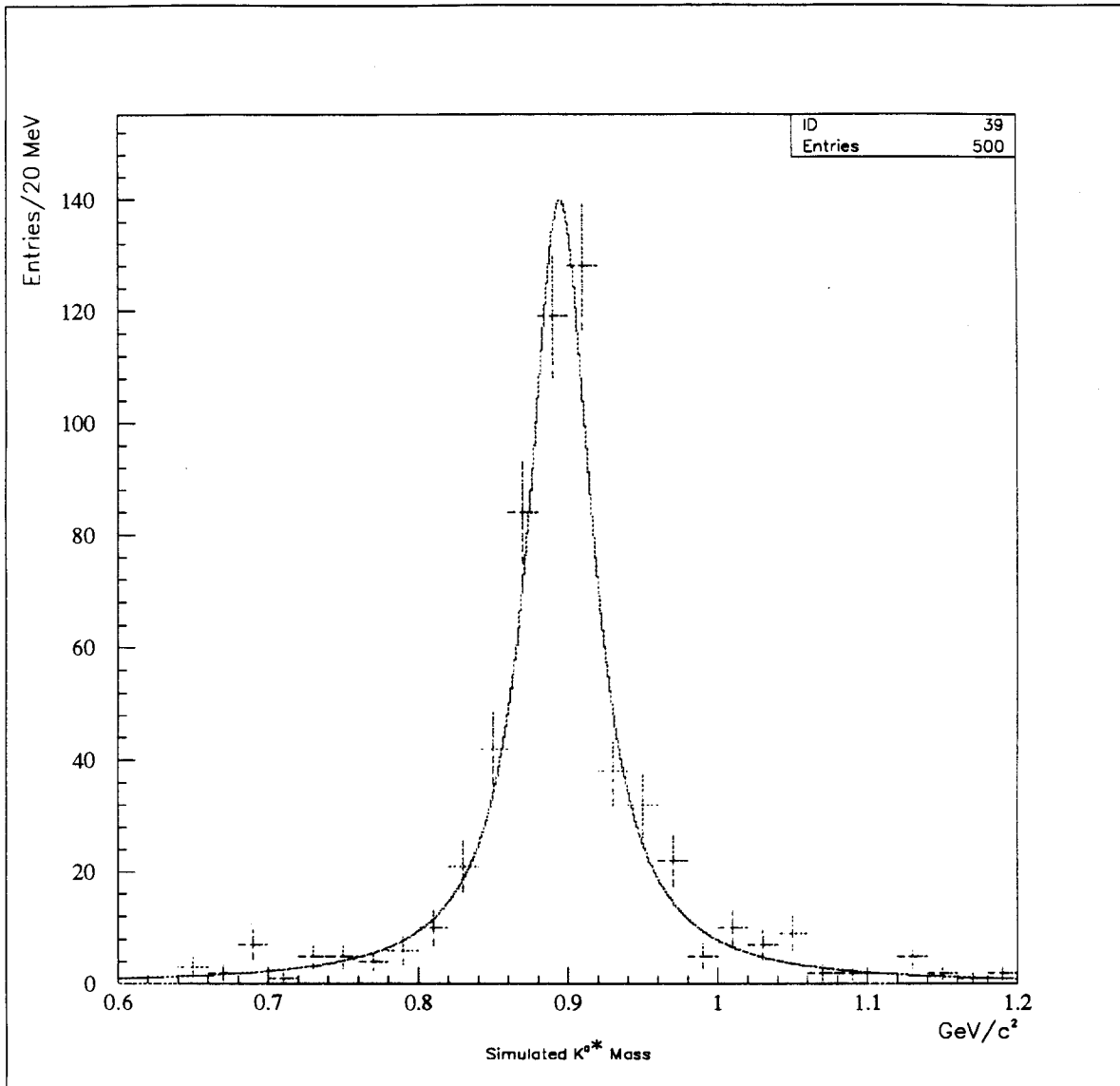
Figure 4.25: Reconstructed K^{0*} signal in simulated events. The width of the distribution is nearly that expected due to the natural K^{0*} width (about 50 MeV/c^2).
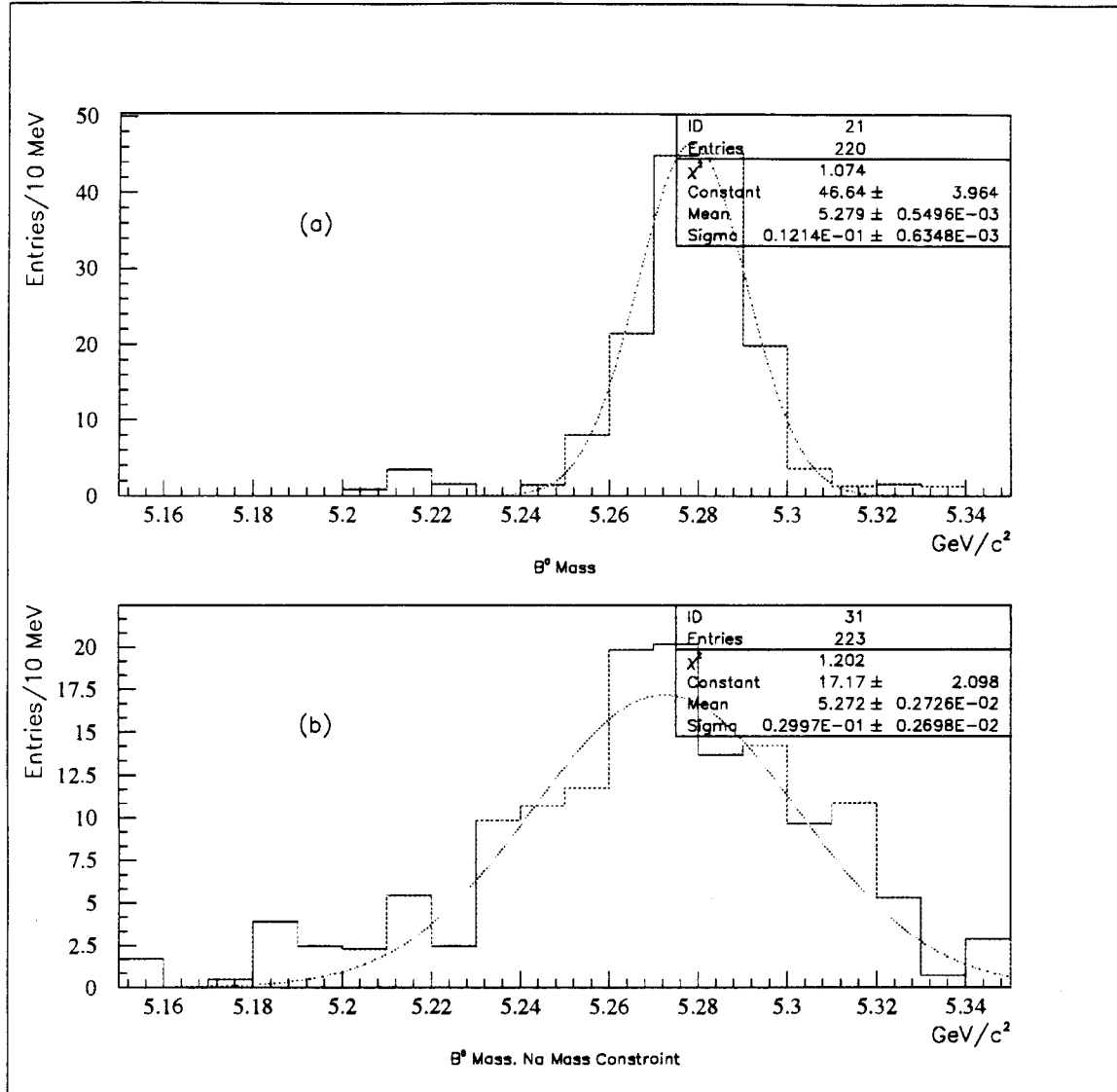
Figure 4.26: Reconstructed B^0 mass from simulated data, using the Dimuon_5_V2 trigger. Figure (a) used a simultaneous mass-vertex constraint and (b) used only the common vertex constraint.
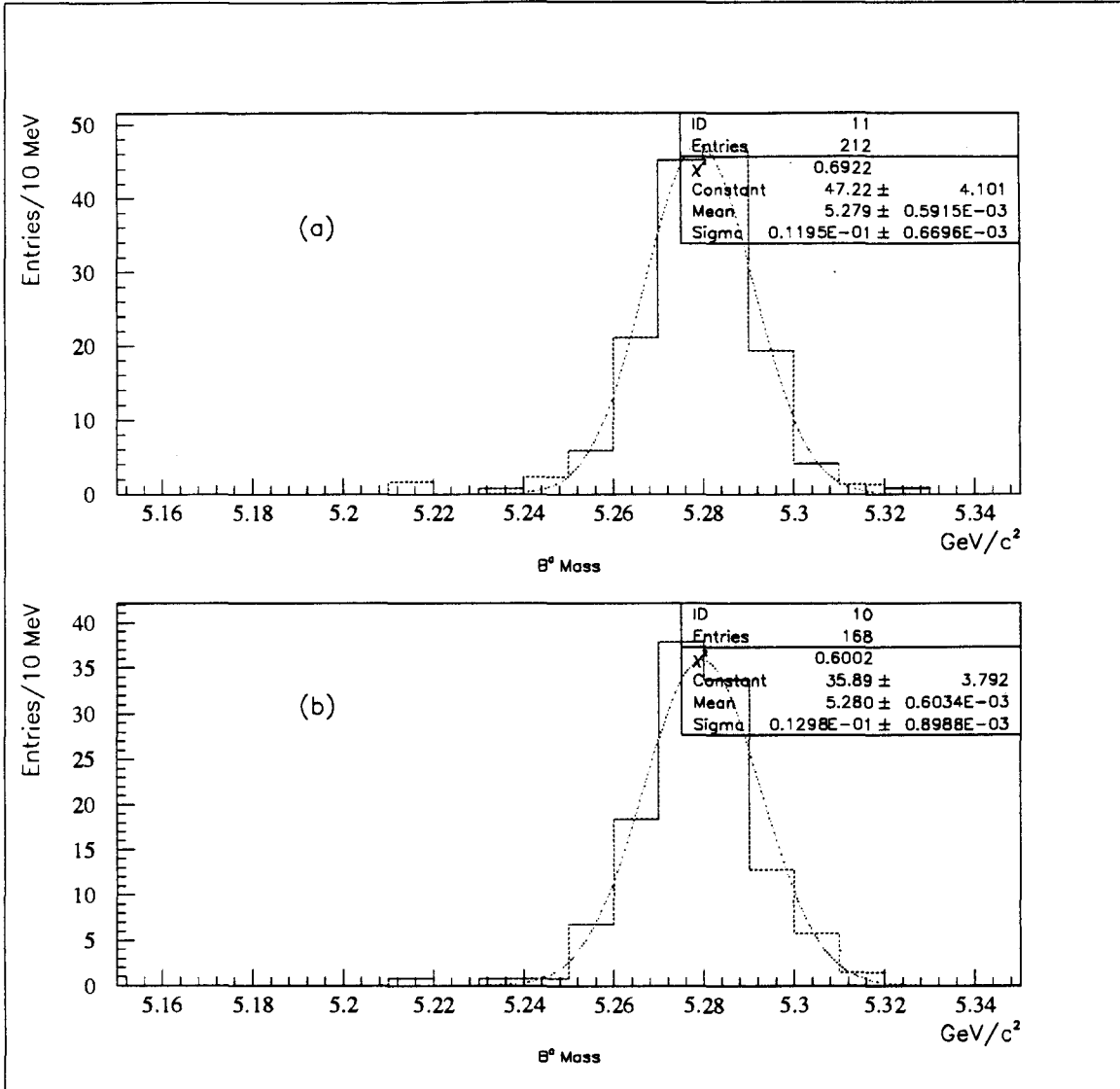
Figure 4.27: Reconstructed B^0 mass from simulated data using a simultaneous mass-vertex constraint. Figure (a) used the Dimuon_5_V2 trigger and (b) used the Dimuon_3_3 trigger.

result in a double-counting and an overestimate of the number of B^0 mesons.

To resolve this ambiguity, a procedure for accepting only one candidate was devised. One possible method was to designate the track with larger P_T the K and the other track the π. Since the K has a larger mass, it would be expected to carry a larger momentum than the π. This procedure was estimated by using simulated events to be only about 60% efficient at assigning the correct combination. An alternate method was to select the K^{0*} candidate which was closer to the K^{0*} mean mass. This method was predicted by the simulation to be only slightly more efficient (65%). The latter was chosen based on its slightly higher efficiency. It should be stressed that in either case, the number of B^0 mesons is correct, even if the wrong $K\pi$ combination is chosen since the K^{0*} kinematics is similar for both cases. Figure 4.28 shows the mass distribution of reconstructed B^0 mesons for this procedure along with that of the reconstructed mass for B^0 mesons where only the correct combination was used. Note that the fitted mass is only slightly different from the true mass and the fitted resolution is within 1 MeV/c² of that for the correct combinations. Figure 4.28 shows the resolution for each of the two triggers. For each trigger, the effect of wrong mass assignments on the resolution is smaller than the uncertainty in the resolution and is not statistically significant.

There were several other effects which reduced the efficiency and were not included in the simulated data. These effects include the muon matching cuts discussed in Section 3.1, the J/ψ mass cut, and the loss of luminosity in the Dimuon_5_V2 trigger due to hardware problems. The efficiency for a muon to match a CTC track to within 3 σ, where σ is the expected scattering spread due to multiple scattering, was measured in Reference [41] to be 0.967 ± 0.007. The J/ψ signal observed in the data was defined by a ± 66 MeV/c² cut on the J/ψ mass. This was approximately $\pm 3\sigma$ where σ was the measured J/ψ width. The efficiency of this cut was estimated from the observed J/ψ mass distribution in the data to
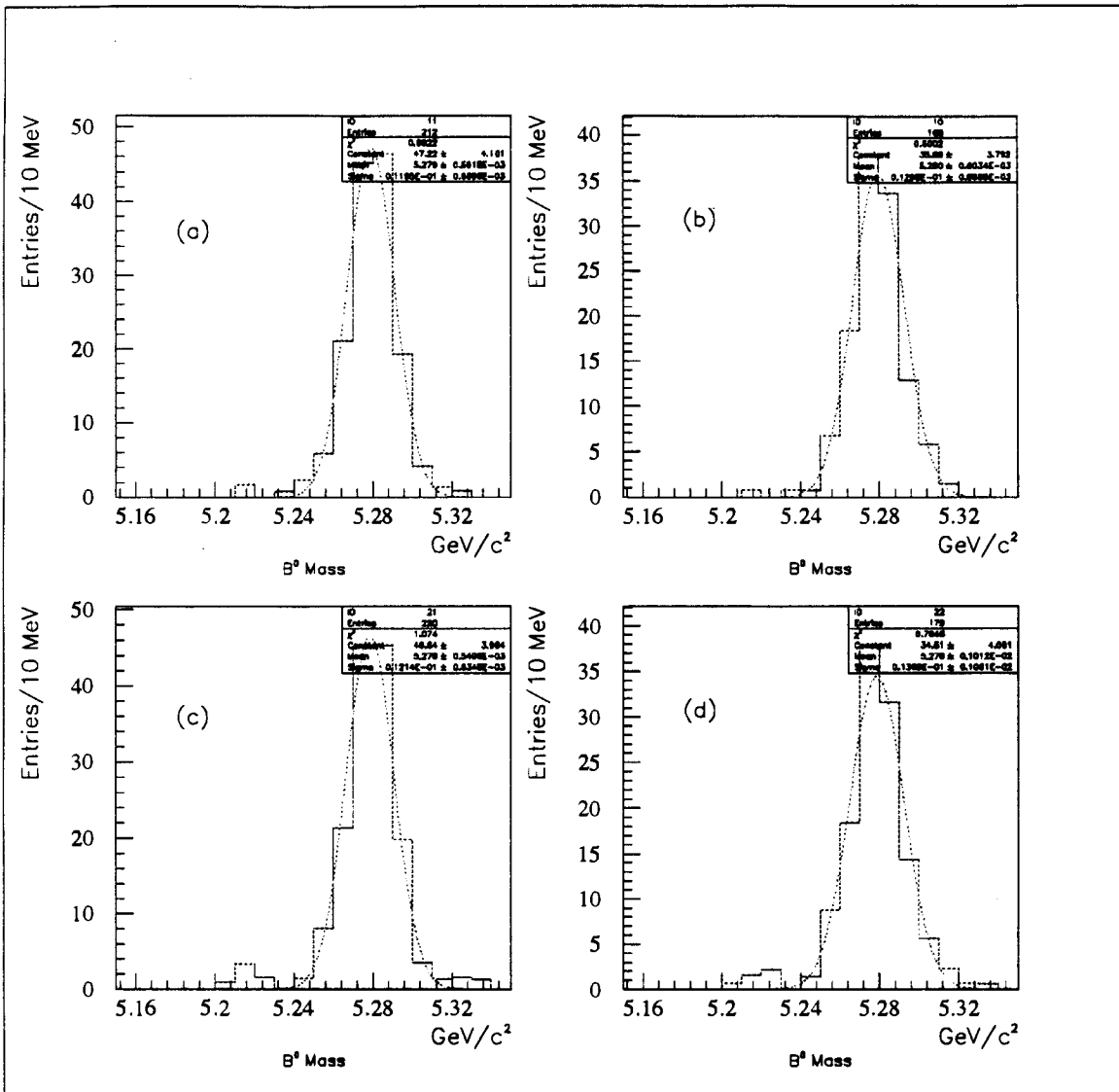
Figure 4.28: Reconstructed B^0 mass from simulated data using the Dimuon_5_V2 trigger. Figure (a) includes only those events with the correct $K\pi$ mass assignments and used the Dimuon_5_V2 trigger. Figure (b) is the same as (a), but used the Dimuon_3_3 trigger. Figures (c) and (d) are the same as (a) and (b), respectively, but contain a contribution where the K and π have had their masses misassigned. When both mass combinations contributed a B^0 candidate, the combination with the mass closer to the K^{0*} mass was used.

be 0.99 ± 0.01. As discussed in Section 3.1, hardware problems with the trigger apparatus, during the portion of the run with the Dimuon_5_V2 trigger in operation, resulted in a loss of approximately 14% of produced J/ψ 's.

The track finding efficiency for the muons was also measured in Reference [41] and found to be 0.97 ± 0.02. In the same study, the tracking efficiency for charged tracks was examined by embedding Monte Carlo events in real J/ψ data and found to be 0.94 ± 0.04 [41], where the error has been elarged by a factor of two to reflect the different kinematics of the particles studied in that analysis.

The total efficiency for reconstruction of B^0 mesons was calculated in two steps. In the first step, the ratio N_{recon}/N_{prod} was calculated, where N_{recon} is the number of B^0's reconstructed from the simulated data sample. For the b quark efficiency, N_{prod} represents the number of b quarks with $P_T > 11.5$ GeV/c and $|y| < 1$, while for the B^0 efficiency, N_{prod} represents the number of B^0's with $P_T > 9$ GeV/c and $|y| < 1$. The ratio N_{recon}/N_{prod} reflects the efficiencies of the triggers, including the P_T cuts on the muons, the different P_T cuts on the K and π mesons, the mass cut for the K^{0*} , and the effect of the procedure for removal of double-counting. The simulated data sample was based on 90,000 b quarks generated with P_T (b)>6.0 GeV/c. For the b quark acceptance, N_{prod} was the number of events with a P_T (b) > 11.5 GeV/c and $|y| < 1$. This was 11194 events. The number of B^0's reconstructed was $N_{recon} = 263$ in the Dimuon_5_V2 trigger and 210 in the Dimuon_3_3 trigger, resulting in b quark efficiencies of $N_{recon}/N_{prod} = 0.0235 \pm 0.0014$ and 0.0187 ± 0.0013. The efficiency for B^0 mesons with $P_T > 9$ GeV/c and $|y| < 1$ was calculated in a similar way and found to be 0.0205 ± 0.0020 and 0.0143 ± 0.0017 for the Dimuon_5_V2 and Dimuon_3_3 triggers respectively.

The efficiencies of the pattern recognition, muon matching cuts, J/ψ mass window, and hardware losses were then included by multiplication with N_{recon}/N_{prod}. Tables 4.3 and 4.4

show the breakdown of the individual contributions to the efficiencies. The total efficiencies

for reconstructing B^0 mesons in the decay channel

$b \rightarrow B^0 \rightarrow J/\psi \ K^{0*}, K^{0*} \rightarrow K\pi, J/\psi \rightarrow \mu\mu$, with $P_T(b) > 11.5$ GeV/c, $|y| < 1.0$ was

determined to be:

- $(1.43^{+0.23}_{-0.35})\%$ for the Dimuon_3_3 trigger,

and

- $(1.55^{+0.34}_{-0.45})\%$ for the Dimuon_5_V2 trigger.

while the total efficiencies for the process $B^0 \rightarrow J/\psi \ K^{0*}, K^{0*} \rightarrow K\pi, J/\psi \rightarrow \mu\mu$, with

$P_T(B^0) > 9.0$ GeV/c, $|y| < 1.0$ was determined to be:

- $(1.09^{+0.20}_{-0.29})\%$ for the Dimuon_3_3 trigger,

and

- $(1.37^{+0.30}_{-0.40})\%$ for the Dimuon_5_V2 trigger.

Note that the errors cited for the ratio N_{recon}/N_{prod} included variations of the trigger

efficiency and variations due to the unknown J/ψ -K^{0*} polarization. The error in the

tracking efficiency included an uncertainty for K mesons which decayed prior to leaving the

CTC. The Monte Carlo predicted that approximately 8% of K's decayed inside the CTC.

The reconstruction algorithm correctly found B^0 mesons for about 50% of these events,

resulting in an inefficiency of 4%. The acceptance was obtained by assuming the simulation

correctly treated these decays and assigning a systematic error of $\pm 4\%$.

Final Algorithm and Efficiency

In summary, the prescription for finding the B^0 mesons in the data was:

	Dimuon_3_3 Trigger	Dimuon_5_V2 Trigger
N_{recon}/N_{prod}	$0.0187^{+0.0030}_{-0.0046}$	$0.0235^{+0.0047}_{-0.0066}$
J/ψ Mass Cut	0.98 ± 0.02	0.98 ± 0.02
Muon Matching Cuts	0.94 ± 0.01	0.94 ± 0.01
Tracking Efficiency	0.83 ± 0.08	0.83 ± 0.08
Hardware Losses	1.00	0.86 ± 0.06
Total	$0.0143^{+0.0023}_{-0.0035}$	$0.0155^{+0.0034}_{-0.0045}$

Table 4.3: Breakdown of efficiencies for identifiying b quarks with $P_T > 11.5$ GeV/c and $|y| < 1.0$.

	Dimuon_3_3 Trigger	Dimuon_5_V2 Trigger
N_{recon}/N_{prod}	$0.0143^{+0.0022}_{-0.0036}$	$0.0209^{+0.0042}_{-0.0059}$
J/ψ Mass Cut	0.98 ± 0.02	0.98 ± 0.02
Muon Matching Cuts	0.94 ± 0.01	0.94 ± 0.01
Tracking Efficiency	0.83 ± 0.08	0.83 ± 0.08
Hardware Losses	1.00	0.86 ± 0.06
Total	$0.0109^{+0.020}_{-0.029}$	$0.0137^{+0.0030}_{-0.0040}$

Table 4.4: Breakdown of efficiencies for identifiying B^0's with $P_T > 9.0$ GeV/c and $|y| < 1.0$.

1. Require an event to have passed either the Dimuon_3_3 or Dimuon_5_V2 triggers.

2. Identify J/ψ candidates

   - Require that the two muon candidates have a vertex constrained invariant mass between 3.0309 and 3.1629 GeV/c^2.

   - If the event passed the Dimuon_5_V2 trigger, the stiff muon was required to be a gold muon. The gold muon was required to have P$_T$ above 5 GeV/c. The softer muon was required to have P$_T$ above 2 GeV/c.

   - If the event passed the Dimuon_3_3 trigger, both muons were required to be gold muons and to have P$_T$ greater than 3 GeV/c.

   - The muons were required to pass the trigger wedge separation requirements.

3. The invariant mass of all other pairs of oppositely charged tracks (excluding the muon pair) was formed.

   - The invariant mass was calculated assuming one track to be a charged pion and the other to be a charged kaon. A second combination with the mass assignments reversed was also formed.

   - Candidate K^{0*} mesons were required to have a K with P$_T$ above 1.0 GeV/c and a π with P$_T$ above 0.5 GeV/c.

   - Invariant mass combinations which were within 50 MeV/c^2 of the mean K^{0*} mass were defined to be K^{0*} candidates.

   - The pion and kaon were required to have been well measured tracks and to have been associated with the same vertex as that of the candidate J/ψ .

4. The invariant mass combination of the K^{0*} and J/ψ candidates was formed to obtain B^0 candidates.

5. If a B^0 candidate used the same pair of tracks twice in the K^{0*} candidate, only the K^{0*} with mass closer to the mean K^{0*} mass was kept. This occured for approximately 20 % of all B^0 candidates.

6. The P_T of the B^0 meson was required to be larger than 9 GeV/c.

With the above prescription for finding B^0 mesons, the data was then examined to determine the number of mesons observed. This is the subject of the next section.

4.3   Data

4.3.1 J/ψ Reconstruction

The observation of J/ψ 's in the data was accomplished by looking for pairs of oppositely charged muons. Figure 4.29 shows the invariant mass spectrum for all muon pairs reconstructed in the data. The muons were required to pass a 3 σ matching cut between the stub and CTC track, where σ was the standard deviation of the mismatch expected due to Multiple Coulomb Scattering. The muons were required to have a P_T of at least 2.0 GeV/c and each muon pair was subjected to a common vertex constraint.

A prominent peak is seen in Figure 4.29 at the J/ψ mass, as well as a smaller peak at the ψ' mass. The shoulder at 2.5 GeV/c² was an aritifact of the criteria used in the formation of the data set which was consisted of all events with at least one oppositely signed muon pair with invariant mass above 2.5 GeV/c².

Figure 4.30 shows the vertex constrained muon pair invariant mass in the immediate vicinity of the J/ψ mass. A fit to a Gaussian plus a flat background resulted in a measured width of about 23.1 GeV/c² and a mean of $3.0943 \pm .0004$ GeV/c². The latter was significantly lower than the World Average mass of 3.0959 GeV/c². This was probably due to the

choice of a Gaussian fit the signal. The fit in data exhibited an asymmetry about the J/ψ mass suspected to be due to initial state radiation.

The fit in Figure 4.30 indicated that there were approximately 2700 J/ψ 's included within the Gaussian distribution. The signal region for candidate J/ψ 's was defined to be those events within ± 3 σ of the world average mass, where σ was the measured width (23.1 GeV/c^2). These candidates were combined with the candidate K^{0*} in order to identify B candidates as is discussed in the next section.

4.3.2 K^{0*} Selection

The next step was to select K^{0*} candidates. For each event containing a candidate J/ψ oppositely signed tracks were combined assuming one track was a K ($m_K = 493.646$ MeV/c^2 [52]) and the other a π ($m_\pi = 139.5679$ MeV/c^2 [53]). The track designated a K was required to have P$_T$ above 1 GeV/c and the other track was required to have a P$_T$ above 500 MeV/c. The tracks associated with the muons forming the J/ψ candidate were excluded from consideration. Figure 4.31 shows the invariant mass distribution of the tracks employed to identify K^{0*} candidates. There is no significant evidence of a peak above the combinatoric background at the K^{0*} mass of 0.896 GeV/c^2. As indicated in Section 4.2, K^{0*} candidates were selected from those track combinations having an invariant mass between 0.846 and 0.946 GeV/c^2.

Identification of B^0 Candidates

B^0 candidates were selected by refitting the tracks in J/ψ - K^{0*} events. The four tracks corresponding to the candidate J/ψ -K^{0*} were refit with a common vertex constraint and simultaneously requiring the muon pair to have a mass of exactly 3.0969 GeV/c^2. Figure 4.32 shows the $K\pi\mu\mu$ mass distribution after refitting the tracks. The muons used in the figure
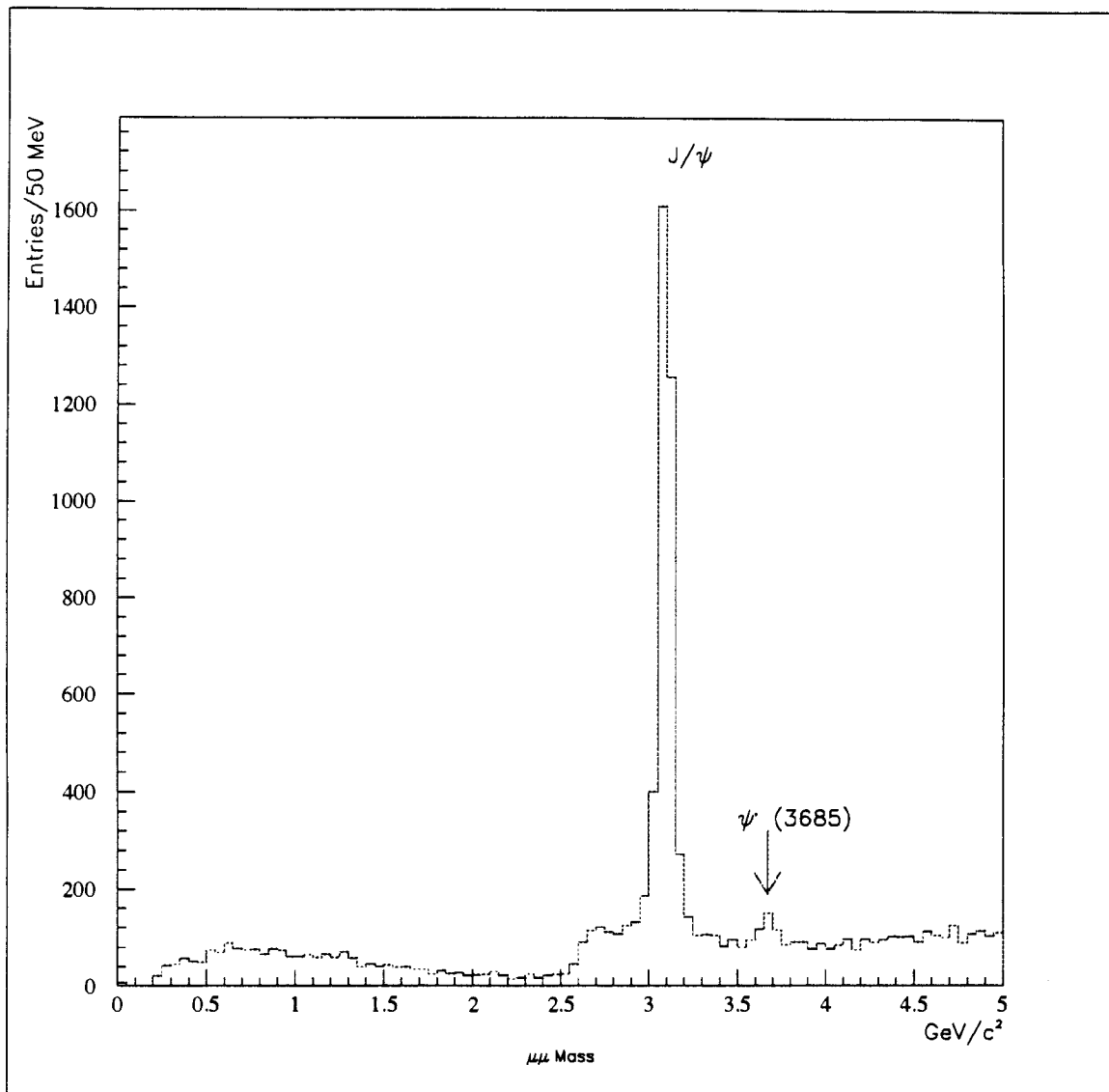
Figure 4.29: Invariant mass distribution of $\mu\mu$ pairs in the $\bar{p}p$ data. The shoulder at 2.5 GeV/c^2 was a requirement used in the formation of the data sample.
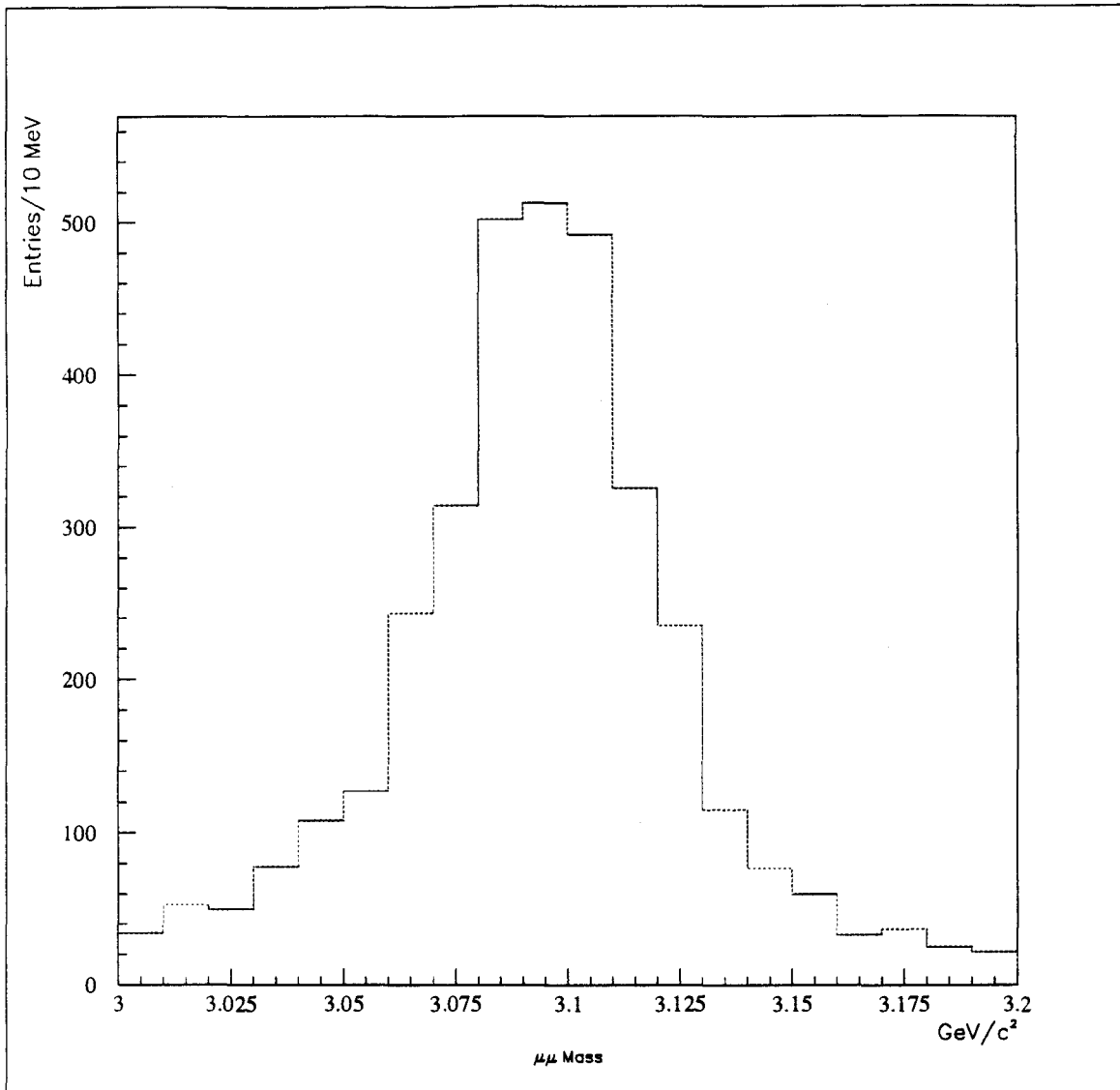
Figure 4.30: Invariant mass distribution of $\mu\mu$ pairs in the $\bar{p}p$ data in the vicinity of the J/ψ peak. A fit to a flat background and Gaussian signal indicated a width of 23.1 GeV/c², a mean of 3.0943 ± .0004 GeV/c² and a total of approximately 2700 J/ψ 's.
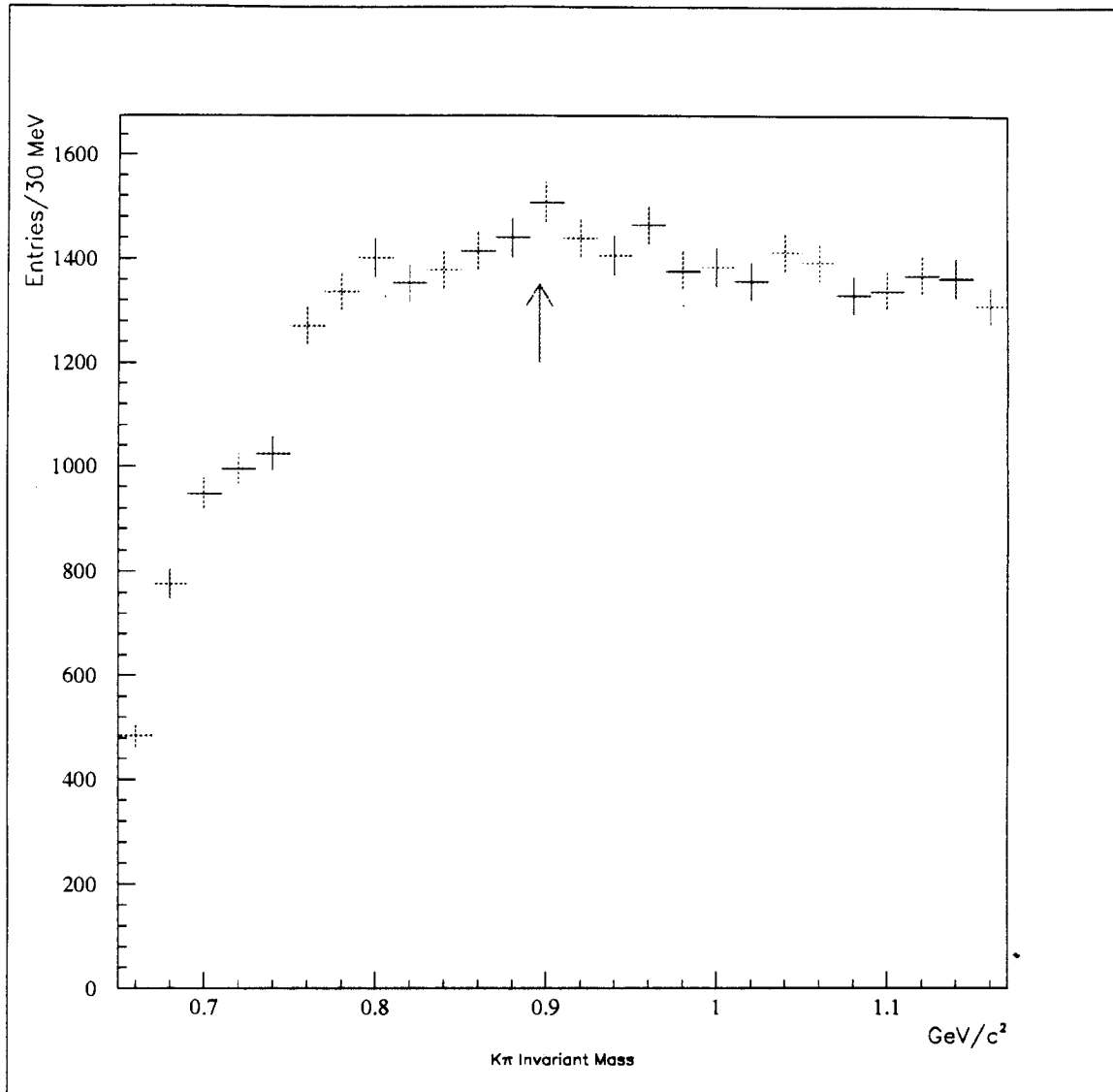
Figure 4.31: Invariant mass distribution of track pairs with $K\pi$ and πK mass hypothesis. Candidate K^{0*} mesons were selected from the region within 50.0 MeV/c^2 of the K^{0*} mass (m(K^{0*})=0.896 GeV/c^2).

were required only to have had a P_T above 2.0 GeV/c and were not required to have specifically passed one of the dimuon triggers. The K and π mesons were required to have satisfied the respective cuts of 1.0 and 0.5 GeV/c.

An excess of events can be seen near the B^0 mass. The distribution was fit to a background function and a Gaussian signal constrained to have a width of 14 MeV/c^2. The fit indicated an excess of 11.4 ± 4.9 events above background at a mass of $5.292 \pm .008$ GeV/c^2. The signal is approximately 2.7 σ above background. A fit to the same data with no constraint on the width of the signal yielded 11.4 ± 5.6 events and a width of 13.9 ± 7.6 MeV/c^2.

Taking the excess of events to be clear evidence of a B^0 signal, the cuts of Section 4.2 were applied in order to obtain the final number of events to be used in the calculation of the b quark and B^0 cross sections.

Figure 4.33 shows the J/ψ -K^{0*} mass distribution after first sorting the signal according to which dimuon trigger was satisfied. The luminosities taken with each trigger were comparable so that dividing the B^0 sample according to which trigger was operating significantly lowered the significance of the signal, especially on the Dimuon_3_3 trigger.

After applying all of the cuts, the distributions of Figure 4.34 were obtained. A signal iss still observed in the sample with the Dimuon_5_V2 trigger requirement, while little remained of the signal on the Dimuon_3_3 trigger. In addition to the trigger selection, the final distributions include cuts on the P_T of the muons and the requirement of at most one B^0 candidate per K^{0*} candidate. Candidates which used the same two tracks for both the K and π candidates were only counted once, using the procedure discussed in Section 4.2 for the removal of double-counted events.

Because of the low number of events passing the cuts, the number of events observed was measured using a Maximum Likelihood technique which incorporated the measured mass resolution discussed in Section 4.2. The likelihood function assumed that the number of
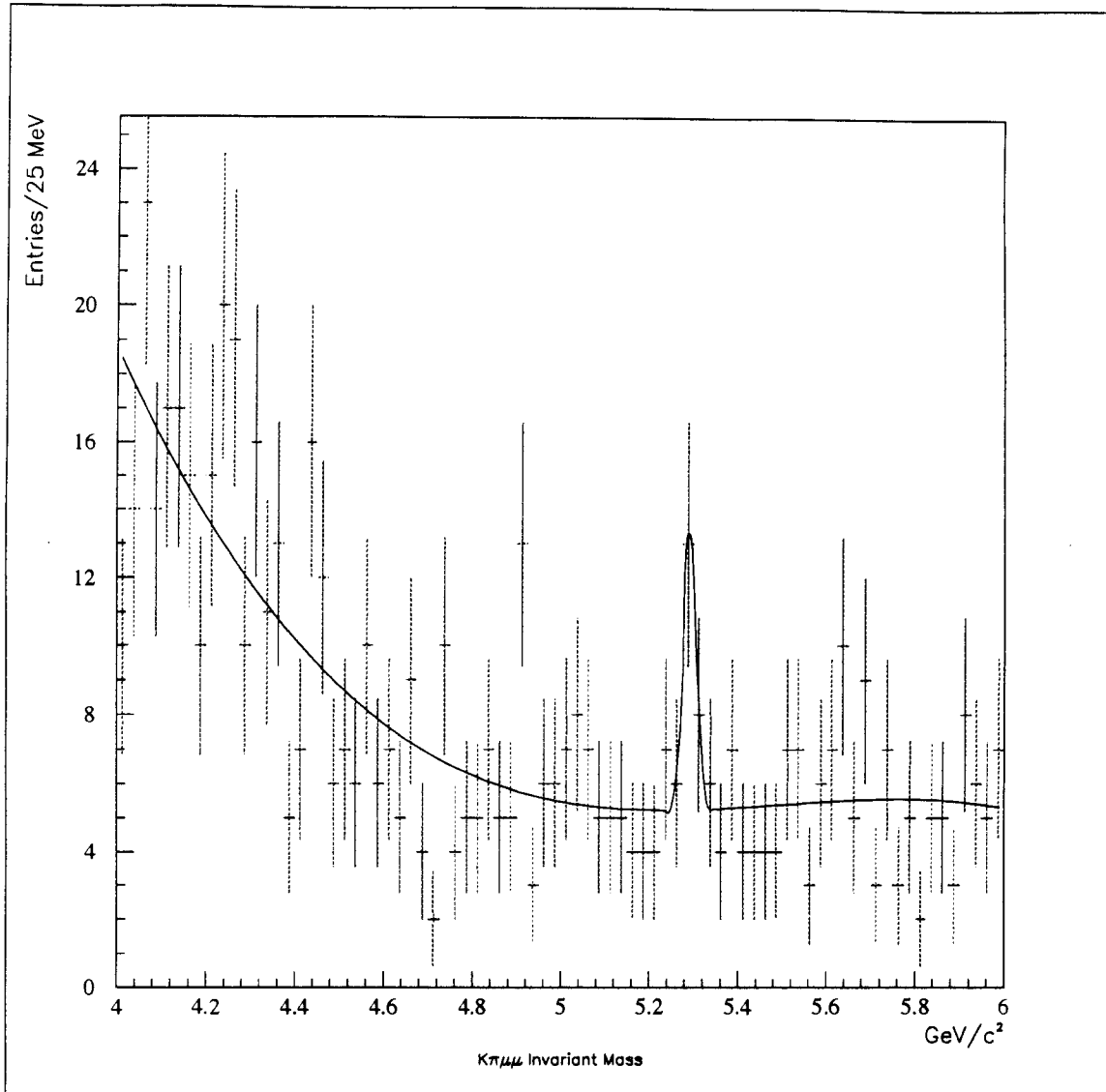
Figure 4.32: Invariant mass distribution of K^{0*} -J/ψ events. No trigger selection was required and the muons were required to have P_T above 2.0 GeV/c. The P_T cuts of 1.0 and 0.5 GeV/c were also placed on the K and π mesons.
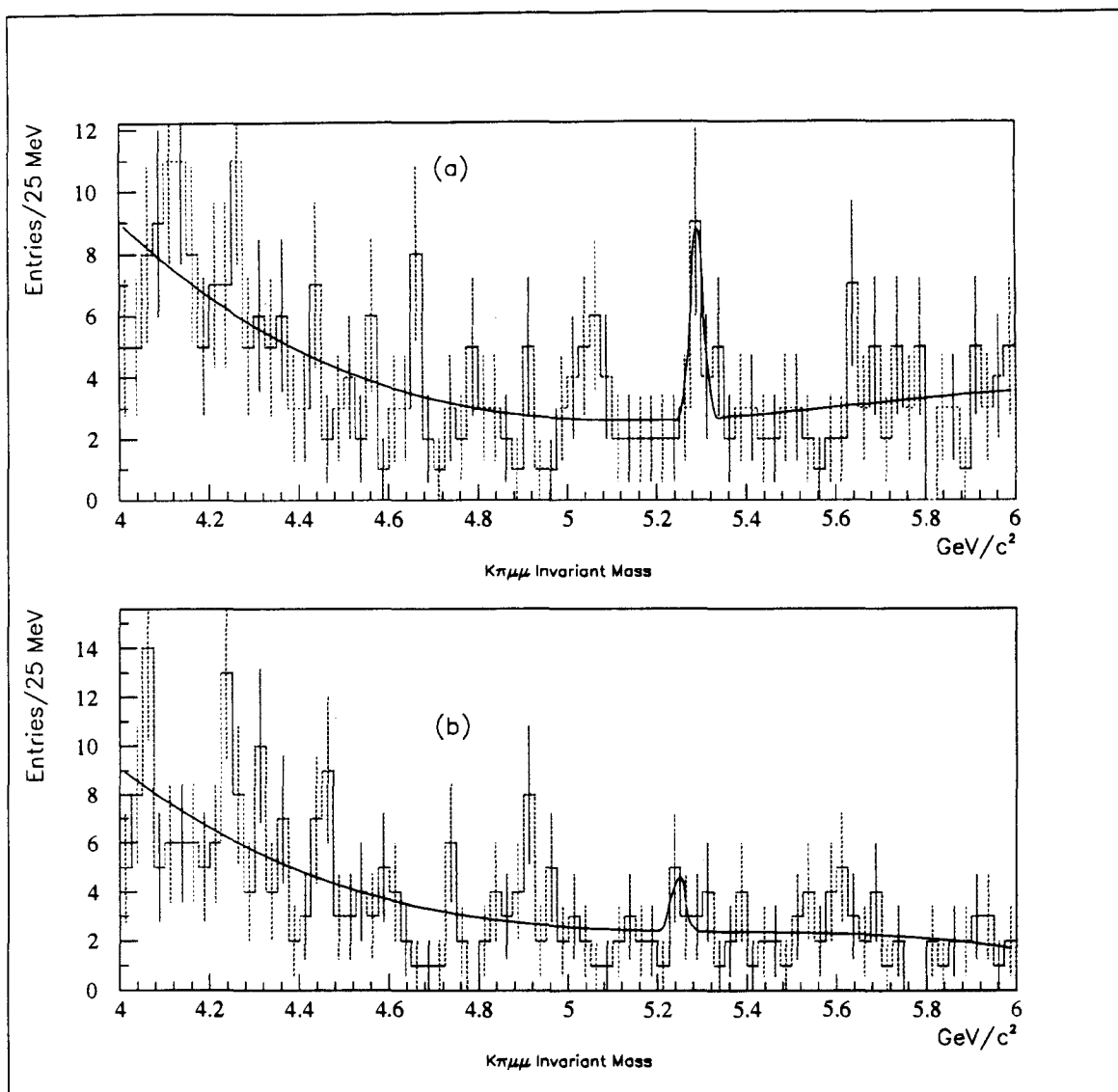
Figure 4.33: B^0 candidate invariant mass distributions after sorting according to the trigger satisfied. Figure (a) shows the distribution for events recorded with the Dimuon_5_V2 trigger. Figure (b) shows the distribution for events obtained with the Dimuon_3_3 trigger. The events in both samples required muons with P_T above 2 GeV/c, K P_T above 1.0 GeV/c, and a $K\pi$ mass between 0.846 and 0.946 GeV/c^2. The background function was a third order polynomial. The signal was taken to be a Gaussian with a fixed width of 14 MeV/c^2, the estimated mass resolution.
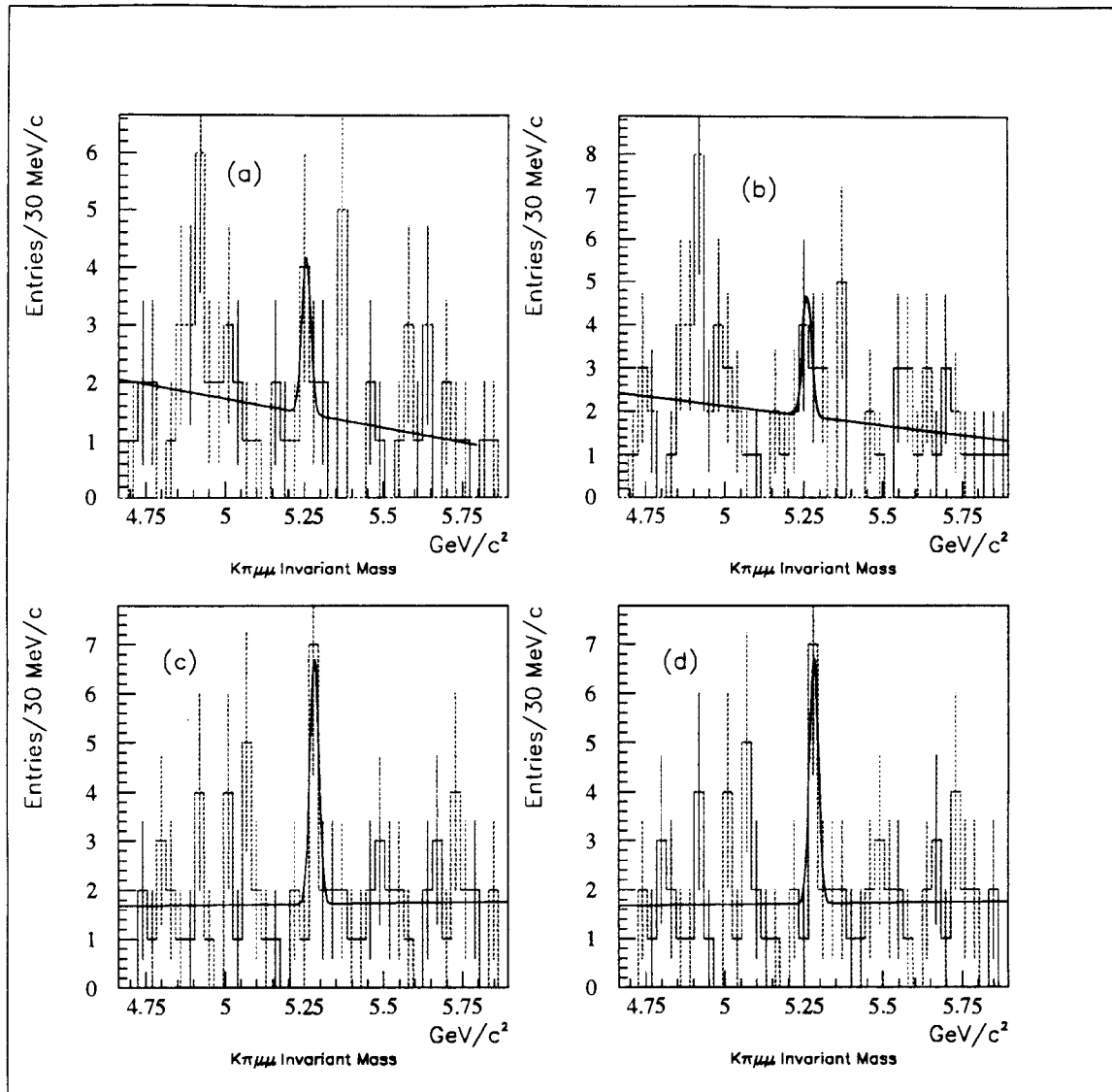
Figure 4.34: $K\pi\mu\mu$ invariant mass distributions. Figure (a) shows the distribution on the Dimuon_3_3 trigger with a cut of 9.0 GeV/c on the B^0 P_T . Figure (b) is the same distribution without the cut on the B^0 P_T . Figures (c) and (d) are the same as (a) and (b), but with the Dimuon_5_V2 trigger. Fits to a linear background and Gaussians signals resulted in 3.2 ± 2.5, 3.3 ± 2.8, 5.8 ± 2.9, and 5.8 ± 2.9 events for plots (a) to (d) respectively.

events observed was distributed with a Poisson probability distribution in a mass region corresponding to $\pm 3\ \sigma$ where σ was the mass resolution.

The mass resolution for J/ψ events was observed to be approximately 20 % larger in real data than in the Monte Carlo . It was assumed that a similar discrepancy could exist in the resolution of the B^0 . Therefore, a 20 % systematic uncertainty in the number of B^0 events observed was assigned due to this possible uncertainty in the mass resolution.

The above results give 5.8 ± 2.9 events in the Dimuon_5_V2 trigger and 3.3 ± 2.8 events in the Dimuon_3_3 trigger samples. The B^0 cross section included a cut on the B^0 P_T of 9.0 GeV/c. With this cut, the number of events estimated on the Dimuon_3_3 trigger was 3.2 ± 2.5. No events were lost with this cut on the Dimuon_5_V2 trigger, and the number of observed events was 5.8 ± 2.9. These values were used to estimate the cross sections for b quark and B^0 production as is discussed in the next section.

4.4 b Quark and B^0 Cross Sections

Equation 4.1 was applied to the results from Sections 4.3.2 and 4.2 to arrive at the cross section measurements for each channel separately. Table 4.4 shows the breakdown of the different components that were used in the calculation of the cross sections. The errors quoted for the cross section are the statistical and systematic errors respectively and the systematic errors are divided respectively into the contributions which were correlated and uncorrelated between the triggers, respectively. The systematic errors are given in Table 4.4.

Trigger	Dimuon_5_V2		Dimuon_2_2	
	b quark	B^0	*b* quark	B^0
Acceptance	$1.55^{+0.35}_{-0.45}$ %	$1.37^{0.31}_{-0.40}$ %	$1.43^{+0.25}_{-0.35}$ %	$1.09^{+0.21}_{-0.29}$ %
Luminosity (pb^{-1})	1.7 ± 0.1	1.7 ± 0.1	2.6 ± 0.2	2.6 ± 0.2
Number of Events	$5.8 \pm 2.9 \pm 1.2$	5.8 ± 2.9	$3.3 \pm 2.5 \pm 0.7$	$3.3 \pm 2.5 \pm 0.6$
Branching Ratio	$(1.9 \pm 0.56) \times 10^{-5}$	$(5.1 \pm 1.5) \times 10^{-5}$	$(1.9 \pm 0.56) \times 10^{-5}$	$(5.1 \pm 1.5) \times 10^{-5}$
$P_T{}^{MIN}$	11.5	9.0	11.5	9.0
$\sigma(P_T > P_T{}^{MIN}, |y| < 1.0 \ (\mu b))$	$5.8 \pm 2.9^{+2.2}_{-2.5} \pm 1.1$	$2.4 \pm 1.3^{+0.9+0.5}_{-1.0-0.5}$	$2.3 \pm 1.9^{+0.9}_{-1.0} \pm 0.3$	$1.1 \pm 0.6^{+0.4+0.1}_{-0.5-0.1}$

Table 4.5: Summary of quantities used in measurement of *b* and B^0 cross sections.

Source	Dimuon_5_V2 Trigger	Dimuon_3_3 Trigger	Correlated ?
Trigger	18	12	N
Branching Fraction	30	30	Y
B^0 Mass Resolution	20	20	Y
Polarisation	+0 −20	+0 −20	Y
Tracking	7	7	Y
Luminosity	6.6	6.6	Y
Hardware Problems	6.0	0.0	N
Fragmentation	+6.0 −3.0	+6.0 −3.0	Y
Decay in Flight	4.0	4.0	Y
Muon Matching	1.0	1.0	Y
J/ψ Mass window	2.0	2.0	Y
Total of Correlated Errors	+38% −42%	+38% −42%	
Total of Uncorrelated Errors	±19%	±12%	

Table 4.6: Summary of systematic errors in the b cross section.

For each trigger, the correlated and uncorrelated errors were added in quadrature.

The measurements of the cross sections using the two trigger channels were combined to arrive at the best estimate of the b quark cross section. The method for combining the two measurements was based on the assumption that the number of events produced in the respective luminosities for each channel were distributed according to Poisson distributions. For each channel, the Poisson parameter, μ, represented the average number of events produced in the particular luminosity interval. This means, for instance, that if the measurement of the number of events identified with the Dimuon_3_3 trigger in 2.6 pb^{-1} was repeated many times, one would expect to observe an average of μ events. The Poisson probabilities for the measured number of events in the Dimuon_3_3 and Dimuon_5_V2 triggers, respectively, were parameterized by μ_{33} and μ_{52} respectively. These were related to one another by

$$\mu_{33} = \frac{\mathcal{L}_{33}}{\mathcal{L}_{52}}\mu_{52}, \tag{4.10}$$

where $\mathcal{L}_{33}$ and $\mathcal{L}_{52}$ were the integrated luminosities for each channel. The observed number of events in each channel was related to the number produced via the relevant efficiency. The convolution of an efficiency with a Poisson process is known to be equivalent to a Poisson distribution with the parameter $\epsilon \times \mu$ [54] where ϵ is the efficiency. This assumes that the number of events observed was related to the number produced by a binomial probability distribution with the success probability ϵ. The efficiencies for each channel were denoted by ϵ_{33} and ϵ_{52}. Since the number of events observed on each channel was assumed to a Poisson process, a Likelihood function was written in terms of the number observed on each channel:

$$L = (\frac{e^{\epsilon_{33}\mu_{33}}(\epsilon_{33}\mu_{33})^{N_{33}}}{N_{33}!})(\frac{e^{\epsilon_{52}\mu_{52}}(\epsilon_{52}\mu_{52})^{N_{52}}}{N_{52}!}). \tag{4.11}$$

The Likelihood function in Equation 4.11 was combined with Equation 4.10 and the loga-

rithm was minimized with respect to μ_{33} to determine the best estimator of the parameter $\epsilon_{33}\mu_{33}$. The result was

$$\overline{\epsilon_{33}\mu_{33}} = \frac{N_{33} + N_{52}}{1 + R},\tag{4.12}$$

where

$$R = \frac{\epsilon_{52}\mathcal{L}_{52}}{\epsilon_{33}\mathcal{L}_{33}}.\tag{4.13}$$

This method of averaging the two measurements gave an estimated number of events per 2.6 pb^{-1} with the Dimuon_3_3 trigger, and without the rapidity and P_T cuts on the B^0 , of 5.3 ± 1.8 events and a cross section of 3.8 ± 1.2 μb. Including the 9 GeV/c cut on the B^0 meson P_T and the rapidity cut $|y(B^0)| < 1$, the number of events was 5.0 ± 1.6. Note that the two measurements could have been combined to estimate μ_{52} rather than μ_{33}. Both procedures must and do give the same cross section.

Each channel had systematic uncertainties as well. These have already been discussed individually in previous sections. Table 4.4 summarizes the systematic uncertainties for each trigger and whether the systematic was correlated between the two channels. Separately combining the correlated and uncorrelated errors, the final result for the average b quark cross section was 3.8 ± 1.2$^{+1.7}_{-1.8}$ μb. The errors reflect the statistical and systematic uncertainties respectively. The uncorrelated errors from each trigger were added in quadrature, while the correlated errors were included once only. For the B^0 , the resulting cross section was 1.7 ± 0.6 ± 0.8 μb. Finally, the measured b quark and B^0 production cross sections in $\bar{p}p$ collisions at a center of mass energy of 1.8 TeV were

- $\sigma(P_T(b) > 11.5 \text{ GeV/c}, |y| < 1.0) = 3.8 \pm 1.2^{+1.7}_{-1.8}$ μb

and

- $\sigma(\mathrm{P}_T(B^0) > 9.0 \text{ GeV/c}, |y| < 1.0) = 1.7 \pm 0.6 \pm 0.8 \ \mu\text{b}.$

Chapter 5

Conclusion

The result for the b quark cross section is shown in Figure 5.1 with the predictions of the NDE analysis and with the other measurements made at CDF during the 1988-1989 Collider run [32]. As in other measurements of the b cross section at CDF [32], the measurement reported in this analysis was above the value predicted by the NDE analysis. The discrepancy in this particular measurement was approximately 1.4 standard deviations above the predicted value.

A particularly important implication of the result obtained in this analysis was the added evidence that the theoretical predictions did not yet accurately predict the b quark production cross section. Without this result, the previous CDF results were subject to two criticisms. First, the measurements obtained from the study of inclusive electron production were correlated. This meant that if a systematic effect, such as the branching ratio for the process $B^0 \rightarrow eX$, was incorrect then all three measured values of the cross section would be simultaneously offset from the correct value by the same amount. This criticism also applies, to a lesser extent, to the measurement made from an analysis of $e^- D^0$ production

where many of the systematics associated with electron identification were common with those for the inclusive electron analysis.

A second criticism concerned the cross section measurement made from exclusive reconstructions of $B^{\pm}$ mesons via the decay $B^{\pm} \rightarrow J/\psi K^{\pm}$. That analysis was based on a sample of approximately 14 events and obtained a cross section measurement which was approximately 2.5 standard deviations above the predicted value. The substantial ($\sim 50\%$) statistical and systematic errors associated with that analysis made it difficult to draw conclusions concerning the accuracy of the predicted cross section. The result presented in this analysis has provided a third independent measurement of the b quark cross section that exceeded the predicted values by a significant amount. With this analysis, the three independent analyses at 1.8 TeV all show a higher value of the cross section than was predicted using the next-to-leading order calculations.

As discussed in Chapter 2, there were a number of sources of uncertainty in the theoretical predictions. The procedure for estimating the effect of these uncertainties is unspecified. However, two of the sources–the b mass and Λ_{QCD}–have some basis in experimental measurements. The b mass can be justified on the basis of the mass of Υ or B mesons, while Λ_{QCD} is an experimentally measured quantity.

On the other hand, the gluon distribution functions and the effect of yet higher order contributions to the cross section are less well known. The effect of the higher order contributions were estimated by varying the value of the renormalization parameter μ. The actual amount by which it should be varied to estimate these effects could be justifiably questioned, and therefore, the effect of higher order terms may be important.

The gluon distribution function is also a potential source of discrepancy. This has not been well measured over the range of x relevant to to b production at Tevatron energies. A recent analysis by Berger,Meng, and Tung [55] has demonstrated that by assuming the
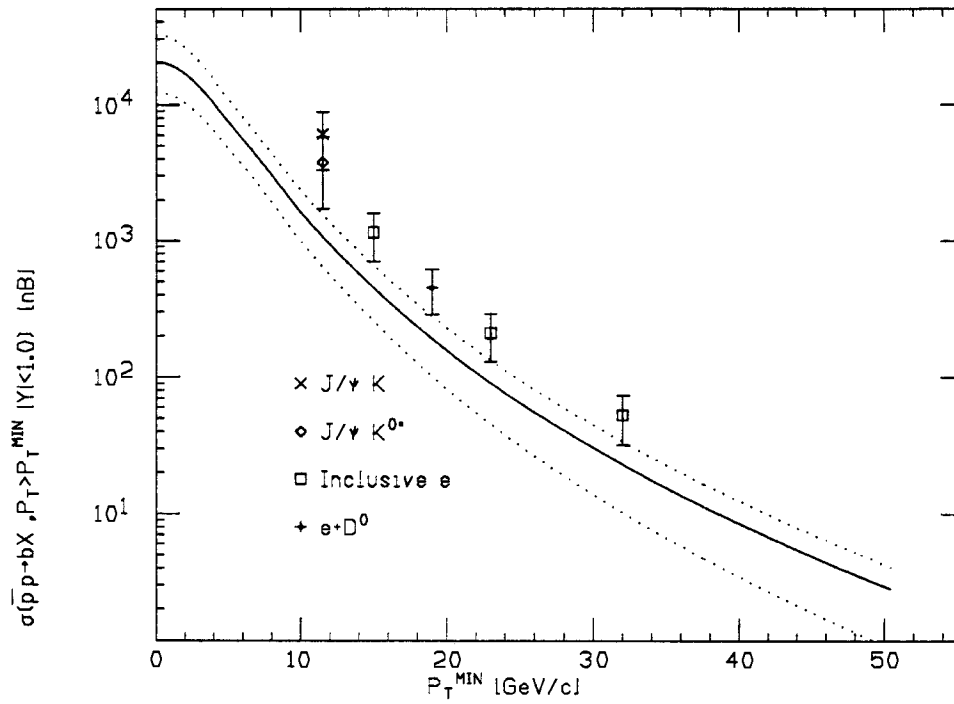
Figure 5.1: Measurements of the *b* quark cross section at CDF. The curves are the NDE predicted value and the estimated theoretical uncertainty. The errors shown add all systematic and statistical uncertainties in quadrature.

$\mathcal{O}(\alpha_S{}^3)$ calculations to be correct, the CDF and UA1 measurements of the b quark cross sections can be combined with known results from Deep Inelastic Scattering to yield gluon distribution functions which differ somewhat from previous models. In particular, the data would require a larger contribution from gluons in presently unmeasured regions of x. Not surprisingly, this distribution function is able to provide an adequate description of the measured CDF b quark cross section. In the near future, precision measurements of the gluon structure function will be made using ep collisions at the ZEUS and H1 experiments [56]. These measurements will give a better understanding of what the measured b cross sections imply for our understanding of heavy quark production.

For the present, it is clear from the measured b quark cross section that perturbative QCD is able to provide a rough numerical estimate of heavy quark production rates, but has not yet demonstrated a capability to do so with precision. The implications of this conclusion include the possibility that in production rates for top quarks may also be underestimated and that present limits on its mass are too conservative. As was discussed in Chapter 2, the theoretical uncertainties in the calculated rates for top production are expected to be much more reliable. Until the top quark itself is found, this expectation remains a speculation which is not yet supported by any experimental evidence.

Appendix A

Multiple Coulomb Scattering of

Muons

In order to identify central muons at CDF, a match was required between charged tracks in the CTC and stubs in the CMU. Between the two subsystems was over eight feet of steel, lead, and scintillator. Muons with momenta above a few hundred MeV/c suffered energy losses due to ionization at less than a few MeV/g/cm^2 and were therefore minimum ionizing. Because of this, muons detected by the Central Muon chambers at CDF typically passed through the calorimetry maintaining the flight direction they had on entering the calorimetry. However, because they were subject to Multiple Coulomb Scattering (MCS) , there was often significant (on the order of a few centimeters) separation between an extrapolated CTC track position at the muon chambers and the position of a muon stub. A natural way to parameterize the mismatch, which takes into account MCS, was to measure the difference between the extrapolated track position and stub in units of the expected differences due to MCS.

After passing through L/L_R radiation lengths of material, a minimum ionizing particle is deflected by an angular amount, ϕ, from its incident direction where the distribution of ϕ is approximately Gaussian with a standard deviation of [57]:

$$\sigma_\phi = \frac{13.6\text{MeV/c}}{\beta p} Z_{inc} \sqrt{L/L_R}(1 + 0.038 ln(L/L_R)) \text{ (radians)}. \qquad (A.1)$$

Note that ϕ is the 3 dimensional angle relative to the muon flight direction. Taking into account energy losses, this expression was employed to calculate the standard deviations in the x-y and z-y planes of the CDF detector. The variances were given by:

$$\sigma_x^2 = (\frac{13.8cm}{P_T})^2 \frac{0.59 + 0.41/sin\theta}{1.0 - 0.71/P_T} + (0.3 \text{ cm})^2 \qquad (A.2)$$

$$\sigma_z^2 = (\frac{13.8cm}{P_T})^2 \frac{0.59 + 0.41/sin\theta}{1.0 - 0.71/P_T} \frac{1}{(sin\theta)^2} + (1.5 \text{ cm})^2. \qquad (A.3)$$

In addition to the error from MCS, a measurement error also contributed to the expected width of these distributions. This quantity was estimated using muons with large P_T (30-40 GeV/c) so that the average scatter from MCS was small. The study showed additional contributions of 0.3 cm in the x-y plane and 1.5 cm z-y plane. The expected standard deviation was taken to be that due to MCS added in quadrature with these measurement errors.

Studies of the matching distributions at CDF showed that the x distributions contained a systematic offset which was sign-dependent and had an average value of 2.9/P_T $(GeV/c)\times$ sign(μ) (cm). The track-stub mismatch was therefore corrected by this amount before scaling by the expected MCS standard deviation.

Using this methodology, muon candidates were required to have a track-stub mismatch of less than 3σ, where σ was the standard deviation expected from Equations A.2 and A.3. A study of the matching distributions of cosmic rays in Reference [41] indicated the cut to

be approximately 97.0 ± 0.5 % efficient for muons with P_T above 2 GeV/c.

Appendix B

Track Quality and Vertex

Association Requirements

Tracks used in analyses at CDF were required to have passed a series of cuts designed to ensure that the track parameters were well measured. When tracking efficiencies are quoted in this analysis, they should be understood to represent the fraction of tracks which are not only found, but pass the following requirements:

1. The track had to have been successfully reconstructed in three dimensions and have had at least four stereo hits.

2. The track had to have had at least eight axial hits.

3. At least one half of the hits found by the pattern recognition had to have been used in the fit (true independently for axial and stereo).

4. If fewer than three axial superlayers had five or more hits used in the track fit, then there must have been at least eight hits in the inner four super layers.

5. Either there must have been one axial superlayer with eight hits, or there must have been two consecutive axial superlayers with six hits.

6. The mean axial residual was required to be less than 900 μ.

7. The mean stereo residual was required to be less than 1000 μ.

8. The track had to have at least 50% of the predicted occupancy.

9. Under some circumstances, the track also had to pass a rather complex occupancy requirement; If the track had 50% of the hits it was predicted to have, it was accepted. It could still be accepted if there were at least ten hits in the inner three super layers, at least two axial superlayers with ten or more hits, at least two stereo superlayers with three or more hits, and the mean axial residual was less than 450 μ and the mean stereo residual was less than 500 μ.

In addition to the requiring tracks to have been of good quality, they were also required to have been associated with a primary vertex as located by the VTPC. This requirement helped to remove particles which originated from decays in flight of K and π mesons and tracks which had few hits in the inner layers of the CTC.

Appendix C

Polarization in Decays of $B^0 \rightarrow$ Vector-Vector Decays

Both the J/ψ and K^{0*} mesons are spin-1 particles. In the decay $B^0 \rightarrow J/\psi\, K^{0*}$, depending on the dynamics underlying the decay, these mesons can be polarized relative to their flight direction in the B^0 rest frame. This feature is particularly interesting in that the degree of polarization may allow this mode to be utilized in measurements of CP violation in the b sector [58]. For the purposes of this thesis, however, the effect of this feature was to introduce a systematic uncertainty in the angular distribution of the final state particles. This appendix summarizes an estimate of the size of the uncertainty.

The general form of angular distributions in particle decays can be derived from conservation of angular momentum [59]. For the case of a scalar particle decaying into two vector mesons, the angular distribution is given by:

$$\frac{d^3\Gamma}{\Gamma d\cos\theta_1 d\cos\theta_2 d\phi} = \frac{1}{4}\sin^2\theta_1(1+\cos^2\theta_2)\frac{\Gamma_T}{\Gamma} + \cos^2\theta_1\sin^2\theta_2\frac{\Gamma_L}{\Gamma} -$$

$$\frac{1}{4}sin2\theta_1 sin2\theta_2(\alpha_1 cos\phi - \beta_1 sin\phi) -$$

$$\frac{1}{2}sin^2\theta_1 sin^2\theta_2(\alpha_2 cos2\phi - \beta_2 sin2\phi), \qquad (C.1)$$

where θ_1 and θ_2 are the so called 'Helicity Angles' for the K^{0*} and J/ψ . These are the angles of the final state particles in the parent vector meson's rest frame relative to the parent flight direction in the B^0 rest frame. The angle ϕ is the angular separation between the decay planes formed by the $\mu - \mu$ and $K - \pi$. Γ is the total decay width and Γ_T and Γ_L are the transversely and longitudinally polarized widths, respectively. These parameters can be expressed in terms of the decay amplitudes into particular final state helicities as:

$$\Gamma_T = |H_{+1}|^2 + |H_{-1}|^2, \qquad (C.2)$$

$$\Gamma_0 = |H_0|^2, \qquad (C.3)$$

$$\Gamma = \Gamma_T + \Gamma_L. \qquad (C.4)$$

The amplitudes are complex quantities. Interference of the different amplitudes gives rise to the remaining terms in equation C.1, where the parameters are defined as:

$$\alpha_1 = \frac{Re(H_{+1}H_0^* + (H_{-1}H_0^*)}{|H_{+1}|^2 + |H_{-1}|^2 + |H_0|^2}, \qquad (C.5)$$

$$\alpha_2 = \frac{Re(H_{+1}H_{-1}^*)}{|H_{+1}|^2 + |H_{-1}|^2 + |H_0|^2}, \qquad (C.6)$$

$$\beta_1 = \frac{Im(H_{+1}H_0^* + (H_{-1}H_0^*)}{|H_{+1}|^2 + |H_{-1}|^2 + |H_0|^2}, \qquad (C.7)$$

$$\beta_2 = \frac{Im(H_{+1}H_{-1}^*)}{|H_{+1}|^2 + |H_{-1}|^2 + |H_0|^2}. \qquad (C.8)$$

The Helicity amplitudes are in turn related to the calculated Lorentz invariant amplitudes [60]:

$$H_\lambda = \epsilon_{1\mu}^*(\lambda)\epsilon_{2\nu}^*(\lambda)(ag^{\mu\nu} + \frac{b}{m_1 m_2}p^\mu p^\nu + \frac{ic}{m_1 m_2}\epsilon^{\mu\nu\alpha\beta}p_{1\alpha}p_{1\beta}) \qquad (C.9)$$

The quantities $a, b,$ and c represent the s, d and p wave contributions to the decay.

The geometric acceptance in Chapter 4.2 was based on no net polarization ($\Gamma_T = 2\Gamma_L$). To estimate the variation in the acceptance due to polarized J/ψ and K^{0*} mesons, a Monte Carlo was used to simulate the kinematics of all the particles in the decay chain. The following cuts were placed on the events:

- b P_T above 11.5 GeV/c,

- rapidity of the b less than 1,

- P_T of both muons above 2 GeV/c,

- P_T of the Kaon above 1 GeV/c,

- P_T of the π above 500 MeV/c,

- rapidity of both muons less than 0.65.

The number of events passing these requirements for different values of the parameters in Equation C.1 was compared with the number passing in the unpolarized case. Figure C.1 shows the relative change in acceptance as a function of the fraction of transverse polarization for the predicted values of α_1 and α_2 from Reference [60]. Based on this study, a systematic uncertainty of $^{+0.00}_{-0.20}\%$ was estimated. The estimate included variation of the parameters α_1, α_2, and Γ_T/Γ.
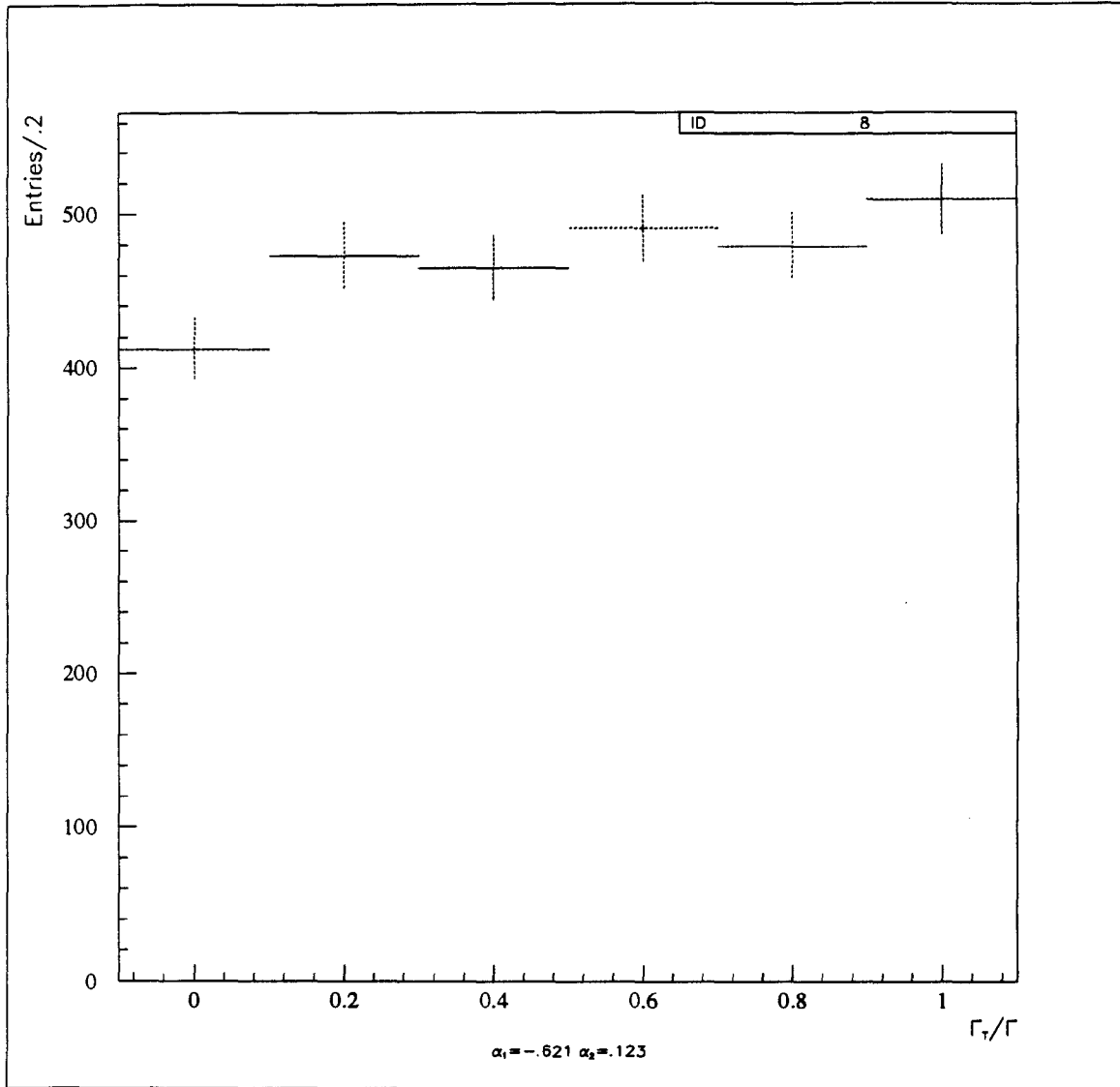
Figure C.1: Relative geometric acceptance for different polarization of K^{0*} and J/ψ mesons in B^0 decays. The plot shown here was generated with $\alpha_1 = -0.621$ and $\alpha_2 = 0.123$.

Bibliography

[1] S. Weinberg, Phys. Rev. Lett **19**,1264 (1967) A. Salam, *Elementary Particle Theory:Relativistic Groups and Analyticity*(8th Nobel Symposium) 1968, p. 367

[2] A sampler of texts which review the Standard Model includes: C. Quigg, *Gauge Theories of the Strong, Weak, and Electromagnetic Interactions*, Benjamin, 1983; F. Halzen and A. Martin, *Quarks and Leptons*, Wiley & Sons, (1984) ; Aitcheson and Hey, *Gauge Theories in Particle Physics*, 1989, Adam Hilger, Bristol and Philadelphia

[3] H. Goldstein, *Classical Mechanics*, pp 151-152, Addison-Wesley, Reading, MA (1980)

[4] G. Arnison, *et. al.*, Phys. Lett. **B122**,103 (1983), Phys. Lett. **B126**,398 (1983)

[5] N. Cabibbo, Phys. Rev. Lett.**10**,531 (1963); M. Kobayashi and T. Maskawa, Prog. Theor. Phys. **49**, 652 (1973)

[6] Phys. Rev. D **45** No.11,III65-66 (1992)

[7] Phys. Rev. D **45** No.11 III65 (1992)

[8] In addition to the references listed in [2], the following are particularly useful for understanding QCD and the Parton Model: *Quantum Chromodynamics: Theory*

and Experiment, Proceedings of the Third Lake Louise Winter Institute, World Scientific (1988); *Quantum Flavordynamics, Quantum Chromodynamics, and Unified Theories*, Plenum Press; R.D. Field, *Applications of Perturbative QCD*, Addison Wesley (1989)

[9] C.Quigg, *Gauge Theories of the Strong, Weak, and Electromagnetic Interactions*, Benjamin, 1983

[10] J. Siegrist *et. al.* Phys. Rev. **D26**,969 (1982)

[11] G. Hanson,*et. al.* Phys. Rev. Lett. 35,1609 (1975)

[12] R. Brandelik, *et. al.* Phys. Lett. 86B 243(1979); Barber *et. al.* Phys. Rev. Lett. 43,830 (1979)

[13] G. t'Hooft, Nucl. Phys. **B33**,177 (1971);**B35**, 167 (1971)

[14] R.P. Feynman, *Photon-Hadron Interactions* 1972 Benjamin, Reading, MA

[15] J.D. Bjorken, Phys. Rev. **163**,1767 (1967)

[16] J.T. Friedman and H.W. Kendall, Ann. Rev. Nucl. Science, **22**, 203 (1972)

[17] E. Eichten, C. Quigg, I. Hinchliffe, and K.D. Lane, Rev. Mod. Phys. 56 (1984) 579, Rev. Mod. Phys 58 (1985) 1065

[18] D.W. Duke and J.F. Owens, Phys. Rev. D30 (1984) 49

[19] M. Diemoz, F. Ferroni, E. Longo, and G. Martinelli , Z.Phys. C39 (1988) 21

[20] J.G. Morfin and W.K. Tung, Z.Phys. C52 (1991) 13

[21] M.Gluck, J.F. Owens and E. Reya, Phys. Rev. **D17** (1978) 2324

[22] B. Combridge, Nucl. Phys. **151** (1979) 429

[23] A. Kernan and G. VanD'alen, Phys. Rep. 106, 298 (1984); M. Aguilar-Benitez *et. al.*, Phys. Lett. **B161**, 400 (1985); M.E. Duffy *et. al.*, Phys. Rev. Lett. 55, 1816 (1985)

[24] P. Nason, S. Dawson, and R.K. Ellis, Nucl. Phys. **B288** (1988)

[25] P. Nason, S. Dawson, and R.K. Ellis, *et. al.* Nucl. Phys. **B327** (1989) 49

[26] E.M. Levin, *et. al.*, Sov. J. Nucl. Phys. 54, 867-871 (1991)

[27] Preprint FNAL-Conf-89/168-T

[28] E.L. Berger, J.C. Collins, and D.E. Soper Phys. Rev. **D35** 7 (1987) 2272

[29] Berger and Meng, *Heavy Quark Cross Sections at Hadron Collider Energies* ANL-HEP-PR-92-11 January,1992

[30] P.N. Harriman, A.D Martin, W.J. Stirling, and R.G. Roberts, Phys. Lett. **B243**,421 (1990)

[31] P.N. Harriman, *et. al.*, to be published in Phys. Rev. D

[32] F. Abe, *et. al.*Phys. Rev. Lett. 68,3403-3407 (1992); F. Ukegawa, *Bottom Quark Production in 1.8-TeV Proton-Antiproton Collisions*, Ph.D. Thesis, University of Tsukuba (1991)

[33] C. Albajar *et. al.*, Phys. Lett **B256**, 121 (1991)

[34] D. DeCamp, *et. al.*, Physics Letters **B236**, 511 (1990)

[35] R.K. Ellis, Phys. Lett. **B259** 492-496 (1991)

[36] K. Symon *Mechanics pp* 144-147, Addison-Wesley (1971); R. Fernow *Introduction to Experimental Particle Physics pp* 234-236, Cambridge University Press (1986)

[37] F. Bedeschi *et. al.* Nucl. Meth. A238, 50-74 (1988)

[38] F. Abe *et. al.* Phys. Rev. D44, 30 (1991)

[39] M. Bozzo *et. al.* Nucl. Phys. **B308**, 724 (1988)

[40] CDF note 1642; F. Abe *et. al.*, to be published in Phys. Rev. Lett.

[41] R. Hughes *Reconstruction of B Meson Decays and Measurement of the B Quark and B Meson Production Cross Sections at the Fermilab Tevatron Collider* (Ph. D. Thesis, University of Pennsylvania) (1992)

[42] C. Peterson, et. al., Phys. Rev. D27,105 (1983)

[43] R.D Field, R.P. Feynman, Nuclear Physics **B136** ,1 (1978)

[44] D. Bortoletto, *et. al.*, Phys. Rev. D37,1719 (1988)

[45] Particle Data Group,Phys. Rev. D45, Part 2 (1992)

[46] *ibid.*

[47] M. Danilov, *International Symposium on Lepton and Photon Interactions at High Energies*, Geneva, 1991

[48] H.A. Bethe, Phy. Reports 89, 1256 (1953); W.T. Scott, Rev. Mod. Phys. 35, 231 (1963)

[49] M. Spahn, Private Communication

[50] C. Boswell, Private Communication; to be published in Phys. Rev. Lett.

[51] Particle Data Group,Phys. Rev. D45, Part 2 (1992)

[52] Particle Data Group,Phys. Rev. D45, Part 2 (1992)

[53] Particle Data Group,Phys. Rev. D45, Part 2 (1992)

[54] A.G. Frodesen, O. Skjeggestad, and H. Tøfte, *Probability and Statistics in Particle Physics*,1979, Columbia University Press, NY

[55] E. Berger and R. Meng, ANL-HEP-PR-92-32

[56] R.S. Fletcher, F. Halzen, R.W. Robinett, Phys. Lett. **B225**, 176 (1989); H. Zi-aeepour, Ph. D. thesis, Orsay (1988)

[57] Particle Data Group, Phys. Rev. D45, Part 2 (1992)

[58] G. Kramer, W.F. Palmer, Phys. Lett. **B279** 181-188 (1992)

[59] J. Richman, *A Study of the Iota in Radiative JPsi Decays* (Ph. D. Thesis, California Institute of Technology) (1985)

[60] M. Bauer, B. Stech, M. Wirbel, Z. Phys. C34 (1987) 103; M. Bauer, B. Stech, M. Wirbel, Z. Phys. C29 (1985) 637

Vita

The author was born at Torrejon A.F.B, outside of Madrid, Spain to Steve and Maria Vejcik on February 27, 1963. He attended public schools in Alabama, Texas, and Virginia before entering George Mason University in Fairfax, Virginia where he received the Batchelor of Science degree in May, 1986. In September, 1986, he began graduate study at The Johns Hopkins University in Baltimore, Maryland and received the Master of Arts degree in May, 1988. He began research in experimental High Energy Physics during the Summer of 1987 on the Mark II experiment at the Stanford Linear Accelerator Collider. In March, 1989 he began research on the CDF collaboration at Fermilab in Batavia, Illinois which culminated in a doctoral thesis, *A Measurement of the b quark and Neutral B meson Cross Sections at Center of Mass Energy of 1.8 TeV.*